Formation Processes of Clathrate Hydrates of Carbon Dioxide and Methane

Thesis by

Veronica R. Blackwell

In Partial Fulfillment of the Requirements

for the Degree of

Doctor of Philosophy

California Institute of Technology

Pasadena, California

1998

(submitted June 5, 1998)

Acknowledgements

I thank my advisors, Dr. J. J. Morgan and Dr. W. J. North for their wisdom, guidance, support, and most of all, encouragement.

I gratefully acknowledge the assistance of Russ, Rodney, John, Rich, Rick and Hai, as well as everyone else, who came through for me in my many apparatus breakdown emergencies.

I thank Fran, Carmen and Linda for all their help, smiling faces and funny stories.

I also thank my family and friends, especially Mikey, for their encouragement and happy times, without which I never would have finished.

And of course, I thank the Electric Power Research Institute for partial funding of this project.

Abstract

This thesis explores the formation kinetics and mechanisms of clathrate hydrates of carbon dioxide and methane, focusing on the nucleation and early growth of hydrates. Homogenous and heterogeneous systems were studied. The catalysis of hydrate nucleation was accomplished by the addition of certain particles to the hydrate forming solution. Copper (II) oxide, calcium carbonate and some α and γ aluminum oxide particles were found to be effective nucleators while α-iron oxide, magnesium hydroxide, silica and some other α and γ aluminum oxide particles were found ineffective. The induction period for hydrate formation was reduced by as much as 85% with copper oxide particles. The important requisites of a nucleation catalyst included a satisfactory match between the crystal structure faces of ice and catalyst particle. The nature of the surface hydroxyl groups on the particle was also important. Particles nucleated hydrate by encouraging hydrogen bonding between the surface hydroxyl groups on the particles and water molecules near the surface, forming a layer of structured water. These structures then built up into clathrate cages when stabilized by guest molecules. Methane hydrate only formed at the interface between gas and water, because only there were there enough methane molecules to stabilize the structures. Carbon dioxide hydrate formed in the bulk solution because the higher solubility of carbon dioxide in water ensures enough carbon dioxide molecules to stabilize cages and allow them to grow into full hydrate structures.

Table of Contents

List of Figures

List of Tables

Chapter 1 Introduction

1.1 Introduction

This thesis explores the formation kinetics and mechanisms of clathrate hydrates of carbon dioxide and methane. The work focuses on the nucleation and early growth of hydrates.

Carbon dioxide hydrates are central to any proposed plan of sequestering carbon dioxide in the deep oceans to minimize global warming and are, therefore, the primary focus of this thesis. An improved understanding of the formation of carbon dioxide hydrate is essential to evaluate the efficiency and impact of any sequestering program. Methane hydrates are interesting for their energy potential, their ability to block natural gas pipelines and their involvement in global warming.

1.2 Motivation

1.2.1 Oceanic Sequestering of Carbon Dioxide

Sequestering anthropogenically produced carbon dioxide in the deep oceans was first proposed twenty years ago as a possible means of mitigating global warming. Marchetti originally proposed injecting carbon dioxide off the Strait of Gibraltar where sinking thermohaline currents would carry the carbon dioxide down to the depths of the ocean, there to be dispersed for thousands of years [1].

The ocean is an ideal storage repository because of its large uptake capacity for carbon dioxide. Carbon dioxide dissolves in the oceans to form carbonic acid that dissociates to form bicarbonate and carbonate ions. The oceans buffer carbon dioxide by reaction with carbonate ions to form more bicarbonate ions and by the dissolution of carbonate sediments. Rough estimates of carbon dioxide storage can be simply calculated by estimating the quantity of carbonate ion and available calcium carbonate sediments in the ocean, 12×10^{16} and 40×10^{16} moles respectively. Assuming these amounts to be completely available for reaction yields storage potentials of 1440 and

4800 gigatonnes carbon, respectively [2, 3]. This acid neutralizing capacity enables the oceans to absorb large quantities of carbon dioxide without large pH variations.

Although global emissions of fossil fuel fired power stations are approximately 5.3 gigatonnes of carbon dioxide per year [4], only about 50% of these emissions are treatable because of the small size and remote location of many plants, reducing the global controllable carbon dioxide emissions to 2.7 Gton CO_2/yr or 0.73 Gton C/yr. At this rate, the storage capacity of the ocean would not be depleted for thousands of years. Total global carbon emissions are about 5.5 Gton C/yr [5] so that only about 15% of the worldwide anthropogenic carbon emissions could be practically disposed of in the oceans by direct disposal, given the existing patterns of energy usage.

The oceans and atmosphere equilibrate with respect to carbon dioxide, though on a timescale of thousands of years because of the slow mixing between surface and deep waters. The final atmospheric carbon dioxide concentration is therefore independent of whether the carbon dioxide is released directly to the atmosphere or first discharged to the deep oceans. The advantage of directly disposing carbon dioxide into the deep oceans is reducing the peak atmospheric concentrations expected to occur over the next few centuries [6]. The transient carbon dioxide peak may be reduced by as much as 50%, depending on the fraction of produced carbon dioxide disposed of and the location and depth of disposal [2, 7, 8, 9]. Ocean carbon cycle and vertical diffusion models show that optimum disposal depth is at least 1000 meters [3, 10]. Disposing of, respectively, 0, 25, 50 and 75% of the projected global carbon dioxide production of 3800 Gton C between the years 2000 and 2200 at a depth of 3600 meters could reduce the atmospheric carbon dioxide increase from about 1150 ppm to 800 ppm, 475 ppm and 200 ppm. Again, only about 15% of the global carbon dioxide production under present conditions, could, at most, be realistically disposed of, resulting in a decrease of projected peak of approximately 13% [3]. The dissolution of calcium carbonate sediments could increase storage effectiveness over the long term [2, 3, 7, 11].

Direct disposal of carbon dioxide in the oceans involves capturing and separating carbon dioxide from power plant flue gases, transporting the carbon dioxide by pipeline to the coast and then down to the deep oceans. Disposal methods differ in cost, detrimental effect on marine life and efficiency of sequestering carbon dioxide.

The most frequently discussed disposal method is the condensing, pumping and injection of liquid carbon dioxide from a pipeline extending down from a stationary platform or a moving ship [6, 12, 13]. The pipe outlet would be designed with a multi-port diffuser to spread the discharge. Liquid carbon dioxide is denser than ambient seawater at depths greater than 3000 m (Figure 1.1) resulting in a negatively buoyant plume of carbon dioxide droplets that would dissolve in the seawater, increasing the density of the surrounding solution of seawater and carbon dioxide. This heavier water would sink, carrying the carbon dioxide farther away from the surface waters and increasing the effectiveness of sequestration. Disposal of liquid carbon dioxide at depths less than 3000 m but greater than 500 m, the shallowest depth at which carbon dioxide is liquid, would be possible but carbon dioxide droplets would rise as they dissolved, bringing carbon dioxide closer to surface waters and thereby not storing it as effectively.

Shallow release of gaseous carbon dioxide bubbles is also possible at depths less than 500 meters [6, 12, 14]. The bubbles, less dense than ambient seawater, would rise, entraining seawater. The carbon dioxide enriched seawater would cease to rise as it is denser than the surrounding seawater. Shallow injection, though not as effective for long-term sequestering of carbon dioxide, would be less expensive, as the injection pipeline could be shorter.

Another option is dissolving compressed carbon dioxide gas in seawater to produce a liquid stream with density greater than seawater and then injecting this solution at depths greater than 500 meters [4, 12, 13, 14]. The denser solution of carbon dioxide and water would sink while entraining more seawater, thereby dispersing carbon dioxide.

Carbon dioxide could also be dropped into the ocean in solid block form [12, 15]. The carbon dioxide in the outer layer would dissolve as it sinks, dispersing the carbon

dioxide over a long vertical column and reducing impacts on oceanic marine life [16]. If the block was large enough, the carbon dioxide would travel all the way to the ocean floor for maximum sequestration [12, 15] but possibly higher detriment to benthic life.

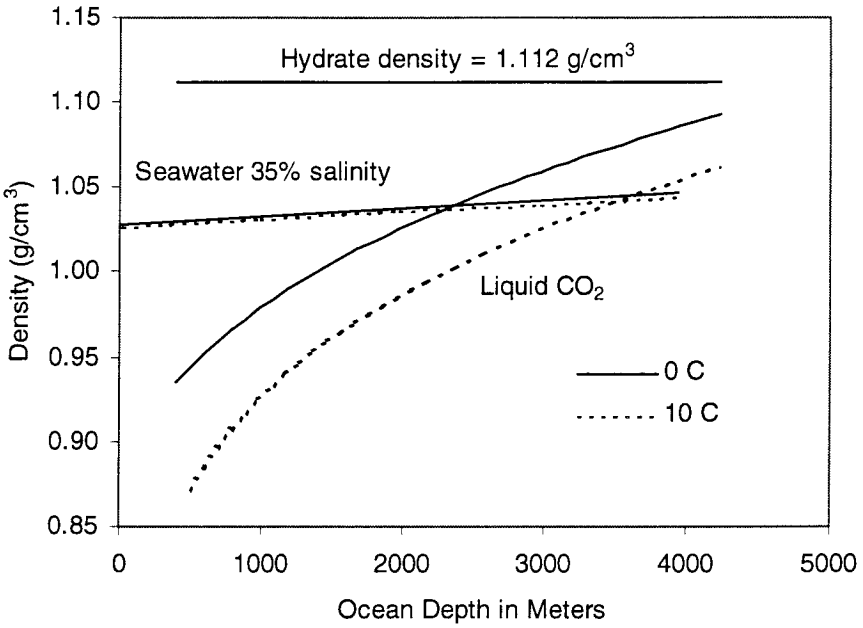

Figure 1.1: Densities of liquid carbon dioxide, seawater and carbon dioxide hydrate. Plotted from liquid carbon dioxide data of [17], seawater data from [18] and using density calculation of Chen [19].

1.2.2 The Role of Carbon Dioxide Hydrates

At the temperatures and pressures of the ocean at depths greater than 500 meters, carbon dioxide and water combine to form a solid, carbon dioxide hydrate (Figure 1.2). Carbon dioxide hydrate forms naturally in the ocean on CO_2 rich fluid venting from the sea floor at 1335 to 1550 meters depth in the mid-Okinawa Trough, Japan [20].

Perhaps the least expensive disposal method of carbon dioxide entails creating solid carbon dioxide hydrates from seawater in a plant at the ocean surface or shore, then injecting a slurry of hydrate and seawater to depth in the ocean [21]. The density of hydrate is approximately 1.112 g/cm^3 [19] and that of seawater about 1.03 g/cm^3, causing the carbon dioxide slurry to sink after injection, avoiding the high cost of compressing

liquid carbon dioxide to achieve the same density difference. The carbon dioxide hydrate would only serve for transportation and not as permanent disposal form. Carbon dioxide hydrate decomposes in water that is undersaturated with carbon dioxide [22, 23, 24, 25, 26, 27], such as ambient seawater, and therefore carbon dioxide hydrate will decompose after injection, either as it settles or after it reaches the seafloor. This point is often misunderstood, with some earlier disposal plans focussing on permanently storing carbon dioxide as blocks of hydrate on the seafloor [28]. Injecting carbon dioxide hydrate slurries at 700 meters depth and discharging in a downward direction should allow complete sequestering of the carbon dioxide for many centuries [21].

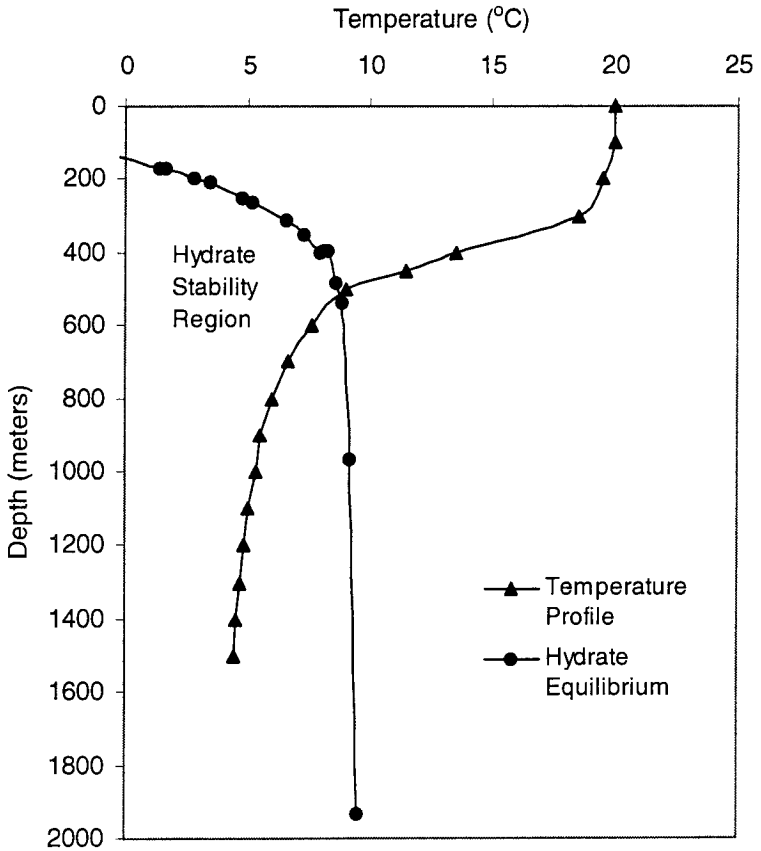

Figure 1.2: Typical temperature profile of the ocean at temperate latitudes superimposed on the carbon dioxide hydrate phase diagram, showing hydrate stability at ocean depths greater than 500 meters. Plotted from temperature profile data of Broecker and Peng [29] and seawater hydrate phase equilibrium data of [30, 31, 32].

Hydrates are also important in any disposal scheme as they can easily form at any interfaces between carbon dioxide and water. At ocean depths greater than 500 meters, hydrate will readily form where water is supersaturated with carbon dioxide such as the surface of discharged carbon dioxide droplets or bubbles. Hydrate coatings will affect density and thus buoyancy and travel direction of droplets or bubbles, and ultimately sequestering efficiency.

The quantity and rate of hydrate formation and decomposition, as well as factors, such as impurities, that affect these parameters must be well understood before assessing the effectiveness of disposal methods.

1.3 Background

1.3.1 Clathrate Hydrates of Carbon Dioxide and Methane

Clathrates are a type of inclusion compound in which one molecular species, the host, physically encages another, the guest. When the host species is water, the compound is referred to as a clathrate hydrate, or more commonly, simply hydrate. Carbon dioxide clathrate hydrate is composed of water as the host, encapsulating carbon dioxide as the guest.

Structure

Clathrate hydrates are solid, crystalline compounds. The hydrate crystal lattice structure consists of water molecules that are linked together through hydrogen bonding to form cages, or cavities. Each cage can hold up to one guest molecule that is linked to the lattice by van der Waals forces. The several types of hydrate structures that exist are distinguished by the size and arrangement of their cages. The basic building block of the common hydrate structures is the pentagonal dodecahedron cage, a polyhedron with 12 pentagonal faces. Carbon dioxide and methane form structure I hydrate in which the pentagonal dodecahedral cavities build up into lattices by linking through their vertices.

The pentagonal dodecahedron cavity is approximately spherical with a radius of 3.91 Å in structure I hydrate. The imprecise packing of pentagonal dodecahedral cavities creates tetrakaidecahedral cavities with 12 pentagonal faces and 2 hexagonal faces. The tetrakaidecahedral cage has an oblate shape and a radius of 4.33 Å. The structure I unit cell consists of six large tetrakaidecahedral cages and two smaller pentagonal dodecahedral cages for a total of 46 water molecules arranged in eight cages (Figure 1.3).

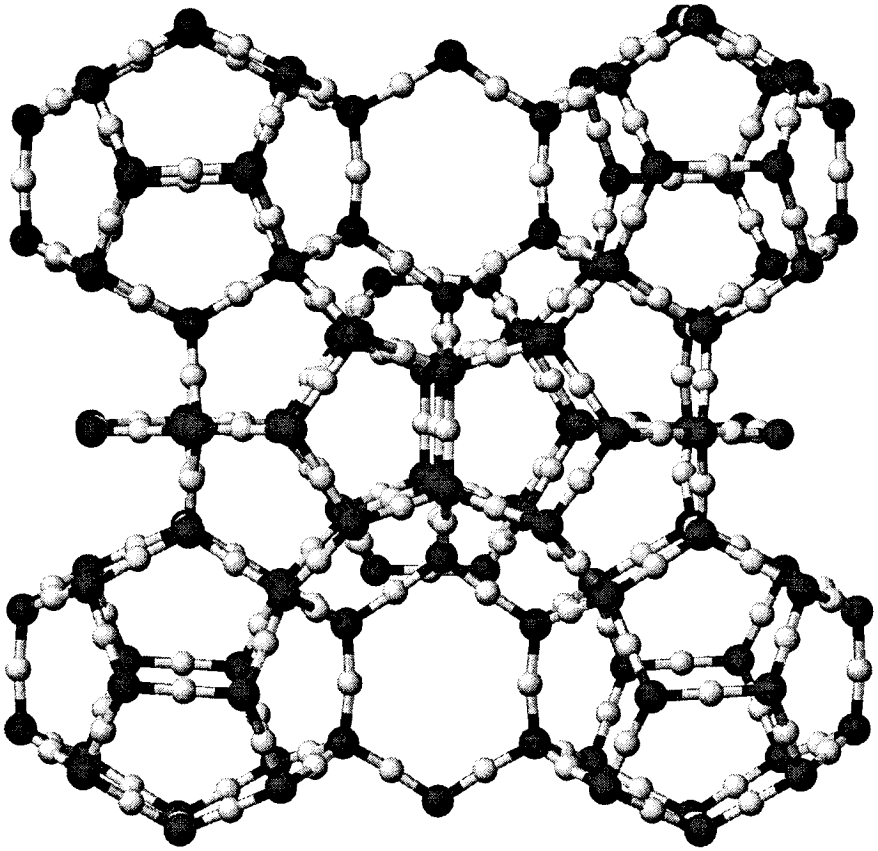

Figure 1.3: The crystal lattice structure for structure I carbon dioxide and methane hydrates, showing pentagonal dodecahedron and tetrakaidecahedral cavities.

Thermodynamics

Hydrates are only stable under conditions of high pressure and low temperature (Figures 1.4 to 1.7). The thermodynamic conditions of hydrate equilibrium have been well studied, both experimentally and theoretically. The system of water and hydrate former

consists of the following possible phases: liquid water, ice water, hydrate, hydrate forming gas and hydrate forming liquid.

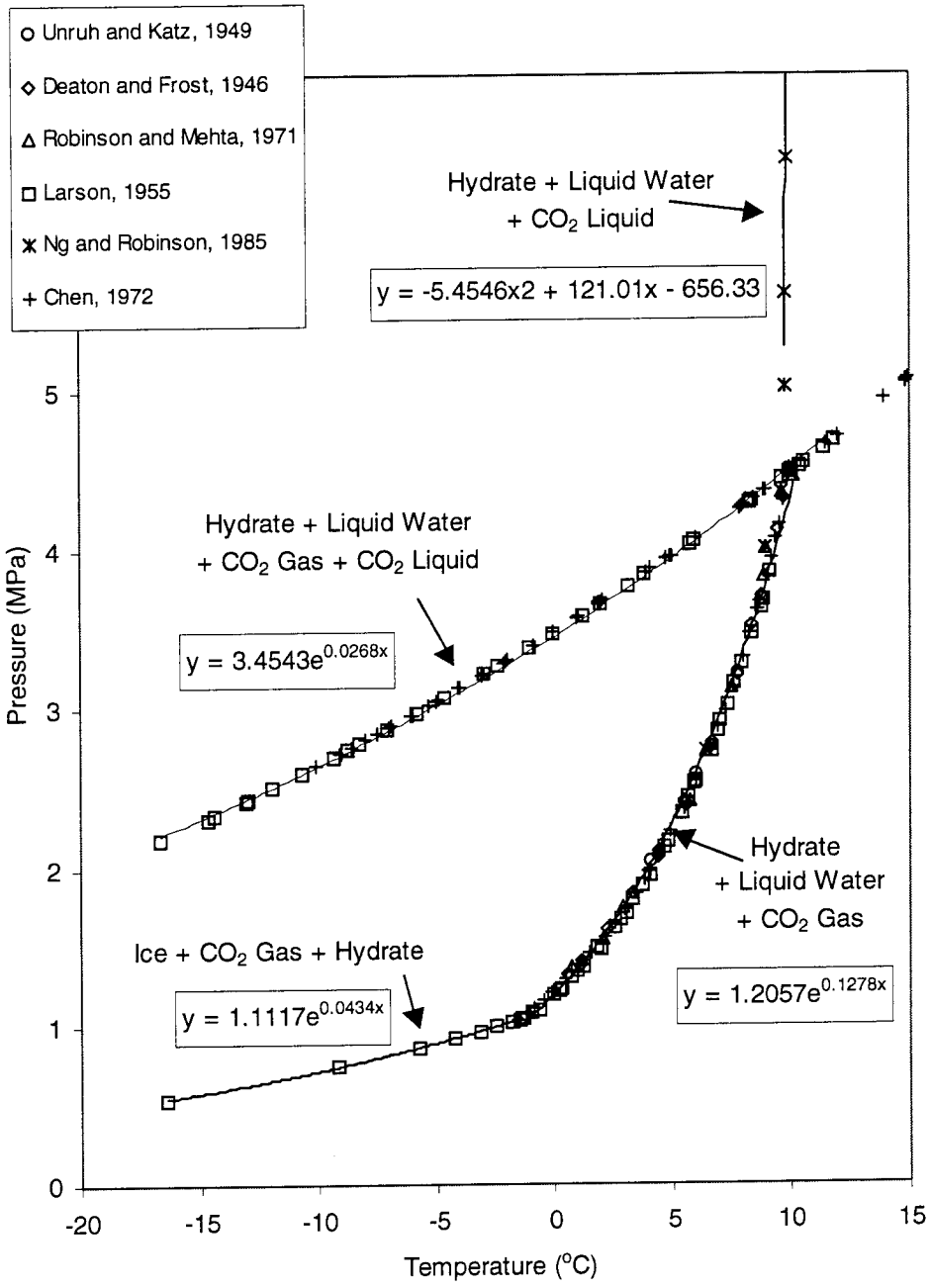

Figure 1.4: Phase diagram for carbon dioxide hydrate from pure water. Data from [33].

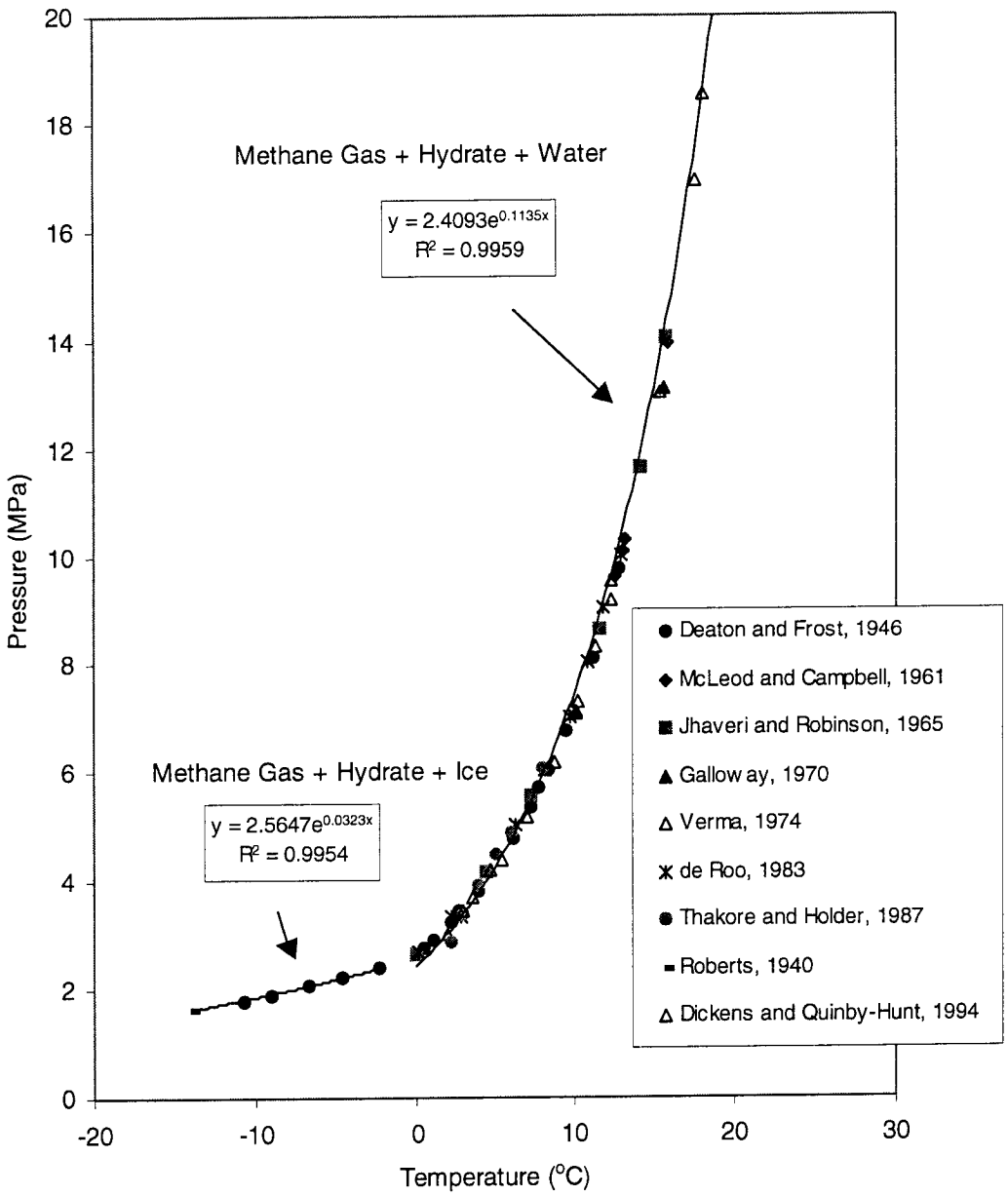

Figure 1.5: Phase diagram for methane hydrate from pure water. Data from [33].

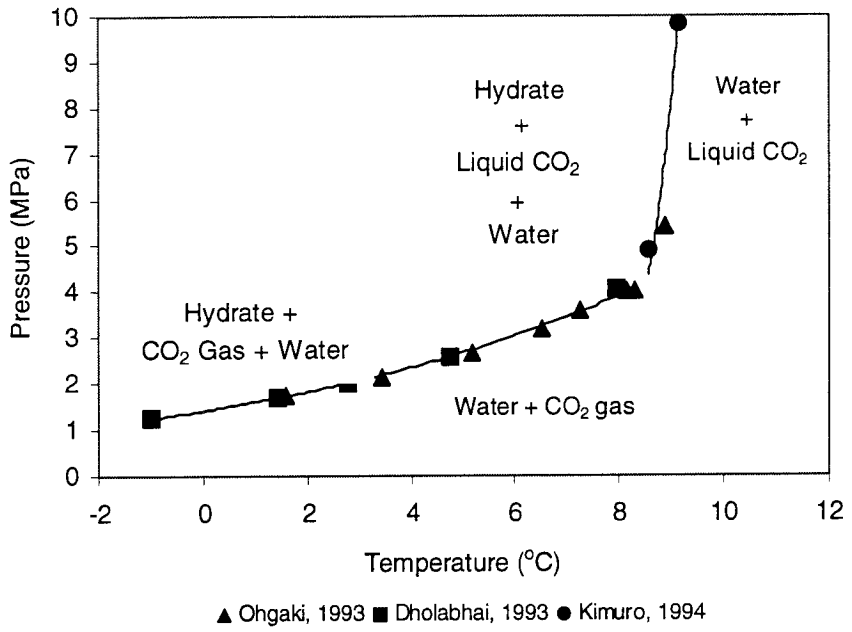

Figure 1.6: Phase diagram for carbon dioxide hydrate from sea water. Data from [30, 31, 34].

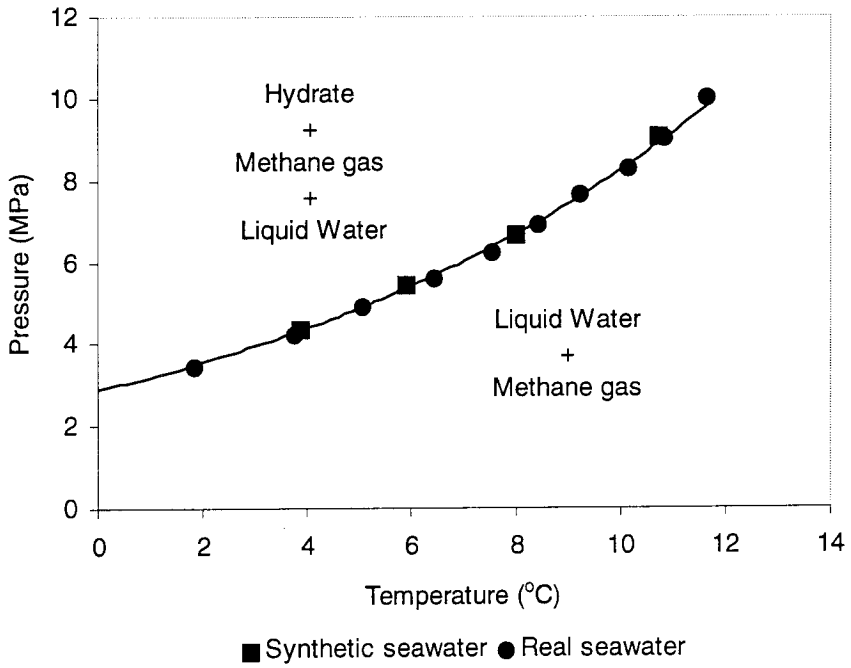

Figure 1.7: Phase diagram for methane hydrate from sea water. Real seawater data from [35] and synthetic seawater from [36].

The presence of electrolytes in the hydrate forming solution causes a shift in phase equilibrium towards higher formation pressures and lower formation temperatures, a shift to the left in Figure 1.8.

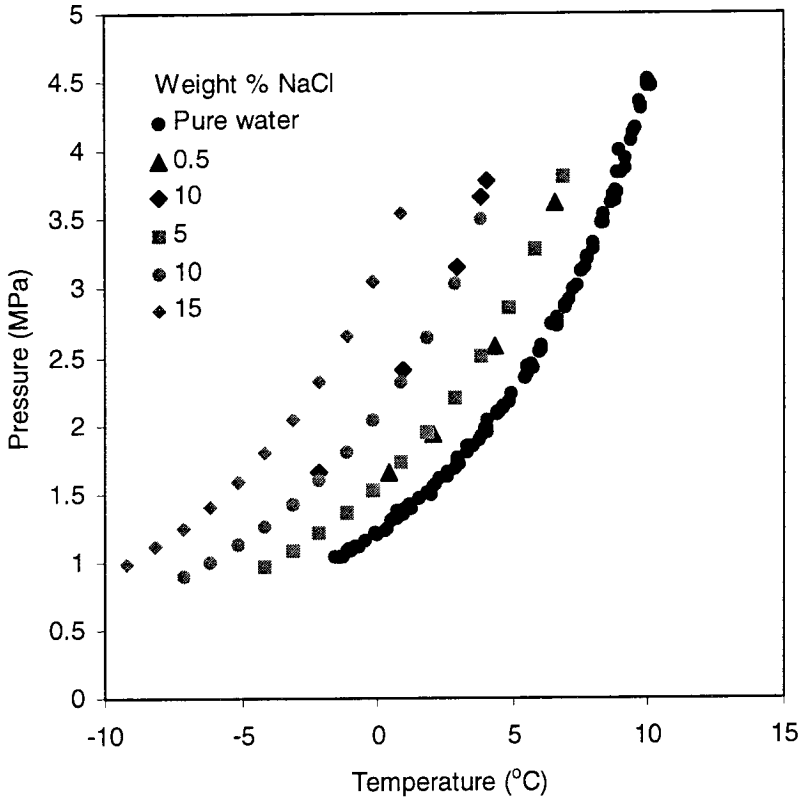

Figure 1.8: Phase diagram of carbon dioxide hydrate showing influence of electrolytes on hydrate equilibrium. Grey data points are calculated by Bakker et al. [37], black points are experimental data from Sloan [33] and Chen [19].

Composition

Each cage of the crystal lattice can hold up to one guest molecule that is linked to the water lattice by weak van der Waals forces. Hydrates are non-stoichiometric compounds with incompletely filled cavities. The ideal guest to water ratio for completely filled cavities is 1 : 5¾ for structure I hydrate. The hydrate number, defined as the number of water molecules per guest molecule, is then 5¾ for completely filled lattices of structure

I. Carbon dioxide and methane hydrates always have hydrate numbers greater than ideal (Figure 1.9).

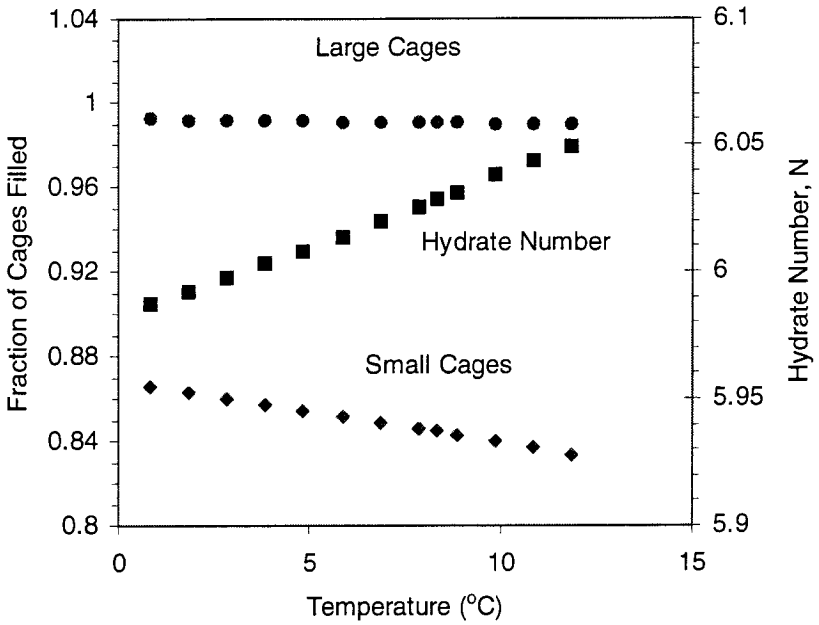

Figure 1.9: Hydrate number for carbon dioxide hydrate, calculated at a pressure of 5.5 MPa and varying temperature from 0 to 10 °C. Fraction of filled cages is also shown. Values calculated using the Colorado School of Mines, CSMHYD Hydrate Program, for estimating the equilibrium conditions of hydrate formation [33].

1.3.2 Chemistry of Carbon Dioxide in Water

Carbon dioxide is unique among hydrate formers because of its acid/base chemistry when dissolved in water. The dissolution of carbon dioxide in water produces the carbon species: dissolved unhydrated CO_2 or $CO_{2(aq)}$, hydrated CO_2 or carbonic acid, H_2CO_3, bicarbonate, HCO_3^-; and carbonate, CO_3^{2-}. These species form by the following reactions:

$$CO_{2\,(g)} \leftrightarrow CO_{2(aq)}$$

$$CO_{2(aq)} + H_2O \leftrightarrow H_2CO_3$$

$$H_2CO_3 \leftrightarrow HCO_3^- + H^+$$

$$HCO_3^- \leftrightarrow CO_3^{2-} + H^+$$

The predominance of one species over another is a function of pH. At neutral pH, HCO_3^- is most abundant. At low pH values, most of the carbon is in the form of $CO_{2(aq)}$, with some present as H_2CO_3. The equilibrium between CO_2 and H_2CO_3 lies far to the left such that less than 1% of the CO_2 is hydrated at atmospheric pressure and 25 °C [38].

The solubility of carbon dioxide in water increases with partial pressure of carbon dioxide (Figure 1.10). The increase in solubility leads to increased concentration of $CO_{2(aq)}$ and lower pH. pH decreases to about 3.2 to 3.3 when the partial pressure of carbon dioxide increases to about 0.5 MPa (Figure 1.11).

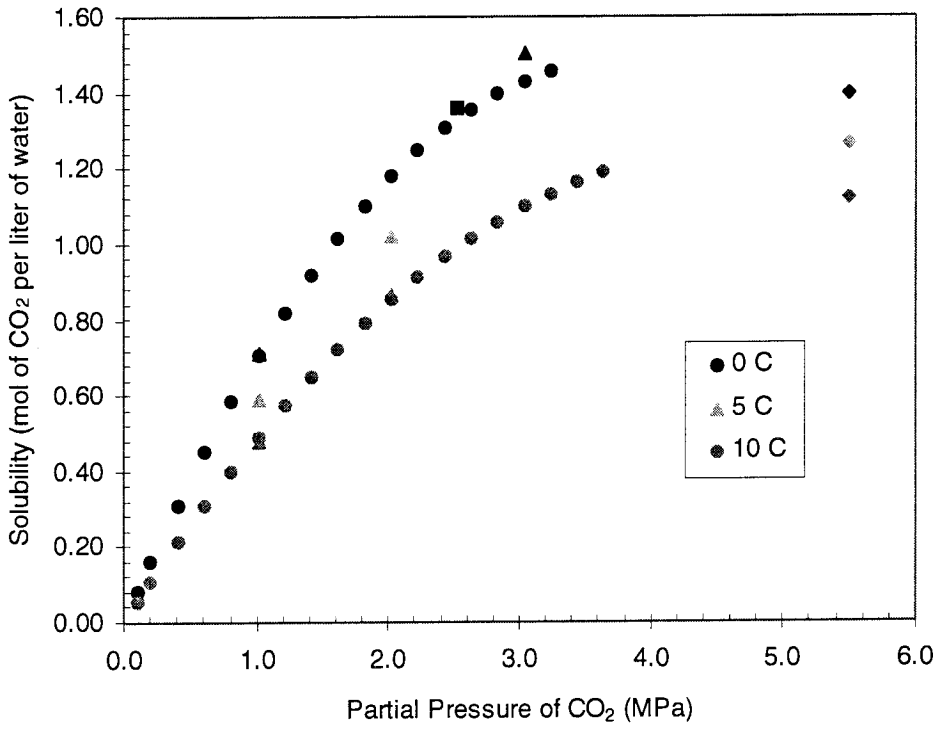

Figure 1.10: Solubility of CO_2 in water at high partial pressures of CO_2. Circles indicate data from [39], triangles from Stewart and Munjal [40]. Values at higher P_{CO2} have not been determined because of experimental difficulties with solid hydrate forming. Values at the experimental pressure of 5.5 MPa were calculated using pressure and temperature adjusted equilibrium constants.

Equilibrium constants for the high pressure and low temperature aqueous carbon dioxide system can be calculated from the work of Owen and Brinkley [41]. Speciation has been calculated for a pressure of 5.5 MPa, our experimental pressure, and assuming a pH of 3.2. The concentration of aqueous carbon dioxide is higher than the concentration of HCO_3^-, CO_3^{2-} and H_2CO_3 by several orders of magnitude.

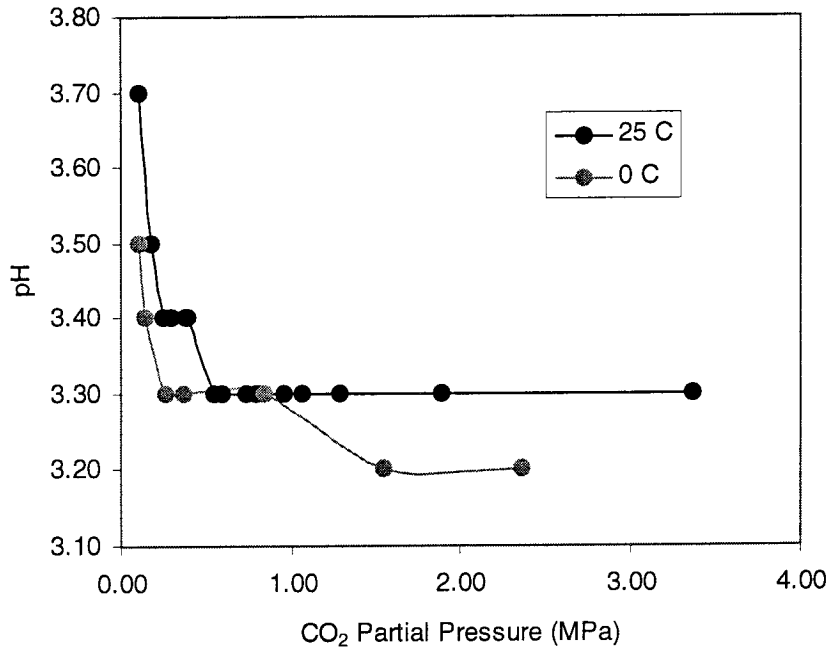

Figure 1.11: pH of solutions of water and carbon dioxide at high partial pressures of carbon dioxide. Plotted from data of [42].

1.3.3 Chemistry of Methane in Water

The solubility of methane is about one-tenth that of carbon dioxide (Figure 1.12). The critical temperature of methane is -82.1 °C; it is therefore a gas at all experimental conditions used in experiments described in this thesis.

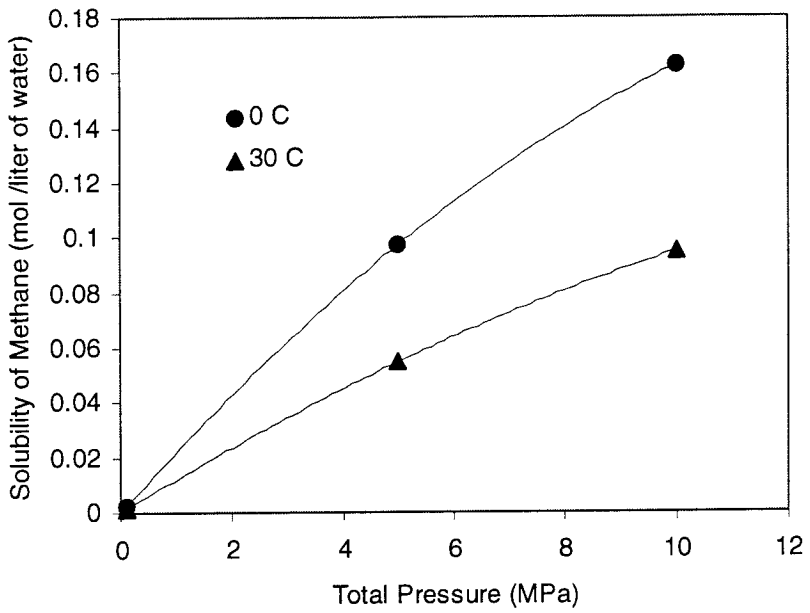

Figure 1.12: Solubility of methane in deionized water at 0 and 30 °C plotted versus total pressure [43]. Total pressure = partial pressure of CH_4 + partial pressure of H_20.

1.3.4 Clathrate Hydrate Formation

Hydrate formation consists of the two processes of nucleation and crystal growth. Nucleation involves the restructuring of guest and water molecules into critically-sized, stable nuclei, while crystal growth is the subsequent growth on these nuclei.

Little is known about the microscopic process of hydrate nucleation. The following discussion will begin with a description of the structure of liquid water and progress to both homogeneous and heterogeneous nucleation of crystals from aqueous solutions, including what is specifically known and hypothesized about hydrate nucleation.

Structure of Water

The emerging view of liquid water from molecular dynamics simulations is of a random, three-dimensional network of hydrogen bonded water molecules (Figure 1.13) [44, 45]. The network has a preference for tetrahedral geometry but contains many strained and broken bonds that continually rearrange, altering the network topology. The hydrogen

bonded network is, therefore, continually fluctuating and changing. Molecular simulations have found that polygons of hydrogen bonds are common, with the most frequently occurring being five and six member rings, with pentagons predominating (Figure 1.13). Pentagonal structures are the most stable at temperatures below 277 K [33]. The occurrence of these five and six member rings is important to note because the hydrate crystal structure itself is composed of five and six member rings of hydrogen bonded water molecules.

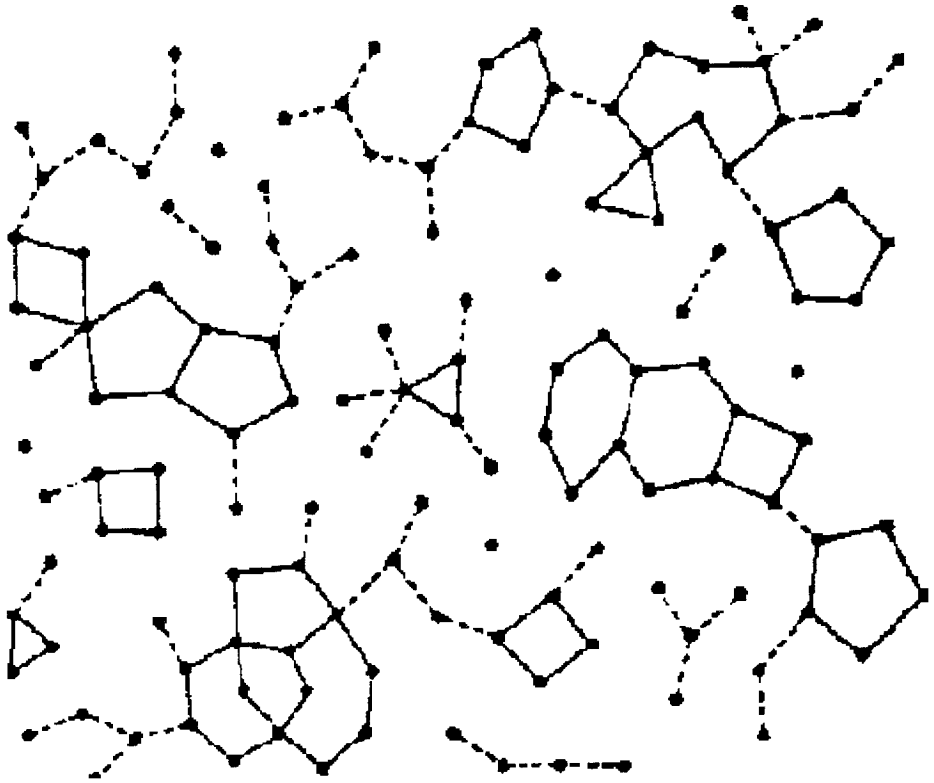

Figure 1.13: Molecular dynamics simulation of liquid water showing hydrogen-bonded networks of water molecules. Note the occurrence of five member rings. Reproduced from Rahman and Stillinger [44].

Stillinger [45] reports that the important issue in supercooled water is the concentration and spatial distribution of the relatively unstrained hydrogen bonded polyhedra embedded within and linked to the random network. The hydrogen bond angles in these polyhedra enable them to share faces and edges without the introduction

of strain, so they are able to link up with one another to form clusters. As water is supercooled, the hydrogen bonds become stronger and the polyhedra become more frequent, encouraging the formation of larger clusters [45].

The dissolution of apolar molecules in water is accompanied by a large negative entropy associated with the increased structuring of water molecules around the solute [33, 45]. The random hydrogen bonded network must reorganize around the dissolved molecule. Hydrate structures show that this rearrangement is possible and molecular simulations have shown that dissolution of dissolved molecules does create a clathrate-like, though imperfect, structure around the solute [45].

Homogeneous Hydrate Nucleation

Homogeneous nucleation is the formation of stable nuclei in a solution in which the remaining solution and the crystallized, solid phase are chemically identical [46]. Homogeneous crystal nucleation can only occur when the activation energy barrier to nucleation is overcome. For homogeneous nucleation, a certain critical supersaturation must be reached before stable nuclei can form. In the metastable zone between saturation and critical supersaturation, crystal nuclei grow and decompose randomly. The critical supersaturation can occur by exceeding phase equilibrium pressure or concentration or by operating at a temperature lower than the phase equilibrium temperature. The time in which a solution remains supersaturated before stable nuclei form is the induction period.

Homogeneous nucleation of hydrate crystals is hypothesized to occur when an apolar guest molecule dissolves in water and stabilizes the short-lived, hydrogen bonded water structures. The water molecule network grows and stabilizes around the dissolved guest molecules, forming metastable clusters of gas and water molecules, which have been termed hydrate precursors or intermediates. How these clusters grow microscopically to the critical nucleus size for further growth is still not well understood because little experimental data exist for this region. Theory is thus based on molecular dynamics simulations. Christiansen and Sloan [47] suggest that the labile clusters of

water molecules hydrogen-bonded around apolar molecules eventually attain the critical size needed for continued growth according to the local supersaturation fluctuations. Hydrate nucleation, therefore, is postulated as being a stochastic process, depending on these chance fluctuations.

The driving force behind nucleation, the supersaturation of the solution, is defined by the chemical potential difference between the experimental chemical potential of dissolved gas and the three-phase equilibrium chemical potential. The driving force can also be expressed in terms of fugacities, as the ratio between the experimental fugacity of dissolved gas and the fugacity at the three phase hydrate equilibrium pressure at the experimental temperature.

Heterogeneous Hydrate Nucleation

Most crystallization processes in natural waters and laboratory experiments start by heterogeneous nucleation on foreign solid substrates such as inorganic crystals, skeletal particles, clays, sands and biological surfaces in natural waters [48] and unknown impurities in laboratory waters. The scatter in data for hydrate nucleation induction times reported in the literature, as well as the near impossibility of ensuring completely pure, particle-free water for experiments, leads to the hypothesis that hydrate nucleation is invariably heterogeneous.

Foreign solids may catalyze nucleation processes by reducing the energy barrier for nucleation. If the surface of the solid substrate matches well with the crystal surface, the interfacial energy between crystal and solid would be smaller than between crystal and solution, promoting crystal nucleation at a lower supersaturation on the solid substrate than in the bulk solution [48]. For the interfacial energy between crystal and solid to be small, the two surfaces must match structurally, meaning that the crystal lattice parameters must be similar [46].

Heterogeneous nucleation of ice crystals on organic and inorganic solids has been reported. The most successful catalysts are stable and insoluble compounds whose

structures are similar to ice crystals such as PbI_2, AgI, CuO and Cu_2O (Table 1.1) [49]. For some of these catalysts, such as PbI_2 and AgI, the matching of crystal structures by lattice constants a, b and c is obvious, though for others a more detailed analysis is necessary (see [49]). Some organic molecules with good structural match also support nucleation [50].

Table 1.1: Crystal structure characteristics of ice and ice nucleating compounds [49].

Compound	Nucleating Temperature	Crystal System	Lattice Constant (Å)		
			a	b	c
Ice		Hexagonal	4.5135		7.3521
PbI_2	-1.3	Hexagonal	4.54		6.86
AgI	-2.6	Hexagonal	4.58		7.494
AgBr	-4.1	Cubic	5.768		
AgCl	-4.2	Cubic	5.547		
CuO	-4.3	Monoclinic	4.653	3.410	5.108
Cu_2O	-4.5	Cubic	4.252		

Because of the inability of some well-matched substrates to nucleate ice, lattice matching cannot be the only requirement for a good catalyst [51]. Particle surface charge has also been found to be important, with low surface charges being more favorable [51]. Other particle properties such as size, surface area and types of surface functional groups could also be important.

Naturally occurring oxides, like those of Al, Si and Fe(III), make up a large fraction of the solid phases in natural waters [48]. In the presence of water, the oxide surfaces are covered with surface hydroxyl groups, $\equiv SOH$. These hydroxyl groups exhibit amphoteric behavior:

$$\equiv SOH_2^+ \leftrightarrow \equiv SOH + H^+, \quad K_{a1}^s$$

$$\equiv SOH \leftrightarrow \equiv SO^- + H^+, \quad K_{a2}^s$$

The acid and base character of the surface groups is pH dependent. These surface hydroxyl groups may enhance (or interfere with) hydrogen bonding at the particle surface.

Vicinal water is defined as "interfacial water near a solid surface, the properties of which differ from the corresponding bulk properties due to structural differences induced by proximity to the surface" [52]. Water is thought to form a layered surface of essentially immobile water molecules around the particle which are in dynamic equilibrium with the surrounding bulk water. The water molecules structure in an orderly way on the surface due to enhanced hydrogen bonding between water molecules near the solid surface [52].

The hypothesized existence of increased hydrogen bonding in vicinal waters, the activity of oxide surface hydroxyl groups and the proven effectiveness of solid particles as ice nucleators led to the hypothesis that oxide surfaces may be good catalysts of hydrate nucleation.

Crystal Growth

The continued growth of hydrate nuclei once they reach critical size involves two steps. Dissolved gas diffuses from the bulk solution to the crystal-liquid interface. Then, an adsorption reaction occurs at the interface incorporating the gas molecule into the water cluster, stabilizing the cluster.

Experimentally, hydrate formation can be divided into three regions: gas dissolution, an induction period, and crystal growth. The nucleation process begins when the solution becomes saturated with gas and ends at the turbidity point, where hydrate particles become visible. The time period in which hydrate nucleation occurs, experimentally determined as the time elapsed from the beginning of supersaturation to the first appearance of hydrate, is the induction period. After the induction period, crystals are stable and grow according to known theory [46].

Hydrate Promoters and Inhibitors

Compounds that specifically affect either hydrate nucleation or growth are known as hydrate inhibitors or promoters (catalysts). Inhibitor compounds make hydrate formation more unfavorable, either by inhibiting nucleation, slowing hydrate growth, or changing

the equilibrium condition. Promoter compounds either promote nucleation or faster growth. Two kinds of hydrate inhibitors or promoters exist: thermodynamic and kinetic.

Thermodynamic inhibitors act to move the hydrate equilibrium phase boundary to a location less favorable to hydrate formation. Known thermodynamic inhibitors include methanol, ethanol, ethylene glycols and inorganic salts. They are needed in large concentrations (on the order of 20% of solution) and probably inhibit by hydrogen bonding with water [53].

Kinetic inhibitors reduce the rate of formation of hydrate. They operate either by delaying the formation of critical nuclei, or by slowing crystal growth, possibly by interfering with the preferred direction of crystal growth [54]. Kinetic inhibitors do not affect the equilibrium phase boundary as they function at very low concentrations, in the ppb range. Known kinetic inhibitors include surfactants, polymers and polymeric surfactants. Known specific inhibitors include Polyvinylpyrrolidone (PVP), Gaffix VC-713 (Vinylcaprolactum-PVP-Dimethylmminoethyllmethacrylate Copolymer) and PVCap Pol(N-Vinylca-prolactam) [55].

Only a small number of studies exist on the thermodynamic and kinetic promotion of hydrate formation. Ng and Robinson [56] have shown that at low concentrations, below about 10 mole % acetone water solutions, acetone can promote hydrate formation by shifting the thermodynamic phase equilibrium boundary as much as 8 °C. In kinetic inhibition supercooling experiments, Long [55] experimented with different materials for the mixing balls included in his reactors. Finding that stainless steel, brass, ceramic and glass balls produced shorter induction times than Teflon, nylon and wood mixing balls, he extended his studies to powdered stainless steel (316 and 140 mesh) to see if the metal surface may be providing nucleation sites for hydrate formation. Of the concentrations tested, ranging from 62.5 g/L to 462.5 g/L, only the highest concentration had a significant effect. However, the induction time was still about 75 minutes compared to a "ball stop time" (so much hydrate forms that the ball no longer moves when reactor is

rocked) of about ten minutes for the stainless steel ball. Long could not therefore infer a surface enhancement of hydrate nucleation.

Cha et al. [57] studied the effect of a bentonite clay surface on hydrate formation by measuring hydrate equilibrium temperatures and pressures. The solutions tested contained, in various combinations: water; bentonite, a swelling clay providing a large surface for strong ordered adsorption of water; chrome-lignosulfonate and NaOH, to seal and disperse the clay platelets, and PHPA, hydrolyzed polyacrylamide, to solvate the water. Solutions of bentonite and water; PHPA and water; and bentonite, thinner, caustic and water all showed thermodynamic enhancement of hydrate formation. By monitoring the pressure drop during hydrate formation, they were also able to conclude that hydrates form faster and more abundantly in solutions containing bentonite clay. The bentonite clay caused both thermodynamic promotion and kinetic enhancement of hydrate formation.

Bylov and Rasmussen [58] have reported effects of impurities on ethane induction times. By adding equal amounts of $CaCO_3$, $BaSO_4$, rust and asphaltenes to distilled water to make up a 1 g/L total impurity concentration, they were able to completely eliminate any induction times: hydrate formed immediately upon cooling and pressurizing to within hydrate stability limits. Using distilled water alone, induction times varied from 11 to 94 hours.

Chemical additives that decrease the activity of water by competing for available water molecules, primarily through hydrogen bonding, are thermodynamic inhibitors. Thermodynamic promoters are chemicals that set up water structures favorable to hydrate crystals, as in surface adsorption. Cha et al. [57] made an important distinction between kinetic and thermodynamic promoter mechanisms. Kinetic promotion requires only that a surface adsorb water molecules into random clusters that may eventually encourage formation of critical nuclei thereby causing faster crystal growth. Thermodynamic promotion, though, requires that the adsorbed water molecules are sorbed in an orderly, structured way, resembling a potential hydrate structure so that the reorganization of

water molecules into the hydrate cages is encouraged, causing the transition to occur at lower pressures and/or higher temperatures than indicated by the phase diagram.

1.4 Research Objectives

1.4.1 List of Objectives

The purpose of this research was to gain an improved understanding of the microscopic processes of hydrate formation and early growth, specifically, to understand the influence of surfaces on the kinetics and mechanisms of hydrate nucleation.

The objectives of this research are:

1. To determine whether hydrate nucleation could be catalyzed by the addition of several well-defined solid particles.
2. To determine which types and sizes of particles are most effective at catalyzing hydrate nucleation and the governing properties that make these the most effective catalysts.
3. To develop a mechanism for hydrate formation based on this knowledge.
4. To describe the location of hydrate nucleation by observing where hydrate first forms, in the bulk solution or on a surface or interface.
5. To study possible differences in formation between systems with an insoluble hydrate former, methane, and those with a more soluble hydrate former, carbon dioxide.
6. To determine reproducibility of hydrate nucleation times.
7. To determine whether particles naturally occurring in the ocean affect hydrate formation.
8. To determine whether particles are thermodynamic promoters of hydrate formation and/or kinetic promoters.

1.4.2 Research Needed Regarding Formation of Hydrates

The above issues should be addressed before carbon dioxide hydrates are ever used in a plan to sequester carbon dioxide in the ocean. Presently, hydrate formation is not well

understood and is highly variable. If carbon dioxide is to be transported to depth in hydrate form, a process for producing hydrates reproducibly and quickly is desirable for reducing production costs and increasing reliability of production.

1.5 Approach

A technique for comparing the kinetics of carbon dioxide hydrate formation in different aqueous solutions with different particulate additives was sought to determine whether the kinetics of hydrate formation could be significantly enhanced. Studies reported in the literature have shown that supercooling experiments are ideal indicators of hydrate kinetics.

1.5.1 Supercooling

A supercooling experiment consists of cooling the aqueous solution with hydrate former at a constant rate and measuring the temperature at which hydrate forms. Supercooling is defined as the difference between the experimental temperature of hydrate formation and the hydrate equilibrium temperature at the experimental pressure, as indicated by the phase diagram. In supercooling experiments with constant rate of cooling, the degree of supercooling is related to the time to hydrate formation, since higher degrees of supercooling are achieved by further cooling which takes a longer time. A large supercooling therefore indicates slow kinetics while a small supercooling would indicate fast kinetics (for the same cooling rate). The degree of supercooling can be transformed to a kinetic variable by dividing by the cooling rate, to obtain a time period, which is commonly called an induction period. Of all the possible techniques for measuring hydrate kinetics, such as measuring true nucleation induction times (measured at a constant temperature) or the amount of hydrate forming gas consumed in crystal growth, only supercooling at a constant rate is reproducible and independent of the apparatus size and arrangement [59].

Supercooling measurements are much more reproducible than the notoriously stochastic true induction time measurements. Reed et al. [53] used supercooling

experiments in a flow loop to test the effectiveness of kinetic inhibitors, chemicals that slow hydrate formation. For a given cooling rate and loop flow rate, the average difference between the highest and lowest supercooling was 0.68 °F, while the supercooling for inhibited and uninhibited systems differed by about 6 °F. Lederhos and Sloan [60] also studied kinetic inhibitors by supercooling and found a standard deviation of only 0.7 °C, with differences between inhibited and uninhibited systems of about 10 °C. They also showed consistency between bench scale and pilot scale flow loop results, showing that supercooling was independent of their experimental systems.

1.5.2 Experimental Approach

The supercooling method was used to study the effect of adding various types and sizes of particles to hydrate forming solutions to determine whether hydrate nucleation could be catalyzed by surfaces. The particles studied were chosen for their different chemical and physical surface properties. Silica particles were studied first because they are naturally present in ocean waters.

1.5.3 Development of Research

Studying the microscopic process of hydrate formation experimentally was difficult. Because of the stochastic nature of nucleation induction times, results were highly variable. Much experimentation involved defining and minimizing this variability.

Early work entailed developing a spectroscopic method to study the hydrate nucleation process. Nuclear magnetic resonance spectroscopy was used to detect hydrate precursors or intermediates just before hydrate formation. An NMR tube was designed for in-situ high pressure hydrate formation and real-time monitoring. Because of the need to use C^{13} labeled CO_2 to obtain a detectable signal, experiments were costly. The reaction could not be visually monitored once inside the NMR instrument. Consequently, variability in hydrate formation times rendered experimentation intractable. Because of the difficulty and cost, NMR experimentation was discontinued.

The hydrate forming solution in the NMR experiments was agitated by the bubbling action of the carbon dioxide. This bubbling action was inconsistent and presumably compounded variability in hydrate formation times. The reactor was redesigned with stirring bar and magnetic stirrer, producing reproducible mixing but variability remained high. Suspecting that this lingering irreproducibility was at least partly caused by heterogeneities in the hydrate forming solution, resulting in heterogeneous, and not homogeneous nucleation, improved reactor cleaning processes were adopted. When this failed to reduce the variability, the reactor was again modified to eliminate contact between solution and reactor wall, but this too failed to improve reproducibility.

Experiments reported in the literature with good reproducibility of induction times were performed with synthetic natural gas, 87.2% methane. [60]. Methane, being a gas at our experimental temperatures and pressures and not as easily absorbed by plastic components of apparatus proved easier in experimentation than the highly acidic, invasive, liquid carbon dioxide. A set of experiments was performed with methane gas, finally achieving acceptable reproducibility.

The possibility of purposefully inducing heterogeneous nucleation to further minimize variability in hydrate formation was next studied by adding various kinds of particles to the solutions. After completing methane experiments, experiments were repeated and extended with carbon dioxide.

The final carbon dioxide and methane supercooling experiments are reported in the main part of this thesis. NMR experiments are included in Appendix A.

1.6 References

1. C. Marchetti, *Climate Change* **1**, 59-68 (1977).
2. K. H. Cole, G. R. Stegen, D. Spencer, *Energy Conversion and Management* **34**, 991-998 (1993).
3. K. H. Cole, G. R. Stegen, G. L. Simmons, The ability of the oceans to absorb CO_2, The International Symposium on CO_2 Fixation and Efficient Utilization of Energy, Tokyo, Japan (RCCRU of Tokyo Institute of Technology, 1993).
4. C. F. Baes, S. E. Beall, D. W. Lee, G. Marland, in *Interactions on Energy and Climate* W. Bach, J. Pankrath, J. Williams, Eds. (D. Reidel Publishing Company, 1980) pp. 495-519.
5. J. T. Houghton, et al., Eds., *Climate change 1995. The science of Climate Change* (Cambridge University Press, Cambridge, 1996).
6. D. Golomb, *Energy Conversion and Management* **34**, 967-976 (1993).
7. T. R. S. Wilson, *Energy Conversion and Management* **33**, 627-633 (1992).
8. R. K. Dewey, G. R. Stegen, R. Bacastow, *Energy Conversion and Management* **38**, S349-S354 (1997).
9. H. J. W. De Barr, M. H. C. Stoll, in *Climate and Energy* P. A. Okken, R. J. Swart, S. Zwerver, Eds. (1989) pp. 143-177.
10. R. Bacastow, G. R. Stegen, Estimating the potential for CO_2 sequestration in the ocean using a carbon cycle model, Oceans (1991).
11. C. S. Wong, R. Matear, *Energy Conversion and Management* **34**, 873-880 (1993).
12. E. E. Adams, D. S. Golomb, H. J. Herzog, *Energy Conversion and Management* **36**, 447-452 (1995).
13. H. J. W. De Barr, *Energy Conversion and Management* **33**, 635-642 (1992).
14. H. Drange, P. M. Haugan, *Energy Conversion and Management* **33**, 697-704 (1992).
15. C. N. Murray, L. Visintini, G. Bidoglio, B. Henry, *Energy Conversion and Management* **37**, 1067-1072 (1996).
16. H. J. Herzog, E. E. Adams, D. Auerbach, J. Caulfield, *Energy Conversion and Management* **37**, 999-1005 (1996).
17. M. P. Vukalovich, V. V. Altunin, *Thermophysical properties of carbon dioxide* (Collet's Publishers Ltd., London, 1968).
18. R. A. Horne, *Marine Chemistry. The Structure of Water and the Chemistry of the Hydrosphere* (Wiley-Interscience, Toronto, 1969).

19. H. Chen, Master of Science, Syracuse University (1972).

20. H. Sakai, et al., *Science* **248**, 1093-1096 (1990).

21. D. F. Spencer, W. J. North, *Energy Conversion and Management* **38**, S265-S271 (1997).

22. H. Teng, C. M. Kinoshita, S. M. Masutani, *Chemical Engineering Science* **50**, 559-564 (1995).

23. W. J. North, V. R. Blackwell, J. J. Morgan, *Environmental Science and Technology* **32**, 676-681 (1998).

24. K. P. Loken, T. Austvik, *Energy Conversion and Management* **34**, 1081-1087 (1993).

25. P. C. Lund, Y. Shinda, Y. Fujioka, H. Komiyama, *International Journal of Chemical Kinetics* **26**, 289-297 (1994).

26. I. Aya, K. Yamane, H. Nariai, *Energy* **22**, 263-271 (1997).

27. I. Aya, K. Yamane, N. Yamada, Effect of CO_2 concentration in water on the dissolution rate of its clathrate, The International Symposium on CO_2 Fixation and Efficient Utilization of Energy, Tokyo, Japan (RCCU of Tokyo Institute of Technology, 1993).

28. H. Noda, et al., in *Carbon Dioxide Chemistry: Environmental Issues.* J. P. Pradier, C. M. Pradier, Eds. (The Royal Society of Chemistry, Stockholm, Sweden, 1994).

29. W. S. Broecker, T. H. Peng, *Tracers in the Sea* (Columbia University, Palisades, N.Y., 1982).

30. K. Ohgaki, Y. Makihara, K. Takano, *Journal of Chemical Engineering of Japan* **26**, 558-564 (1993).

31. P. D. Dholadhai, N. Kalogerakis, P. R. Bishnoi, *Journal of Chemical Engineering Data* **38**, 650-654 (1993).

32. H. Kimuro, T. Kusayanagi, *IEEE Transactions on Energy Conversion* **9**, 732-735 (1994).

33. E. D. J. Sloan, *Clathrate Hydrates of Natural Gases.* H. Heineman, Ed., Chemical Industries (Marcel Dekker, Inc., New York, 1990), vol. 39.

34. H. Kimuro, F. Yamaguchi, K. Ohtsubo, T. Kusayanagi, *Energy Conversion and Management* **34**, 1089-1094 (1993).

35. G. R. Dickens, M. S. Quinby-Hunt, *Geophysical Research Letters* **21**, 2115-2118 (1994).

36. T. Maekawa, S. Itoh, S. Sakata, I. Shun-Ichiro, I. Nboru, *Geochemical Journal* **29**, 325-329 (1995).

37. R. J. Bakker, J. Dubessy, M. Cathelineau, *Geochimica et Cosmochimica Acta.* **60**, 1657-1681 (1996).

38. R. Van Eldik, D. A. Palmer, *Journal of Solution Chemistry* **11**, 339-346 (1982).

39. G. Houghton, A. M. McLean, P. D. Ritchie, *Chemical Engineering Science* **6**, 182-187 (1957).

40. P. B. Stewart, P. Munjal, *Journal of Chemical and Engineering Data* **15**, 67-71 (1970).

41. B. B. Owen, S. R. Brinkley, *Chemical Revisions* **29**, 461-474 (1941).

42. E. L. Quinn, C. L. Jones, *Carbon Dioxide* (Reinhold Publishing Company, New York, 1936).

43. Z. Duan, N. Moller, J. Greenberg, J. H. Weare, *Geochimica et Cosmochimica* **56**, 1451-1460 (1992).

44. A. Rahman, F. H. Stillinger, *Journal of the American Chemical Society* **95**, 7943-7948 (1973).

45. F. H. Stillinger, *Science* **209**, 451-457 (1980).

46. S. Sarig, in *Handbook of Crystal Growth 2 Bulk Crystal Growth Part B: Growth Mechanisms and Dynamics* D. T. J. Hurle, Ed. (North-Holland, New York, 1994), vol. 2,.

47. R. L. Christiansen, E. D. Sloan, in *Natural Gas Hydrates* E. D. Sloan, J. Hjappel, M. A. Hnatow, Eds. (New York Academy of Sciences, New York, 1994) pp. 283-305.

48. W. Stumm, *Chemistry of the solid-water interface* (Wiley-Interscience, New York, 1992).

49. N. Fukuta, *Journal of Meteorology* **15**, 17-26 (1958).

50. V. A. Garten, R. B. Head, *Nature* **205**, 160-162 (1965).

51. G. R. Edwards, L. F. Evans, *Transactions of the Faraday Society* **58**, 1649-1655 (1962).

52. W. Drost-Hansen, in *Biophysics of Water* F. Franks, Ed. (John Wiley & Sons Limited, New York, 1982).

53. R. L. Reed, L. R. Kelley, D. L. Neumann, R. H. Oelfke, W. D. Young, Some preliminay results from a pilot-size hydrate flow loop, E. D. Sloan, J. Happel, M. A. Hnatow, Eds., International Conference on Natural Gas Hydrates, New York (The New York Academy of Sciences, 1994).

54. R. Larsen, Y. M. Taras, C. A. Knight, E. D. J. Sloan, Growth and inhibition phenomena of single hydrate crystals, Meeting of the American Chemical Society, Division of Fuel Chemistry, San Francisco (1997).

55. J. Long, Ph.D., Colorado School of Mines (1990).

56. H. J. Ng, D. B. Robinson, New developments in the measurement and prediction of hydrate formation for processing needs, E. D. Sloan, J. Happel, M. A. Hnatow, Eds., International Conference on Natural Gas Hydrates, New York (The New York Academy of Sciences, 1994).

57. S. B. Cha, H. Ouar, T. R. Wildeman, E. D. Sloan, *Journal of Physical Chemistry* **92**, 6492-6494 (1988).

58. M. Bylov, P. Rasmussen, The effect of impurities on ethane hydrate induction times, Meeting of the American Chemical Society, Division of Fuel Chemistry, San Francisco (1997).

59. W. D. Young, How to characterize the effectiveness of kinetic hydrate inhibitors, E. D. Sloan, J. Happel, M. A. Hnatow, Eds., International Conference on Natural Gas Hydrates, New York (The New York Academy of Sciences, 1994).

60. J. Lederhos, E. D. Sloan, Transferrability of hydrate kinetic inhibitor results between bench scale apparatuses and a pilot scale flow loop, 2nd International Conference on Natural Gas Hydrates, Toulouse, France (1996).

Chapter 2 Experimental Methods

2.1 Introduction

The bulk of experimentation involved measuring the supercooling and induction time necessary for hydrate formation in solutions of varying composition. The method was straightforward: water with or without added particles was pressurized to 5.5 MPa and then linearly cooled until hydrate formed. The temperature of hydrate formation was measured and the supercooling calculated and converted to an induction time.

Much of this thesis work involved the design of the experimental apparatus. The high pressures and low temperatures necessary for hydrate formation complicated the design. The acidity of the carbon dioxide and water solutions and surface dependency of nucleation processes created additional design concerns. The central component of the experimental set-up, the reactor in which hydrate was formed, was modified several times over the course of the work. Although much preliminary work was carried out in an earlier design of the reactor, all of the experimental results presented here were obtained in the final reactor. Both designs will be shown to explain the evolution of the final design.

Experiments were performed with both carbon dioxide and methane with some differences in methodology resulting from the difference in phases between the liquid carbon dioxide and the gaseous methane under the temperature and pressures conditions of the experiments.

The particles used in the experiments were characterized with respect to physical and chemical properties that might affect their catalytic potential.

2.2 The High Pressure Reactor

2.2.1 General Comments

Hydrates were formed in a high-pressure reactor that was specifically designed by the author to meet the design criteria of strength, visibility, non-reactivity, economy and ability to withstand high pressures and low temperatures.

To satisfy these requirements, the reactor was fabricated from polycarbonate plastic. When polished, polycarbonate is nearly transparent, enabling the hydrate reaction to be visually monitored without installing windows. Polycarbonate is also inexpensive, compared to sapphire and steel, and easily machined.

The polycarbonate chamber was encased in a Plexiglas jacket. Cooling water circulated in the space between jacket and reactor.

Reactors were pressure tested to 1600 psi without failure, using water as the pressurizing medium to avoid the possibility of explosive failure.

2.2.2 Initial Reactor Design

The initial reactor was fabricated from two inch outside diameter polycarbonate stock cut to 5¾ inch lengths, and boring a one-inch hole to within 1¼ inches of the reactor bottom (Figure 2.1). The top one-inch of the bored center was tapped for screwing in the top stainless steel fitting through which gas was transferred.

The temperature probe was inserted through the side wall, in a 1/8 inch hole that was drilled and tapped about midway down the reactor, 3 inches from the bottom.

The top stainless steel fitting was 1½ inches in diameter (Figure 2.1). A single ¼ inch hole was drilled and tapped for ¼ inch NPT pipe fittings for transfer of pressurizing gas.

The Plexiglas jacket, measuring 3 inches in outside diameter and 6 inches in height, consisted of three parts that were sealed together with O-rings, enabling easy disassembly. A 1 inch opening was built into the casing wall for insertion of the

temperature probe. A removable Plexiglas-rubber-Plexiglas ring sequence sealed around this opening (Figure 2.1).

Because of the lengthy cleaning process, multiple reactors were built so that one would always be ready for use.

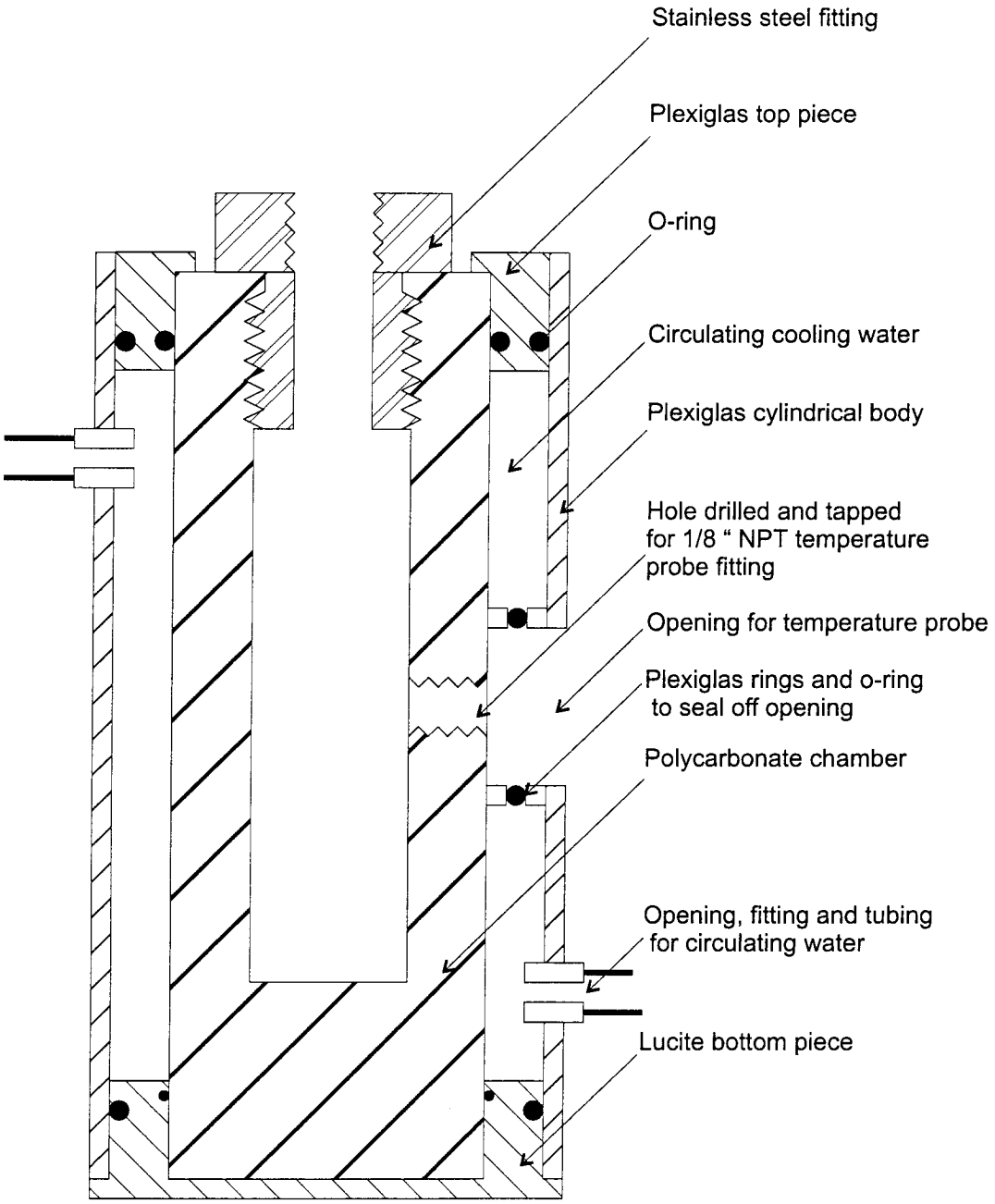

Figure 2.1: Initial reactor design. Showing stainless steel top fitting and cold bath casing.

2.2.3 Use of and Problems with Original Reactor

Initial supercooling experiments showed great variability in the supercooling needed to form hydrates. Many experiments were performed to determine whether improper reactor cleaning techniques or experimental methods caused this variability.

A very thorough reactor cleaning method was established. After each experiment, reactors were disassembled, rinsed out with deionized water and then with isopropyl alcohol to remove oil and grease, especially any ethylene glycol that might have contacted the chamber during disassembly. Chambers were then soaked in a one normal hydrochloric acid solution for two hours to remove any metals and oxides. The chambers were then rinsed in deionized water and then with Milli-q water. The Lucite cold bath parts were soaked in a Micro-90 cleaning solution (International Products Corp.) and thoroughly rinsed and dried to avoid contaminating inside of reactor with ethylene glycol. The top stainless steel fitting was cleaned by rinsing with deionized water and blowing through with compressed air (Air Liquide) for complete drying to prevent rust formation.

Even after implementation of this cleaning program, the measured supercooling still varied widely. After several experiments, the inside walls of the polycarbonate chamber suffered from pitting, crazing and eventual cracking. Though this could be due to the high acidity of the carbon dioxide and water solution, it was determined that most of this deterioration occurred during depressurizing, when lowered pressures were accompanied by reduced temperatures, causing a solid carbon dioxide phase to appear or hydrate phase to reappear. These solid phases would form in the reactor and prevent the depressurization of the reactor below the solid barrier. When the pressure differential below and above the barrier became too great, a small but powerful explosion would occur in the reactor, and though not forceful enough to destroy the reactor, the explosion did damage the interior walls. This damage was minimized by very slow depressurization after each experiment but was difficult to avoid completely.

Nucleation processes are surface dependent. The inside surface of the reactor was continually changing with the pitting and crazing of the polycarbonate surface. Suspecting that the changing surface was contributing to the problems with reproducibility, isolation of the hydrate forming solution from the polycarbonate walls was deemed necessary. The reactor design was modified to include the insertion of glass liners inside the polycarbonate chambers.

2.2.4 Final Reactor Design

The final reactor design was very similar to that already described but with the addition of a glass liner to isolate the hydrate forming solution from the polycarbonate wall. Other modifications included increasing the size of the reactor to accommodate the glass liner yet still provide the same internal reactor volume, and relocating the temperature probe to enter the top of the reactor.

The chamber was fabricated from 3¼ inch diameter Lexan (McMaster Carr), machine grade, polycarbonate rod. A 1½ inch hole was bored to within 1 inch of the reactor bottom, and the top 1 inch tapped for the top stainless steel fitting. Polishing the chamber ensured transparency and visibility. The chamber design is shown in Figure 2.2.

The polycarbonate chamber was encased in a Plexiglas jacket (Figure 2.2). This jacket was made of three pieces, top, bottom and cylindrical body, for easy disassembly. Watertight o-ring seals connected the three pieces. O-ring seals were also included between jacket bottom and top and chamber wall to prevent leakage of cooling water. Two ports were drilled in the jacket, as shown, for connecting the circulating water hoses.

Two ports were drilled in the top stainless steel fitting, one for the temperature probe and one for transferring gas into the reactor (Figure 2.3).

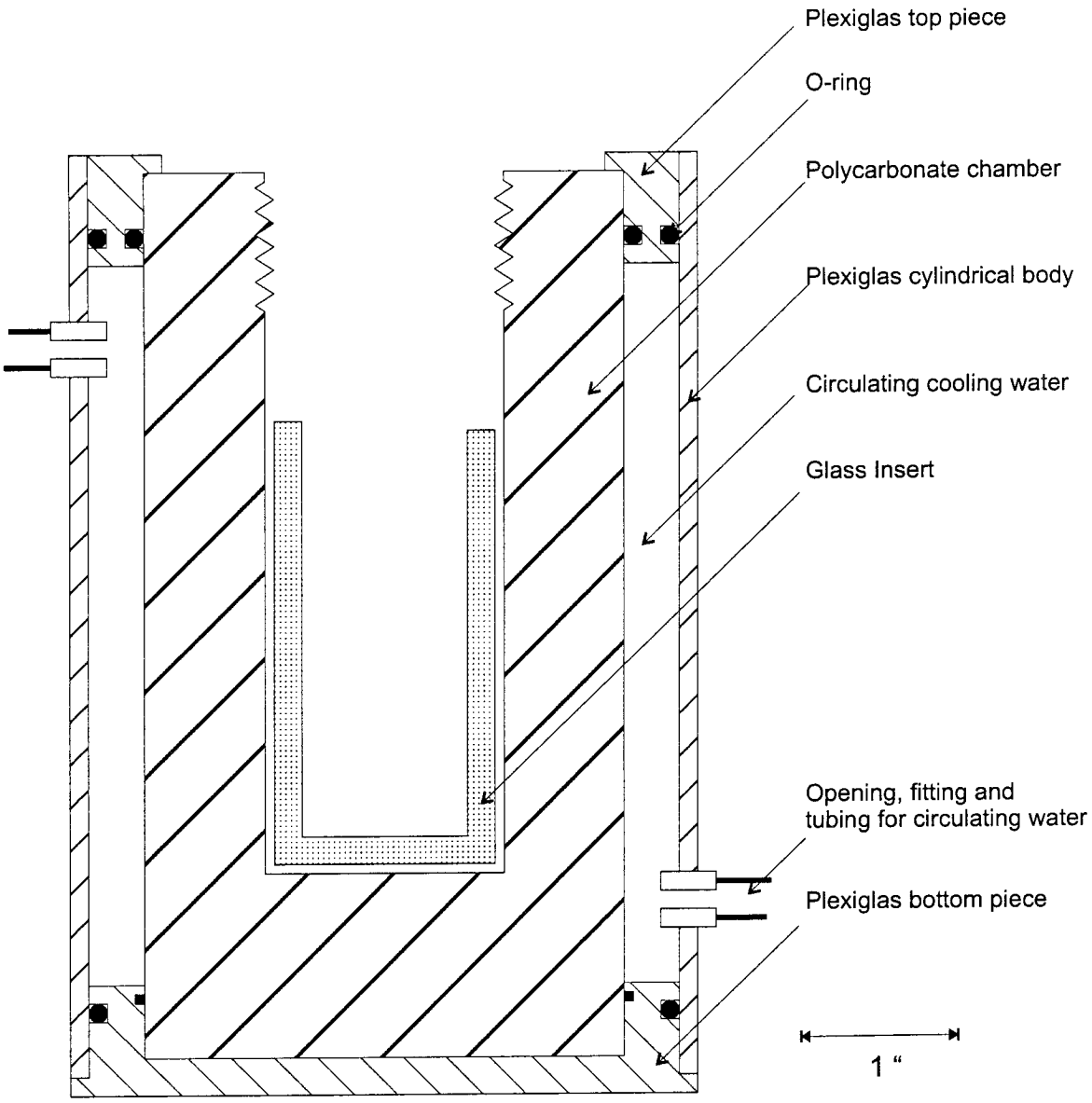

Figure 2.2: Reactor design showing polycarbonate chamber, glass insert and cold bath casing.

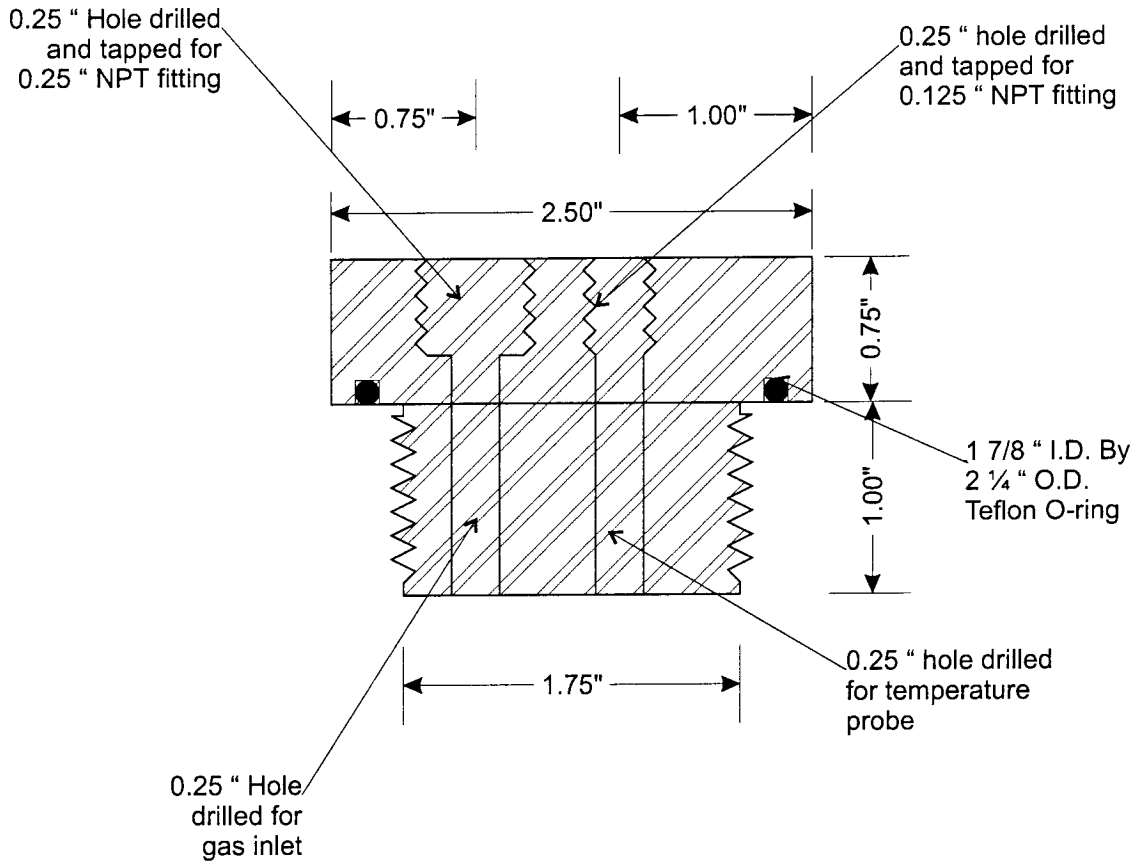

Figure 2.3: Stainless steel fitting showing two ports for transfer of pressurizing gas and insertion of temperature probe.

After prolonged use of the reactor, the top fitting was hard to unscrew and the threads in the polycarbonate were cracking. The reactor was modified once more to include a stainless steel sleeve that was screwed into the polycarbonate (Figure 2.4). Subsequently, the fitting was only screwed in and out of this sleeve, eliminating the wear on the polycarbonate threads. An O-ring was added to the bottom of the stainless steel fitting to seal between fitting and sleeve, yielding the final, complete reactor design (Figure 2.5).

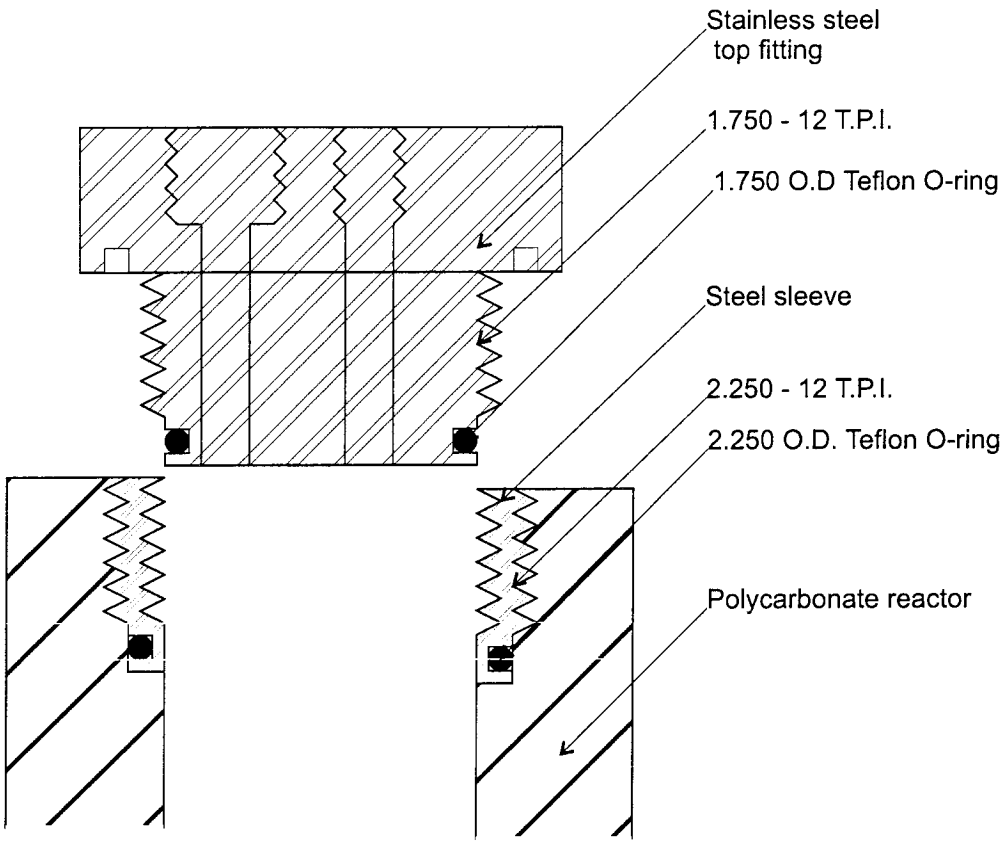

Figure 2.4: Steel Sleeve.

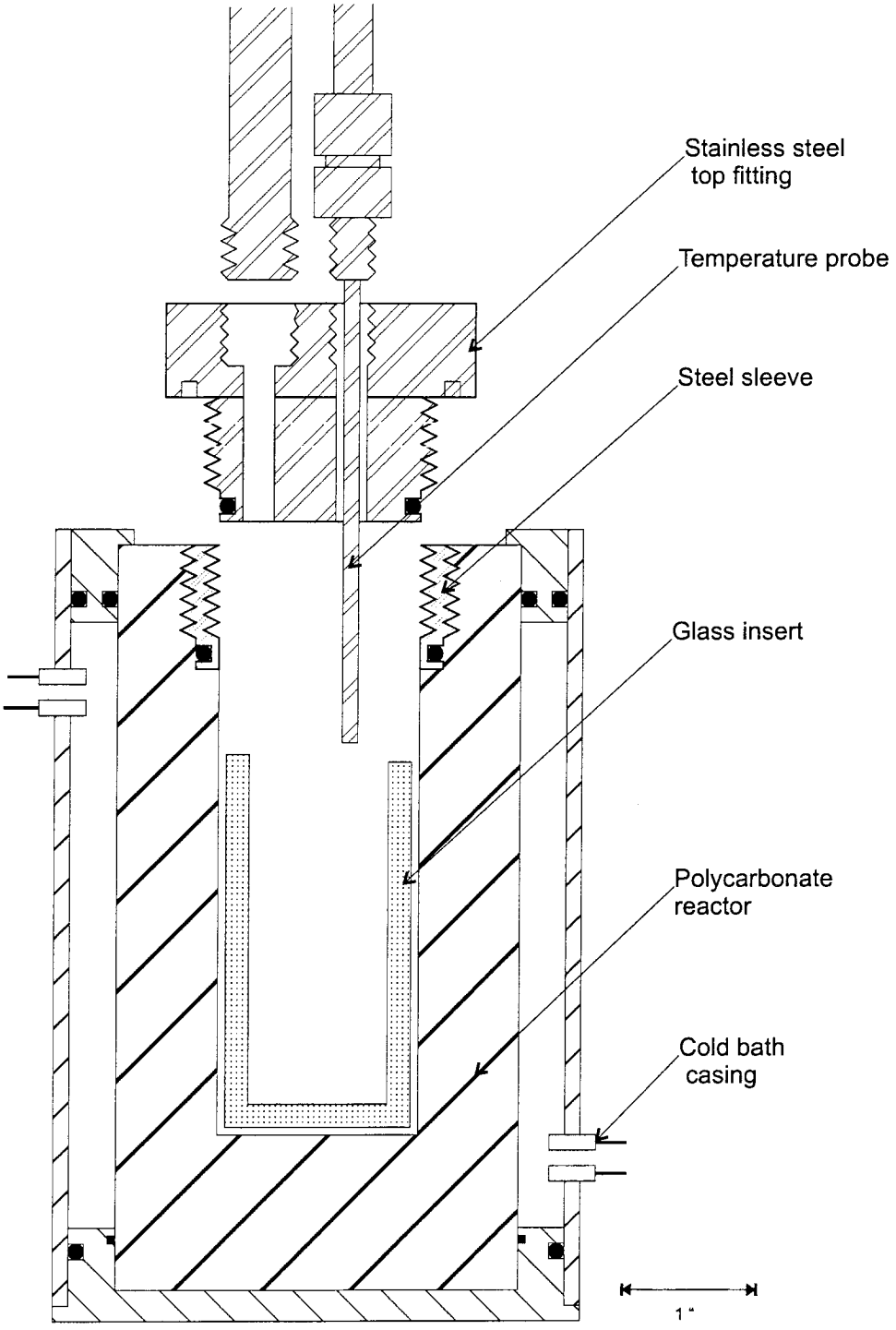

Figure 2.5: The final, complete reactor, showing glass liner, polycarbonate chamber, steel insert, temperature probe and gas inlet piping.

2.3 Experimental System

2.3.1 Pressure Control

The reactor was pressurized using the pressure of the hydrate forming gas, carbon dioxide or methane. The gas was transferred from the source tank, through a Matheson model #3030 high outlet pressure regulator, 72 inches of ¼ inch Swagelok 7R Series Nylon 11 core tubing rated at 2750 psi, the pressure control valve, stainless steel pipe and finally through the ¼ inch port in the stainless steel reactor top (Figure 2.6).

Reactor pressure was maintained with an MKS Instruments, Inc., pressure control system. A MKS Baratron absolute pressure transducer model #750B with a pressure range up to 1000 psia and a 1% accuracy measured the reactor pressure. The DC pressure signal was transmitted to the PID control module, MKS type 250D pressure controller, which compared this signal to the set point and positioned the control valve so that it drove the actual pressure to the set pressure. The control valve used, an MKS type 248A, with a maximum flow rate of 200 sccm, was a modified solenoid valve that opened when supplied with a controlling current, causing gas flow. The complete system provided good pressure control for our system wherein a continuous gas consumption occurred due to gas dissolution and hydrate formation. Unfortunately, the system did not allow for degassing and therefore could not compensate for any sudden increases in pressure, such as changes associated with ice formation in some experiments.

The MKS pressure control system was certified calibrated when purchased; frequent checks against a calibrated pressure gauge showed no drift. The Mark 15 pressure probe readings did drift and were therefore frequently recalibrated at 800 psi against the MKS system.

2.3.2 Temperature Control

The polycarbonate chamber resided in a Lucite water bath casing with an approximately ½ inch space between outer wall of chamber and inner wall of Lucite. A VWR brand

Model #1157 high capacity heating/refrigerating circulating cold bath pumped water around the side walls of the inner chamber. The underside and top of the chamber were not directly cooled. The cooling solution was a 50/50% solution of water and ethylene glycol. The cold bath was equipped with RS-232 interface and PC software for controlling the cooling rate.

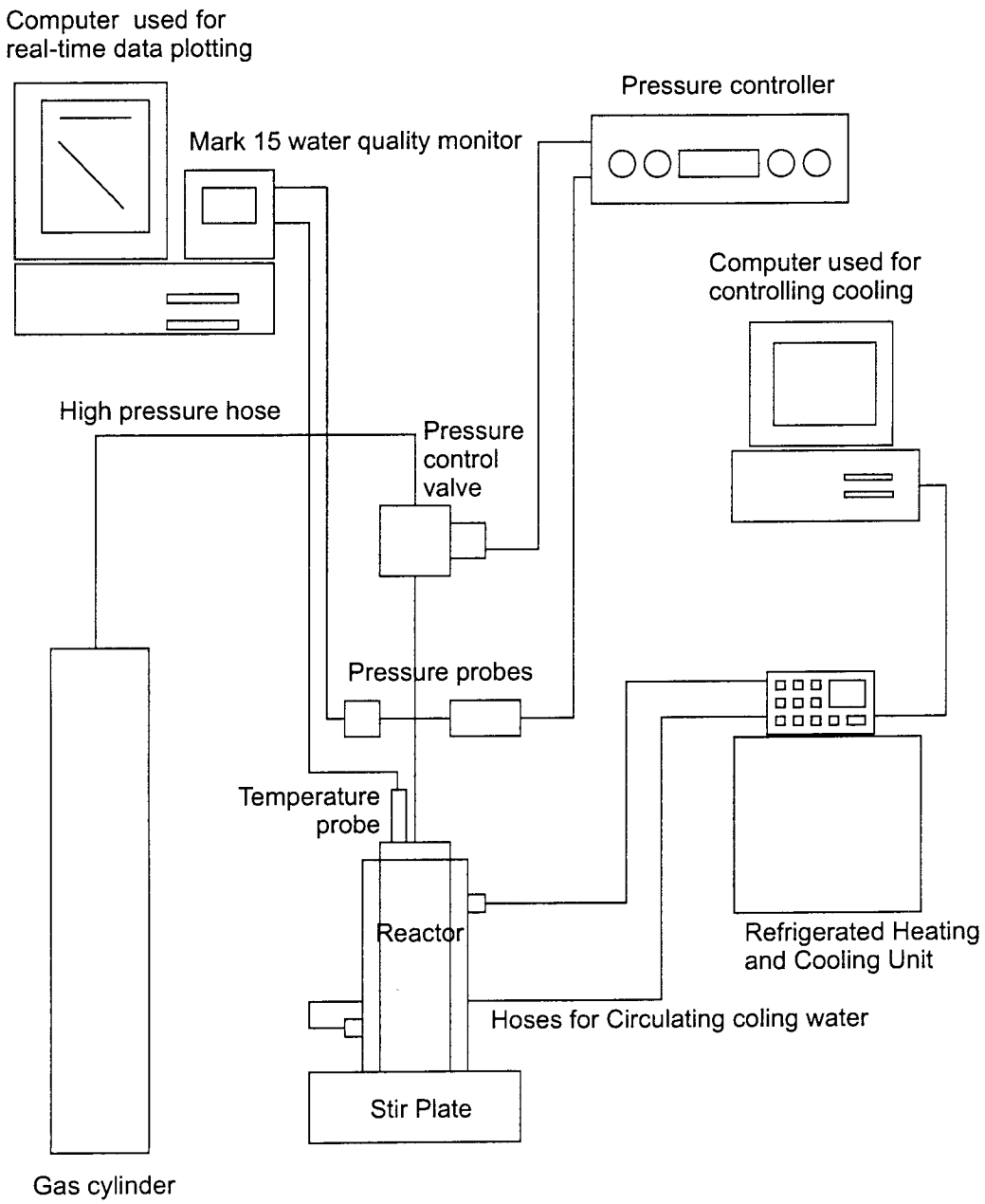

Figure 2.6: The experimental system.

2.3.3 Temperature and Pressure Measurement

Reactor pressure and temperature were measured by a Senso-Metrics Inc. model #SP91KFS high pressure probe and an RTD temperature probe respectively. The temperature probe was initially inserted through the chamber wall, directly into the hydrate forming solution. The temperature probe was subsequently relocated to the top stainless steel fitting, extending down into the solution. Both designs measured actual bulk solution temperature directly. All pressure probes measured pressure in the gas input piping leading to the chamber, thus avoiding large temperature effects on the pressure probes. Since there were no restrictions in the piping, this pressure was presumed identical to the pressure inside the chamber. These probes were connected to a Martek Instruments, Inc., Mark 15 water quality monitor that recorded pressure and temperature every 5 seconds.

The temperature probe was calibrated against an NIST certified thermometer at 0 and 15 ^{0}C using the cold bath. Temperature probe calibration was frequently checked but never needed recalibration.

2.3.4 Data Acquisition

The Mark 15 monitor was connected by RS-232 interface to an IBM PC AT computer for data acquisition. A Quick Basic program was written to plot the pressure and temperature data on the computer screen in real time and to save the data to file for further analysis.

2.3.5 Agitation

Reactor contents were mixed by a VWR brand magnetic stirrer model #400S. Stirring rate ranged from 60 to 2500 rpm, with LED display of speed for greater repeatability of stirring rate. Teflon coated VWR spinbar magnetic stir bars were used.

2.4 General Materials

2.4.1 Waters

Unless otherwise specified, pure, Milli-q (Millipore) water was always used. Milli-q water is deionized, 0.2 micron filtered and UV treated.

Artificial seawater was prepared using the recipe of Kester, Duedall, Connors and Pytkowicz [1] (Table 2.1). NaCl, Na_2SO_4, KCl, KBr and NaF were dried overnight at 110°C and then stored in a dessicator to be weighed in anhydrous form. $NaHCO_3$ and H_3BO_3 were weighed without drying. These salts were mixed in one flask in about 500 ml deionized water. 1.0 M stock solutions of $MgCl_2 \cdot 6H_2O$ and $CaCl_2 \cdot 2H_2O$ and a 0.1 M stock solution of $SrCl_2 \cdot 6H_2O$ were prepared. The correct volumes of these stock solutions were mixed and diluted to about 300 ml deionized water in another flask. The two solutions were then added together and made up with deionized water to 1.00 kg.

2.4.2 Gases

Carbon Dioxide was Air Liquide Coleman Instrument grade of 99.99% minimum purity. Methane was Matheson purity grade of minimum purity of 99.99%.

2.4.3 Inhibitor

Polyvinylpyrrolidone (PVP), a water soluble polymer from Aldrich with an average molecular weight of 55 000, was used as an inhibitor of hydrate formation. The chemical structure of PVP is:

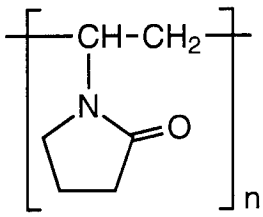

Table 2.1: Seawater Recipe, after Kester et al. [1].

Part A – Gravimetric Salts	
Compound	Concentration (g/kg of solution)
NaCl	23.926
$Na2SO_4$	4.008
KCl	0.677
$NaHCO_3$	0.196
KBr	0.098
H_3BO_3	0.026
NaF	0.003
Part B – Volumetric Salts	
Compound	Concentration (mol/kg of solution)
$MgCl_2 \cdot 6H_2O$	0.05327
$CaCl_2 \cdot 2H_2O$	0.01033
$SrCl_2 \cdot 6H_2O$	0.00009
Part C – Distilled water to 1000.000 g	

2.5 Particles

2.5.1 General Comments

Aluminum oxide, iron oxide, calcium carbonate, silicon dioxide, magnesium hydroxide and copper oxide particles were used in experiments. Particles were obtained from commercial manufacturers, with the exception of iron oxide, which was synthesized in the laboratory. A list of particles and their properties as reported by the manufacturer is presented in Table 2.2.

2.5.2 Characterization Methods

Because of the risk of losing fines in the cleaning procedures and the importance of having accurate size and surface area measurements, particles were re-characterized by transmission electron microscopy, Coulter counter, photon correlation spectroscopy, BET and electrophoretic mobility techniques.

Table 2.2: Particle properties as supplied by manufacturers, excluding synthesized Fe_2O_3.

Particle	Primary Particle Size (nm)	Surface Area (m^2/g)	Crystal Structure	Purity (%)
Al_2O_3				
Degussa C	13	85 - 115	γ	99.6
Linde A	300	14	90% α , 10% γ	99.98
Linde C	1000	3	100% α	99.98
Linde D	1000	15	90% α , 10% γ	99.98
Praxair B-AF	50	80	10% α , 90% γ	99.98
$CaCO_3$				
Aldrich 20, 293-2	n.a.	n.a.	n.a.	99.995
SiO_2				
Aerosil 380	7	350 - 410	amorphous	99.8 - 100.5
CuO				
Aldrich, 45, 080-4	n.a.	n.a.	n.a.	99.995

Note: n.a. = not available

Size Distributions

TEM size distributions were obtained on a Philips EM 430 Transmission Electron Microscope at 300 kV. Samples were prepared by suspending particles in water to make dilute suspensions that were then sonicated for one hour to break up any agglomerates. Using a fine wire, a drop of suspension was transferred to the surface of a porous carbon substrate, covering a copper grid. Excess water was drawn off with filter paper after 30 seconds and sample allowed to dry. Elemental analysis was performed by energy dispersive x-ray analysis using an EDAX 9900 system.

Particle size distributions were also obtained using a Malvern 4700 Photon Correlation Spectrometer with multi-angle capability and a Contin size analysis package. Samples were prepared by diluting particles with water in Nalgene tubes and then sonicating for one hour. Suspensions were transferred by pipette to clean quartz sample vials.

Particles larger than one micron were sized with a Coulter Counter Model T_{AII} multi-channel particle counter. Samples were prepared by suspending low concentrations

of particles in a 0.025 micron filtered 1% KCl solution and sonicating for one hour. Although repeatability of measurements on the same sample was excellent, obtaining high reproducibility of results from separately prepared samples proved difficult. Problems presumably arose due to coagulation of particles in the electrolyte solution. Unsonicated samples could not be measured as the particles immediately clogged the measuring orifice. Sonicating samples for at least one hour was necessary to eliminate this problem.

Surface Area

Surface areas were measured using the BET nitrogen gas adsorption method. Particles were dried overnight in a 70°C oven before measuring. Because of use constraints on the instrument, only two surface areas were measured, those of aluminum oxide Linde A and D. Other surface areas were calculated using assumed shapes and averaged particle sizes. These calculated, theoretical sizes were compared to values reported by the manufacturer and the most reasonable value chosen and used in all analyses.

Electrophoretic Mobility

Particle electrophoretic mobilities were measured on a Mark II particle micro-electrophoresis apparatus (Rank Brothers, London), using a flat cell. Suspensions were sonicated before measurements and dilute particle concentrations were chosen to minimize particle coagulation during measurement. For determination of pH_{pzc}, the ionic strength of the medium was adjusted to 0.05 M with KCl. Twenty particles were counted in each direction.

2.5.3 Preparation and Properties

Iron Oxide Particles

Monodisperse α-Fe_2O_3 particles were synthesized from condensed ferric hydroxide gel. 100 ml of 5.4 N NaOH solution was slowly added to 100 ml of 2.0 M $FeCl_3$ solution in a 250 ml Pyrex bottle, stirred for 10 minutes and the highly viscous ferric hydraoxide gel was immediately heated to 100 °C for eight days in a closed Pyrex bottle. The synthesis method was developed by Sugimoto and Sakata [2] who, by TEM and x-ray diffractometry, found the iron oxide particles to be monodisperse, pseudocubic hematite, α-Fe_2O_3.

After synthesis, the hematite particles were washed by allowing particles to settle, decanting supernatant and re-suspending with fresh water. The cycle was repeated until particles no longer settled. Then the pH was adjusted to approximately the point of zero charge by adding micromolar NaOH (ascertained visually by a sudden change in suspension color indicating an increase in particle size from coagulation). Particles then coagulated and settled. Supernatant was discarded and particles re-suspended with water. The cycle was repeated several times before a final cleaning by dialysis. Particle suspension was then transferred to plastic Nalgene bottles, frozen overnight and lyophilized. Particles were stored in the tightly closed bottles in a dessicator.

TEM micrographs showed particles ranging in size from 58 nm to 218 nm, with an average particle size by number of 120.0 nm (Figure 2.7). Micrographs were very clear and particles distinct, thus easily measured from the TEM negatives with a micrometer eyepiece. Crystals were pseudocubic or pseudorhombic. Particles clumped together, probably an effect of drying and high concentration rather than aggregation.

From the particle size distribution, an average particle size, weighted by surface area, was calculated to be 131.7 nm. With the assumption of cubic particles, a theoretical surface area was calculated:

$$S.A. = \frac{6d^2}{\rho d^3} = \frac{6}{\rho d}$$

where ρ = particle density (5.26 g/cm^3) and d = average particle diameter (131.7 nm). Calculated specific surface area was 8.66 m^2/g.

PCS analysis was inconclusive, showing possible dust contamination, and was therefore discounted.

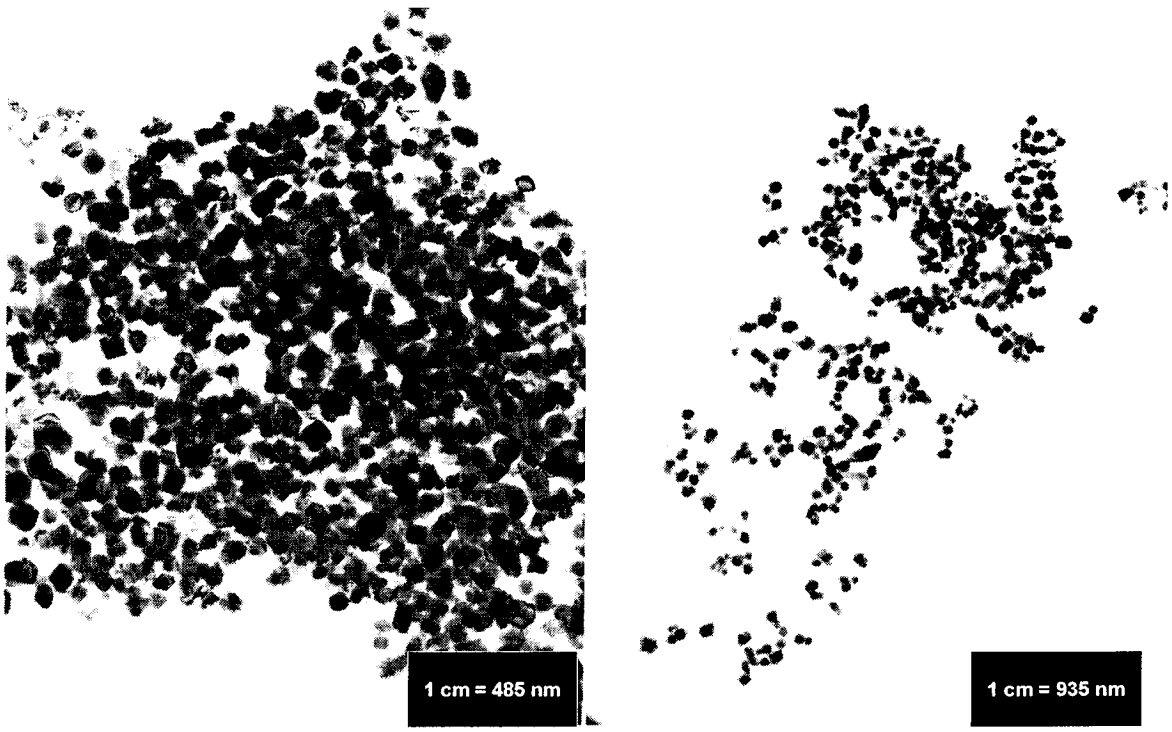

Figure 2.7: TEM micrographs of Fe_2O_3 particles.

Aluminum Oxide Particles

Degussa aluminum oxide C particles, with a reported average primary particle size of 13 nm and a surface area ranging from 85 to 115 m^2/g, were chosen for their high surface area. The oxide particles have a gamma crystal structure and a chemical purity of 99.6%.

These aluminum oxide particles were used without treatment in the methane hydrate experiments but were prewashed for the carbon dioxide experiments, using Schlautman's method [3]. The particles were washed in 0.1 M NaOH for two hours, rinsed once with water and then washed in 0.1 M HCl for thirty minutes. The particles

were centrifuged and the supernatant discarded. The particles were scraped from the centrifuge tubes and re-suspended in fresh water. Rinsing was repeated until the conductivity of the supernatant decreased approximately to that of distilled water. The washed particles were then re-suspended in water, frozen and dried by lyophilizing and then stored in a dessicator to prevent moisture absorption.

The average primary particle size of Degussa aluminum oxide measured from the TEM micrographs was 11.5 nm, agreeing well with the reported size of 13 nm (Figure 2.8). Assuming spherical particles, the theoretical surface area (S.A.) was calculated according to:

$$S.A. = \frac{1}{\rho}\frac{\pi d^2}{\frac{\pi d^3}{6}} = \frac{6}{\rho d}$$

where d = average particle diameter (11.5 nm) and ρ = particle density (3.2 g/cm^3) as reported by the manufacturer. Calculated surface area was 163 m^2/g. Since the measured and reported sizes agreed well but the calculated and reported, 85 to 115 m^2/g, surface areas differed greatly, the average reported BET surface area, 100 m^2/g, was used in analyses.

The size distribution of particles from the PCS analysis was cut off at the lower end. The instrument is capable of sizing particles down to 3 nm so the instrument must have been set incorrectly during the measurements. The analysis was not repeated and the data were not used.

A series of Linde (A, C and D) aluminum oxide particles of larger crystal size and smaller surface area were obtained from Union Carbide. These oxide particles were of high purity, 99.98%.

Linde A, C and D particles were also washed by Schlautman's method of NaOH followed by HCl. The slurry consistency of these particles differed from that of the Degussa aluminum oxide and prohibited separation of particles from supernatant by centrifuging. Linde A aluminum oxide was repeatedly filtered through 0.05 micron

polycarbonate membrane filters and re-suspended with fresh water until the filtrate conductivity was substantially decreased. The highly concentrated slurry was then dialyzed until conductivity of rinse water approached that of distilled water. Linde C was cleaned entirely by the above filtration process without dialysis. Linde D was rinsed entirely by dialysis, without first centrifuging or filtering. The difference in cleaning techniques was partly due to equipment limitations and partly due to differences in suspension consistencies, Linde D being particularly viscous and not lending itself to filtration. All three particle suspensions were transferred to clean HDPE plastic bottles, frozen overnight, dried by lyophilizing and stored in a dessicator.

Linde A, C and D all showed very wide size and shape distributions.

The TEM micrographs of Linde A aluminum oxide showed a trimodal distribution, with some very fine particles, some large fused particles and other medium sized particles (Figure 2.11). The fine particles were too small to be measured. Typical secondary particles, about 300 nm in width, were composed of smaller, apparently fused, primary particles. The particles appeared highly aggregated. The larger fused particles were measured, yielding a calculated average size of 268.8 nm. The PCS analysis showed a monomodal distribution with an average size of 317.0 nm. TEM and PCS size analyses agreed well with each other and with the manufacturer's reported size of 300 nm.

TEM micrographs of Linde C aluminum oxide showed a bimodal distribution with secondary particles in the same size range as Linde A with similar fines (Figure 2.9). The fines appeared attached to the faces of the Linde C secondary particles. One of the micrographs showed unidentified sheets but these were rare occurrences. The secondary particles were apparently aggregated. Sizing by TEM gave a mean secondary particle size of 317 nm. PCS analysis also yielded a similar mean particle size, 360.9 nm. This result differed substantially from the reported size of 1.0 micron.

Linde D aluminum oxide particles were very widely distributed both in shape and size. PCS analysis showed a bimodal size distribution with an average particle size by

surface area of 352.5 nm. TEM micrographs showed large fused particles with an average size of 263.4 nm (Figure 2.10). The fines present in Linde A and C were mostly missing from Linde D.

Because shapes of the Linde A, C and D secondary particles were highly irregular, surface areas were not calculated by using the average particle size and assuming an average particle shape. The measured BET surface area of Linde A aluminum oxide was 12.42 ± 0.03 m^2/g and that of Linde D was 7.90 ± 0.07 m^2/g. The reported surface area of 3 m^2/g was used for Linde C.

A final aluminum oxide, B-AF, with properties similar to that of the Degussa aluminum oxide was obtained from Praxair. Reported surface area was 80 m^2/g, particle size 50 nm, crystal phase mostly γ and purity 99.98%. This particle was used without any pretreatment.

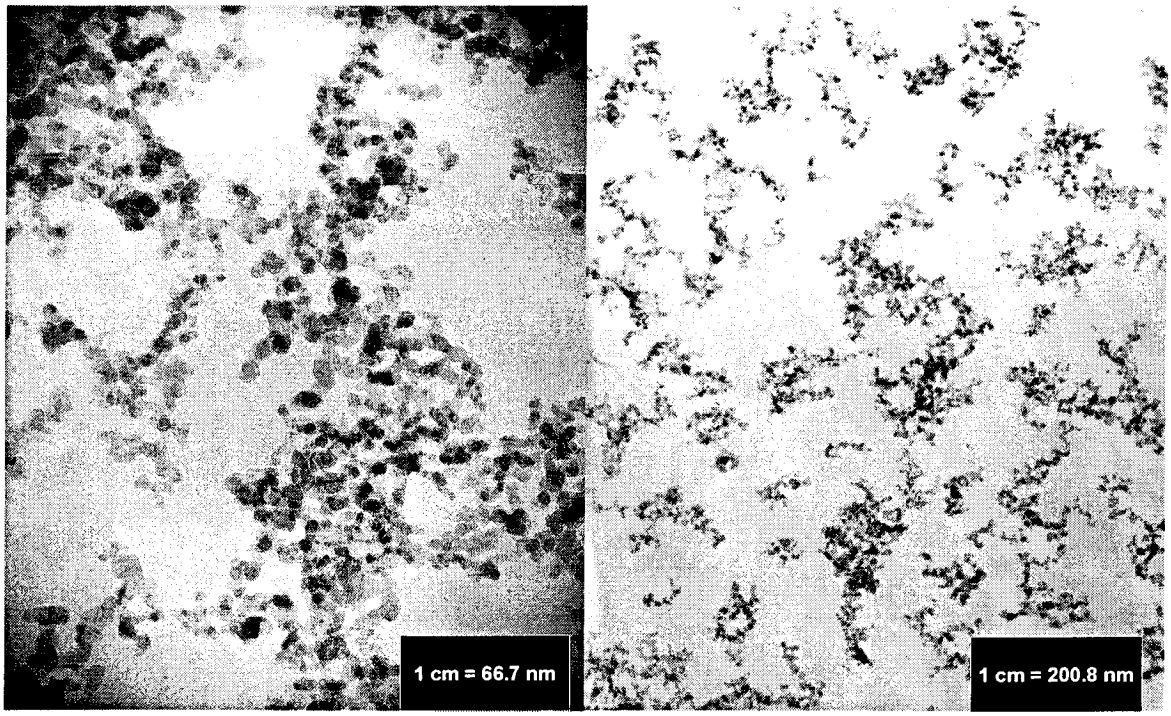

Figure 2.8: TEM micrographs of Degussa C Al_2O_3 particles.

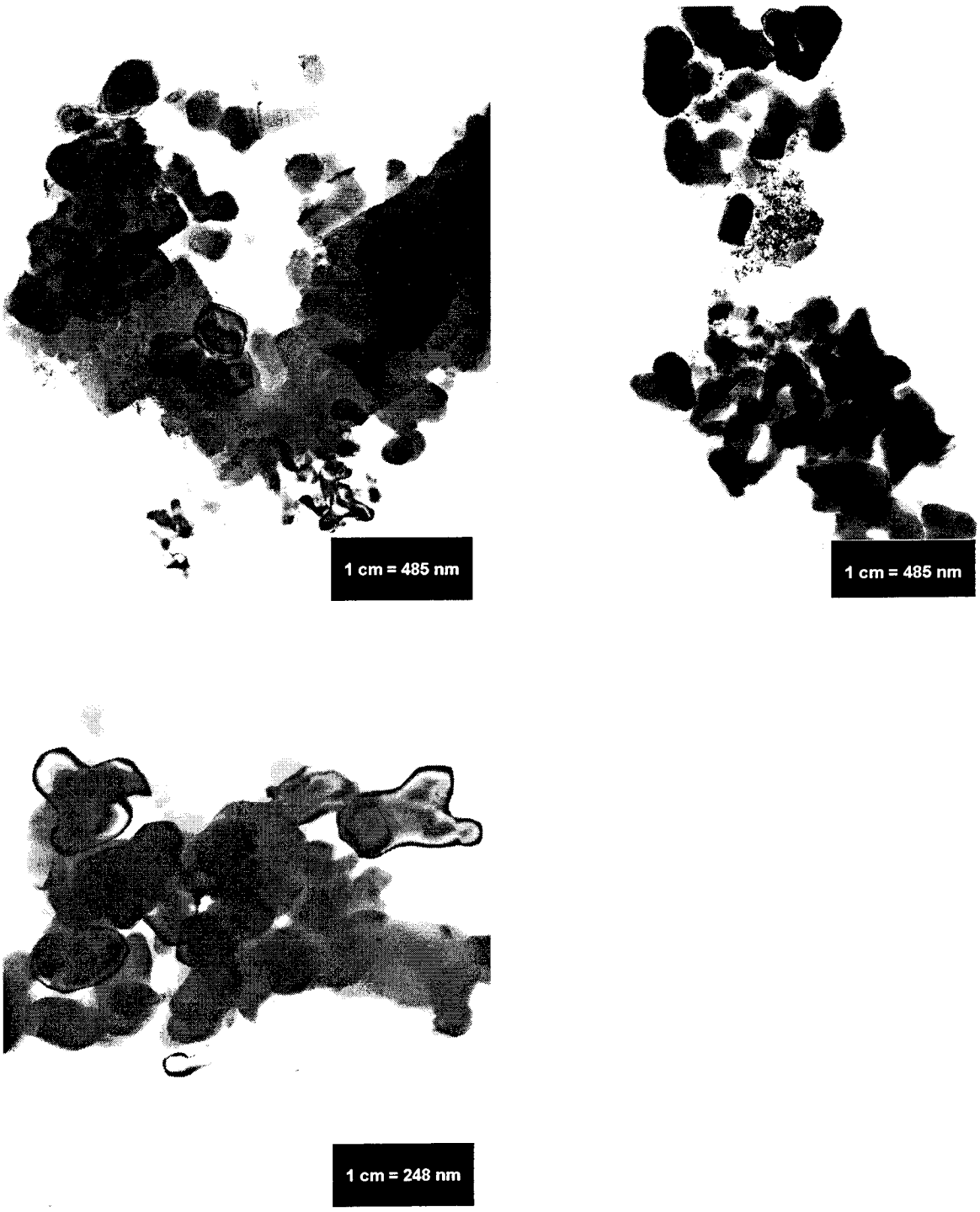

Figure 2.9: TEM micrographs of Linde C Al_2O_3 showing possible sheet-like impurity (top left), fines and larger particles (top right) and bulk particles (bottom).

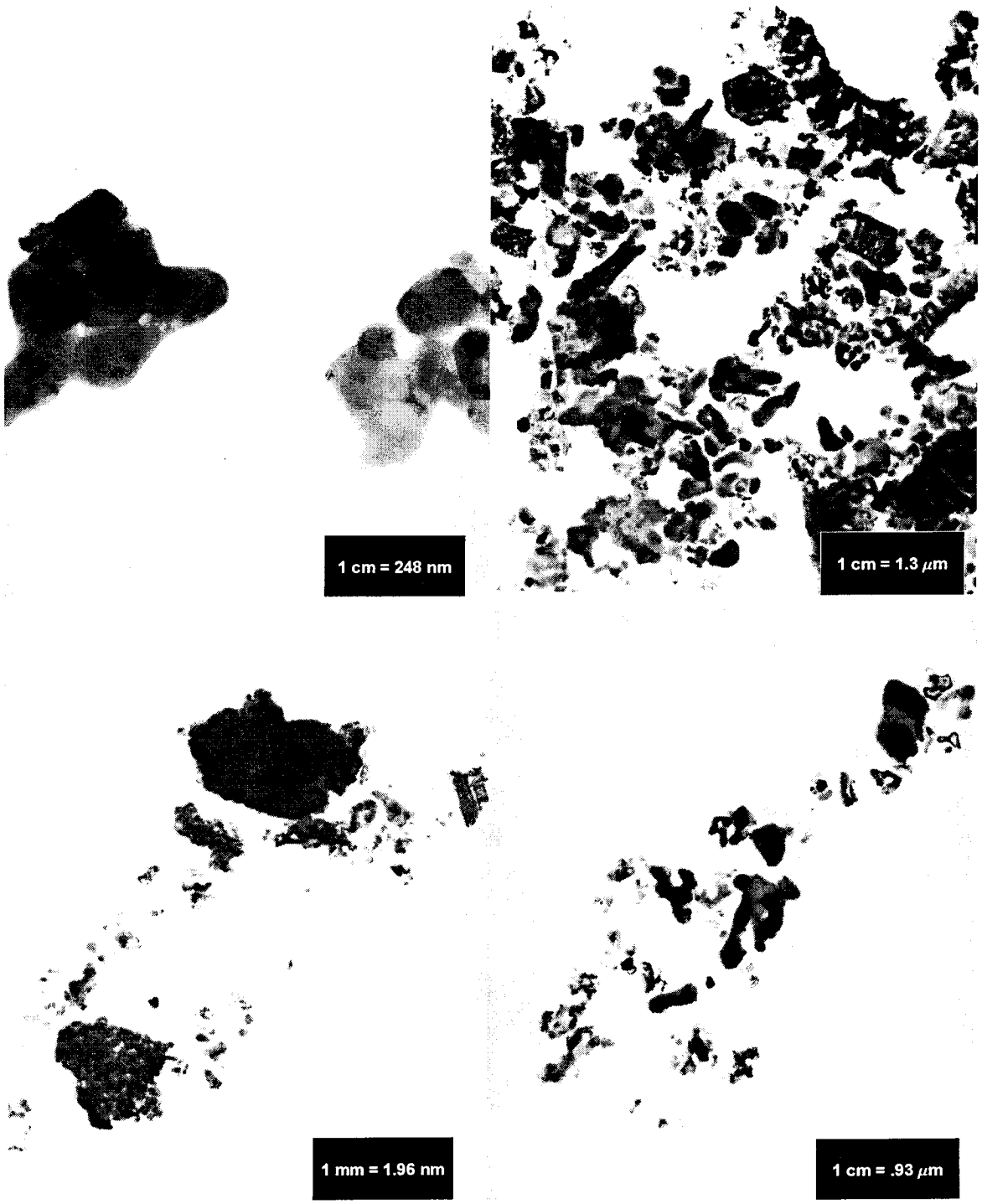

Figure 2.10: TEM micrographs of Linde D Al_2O_3 particles.

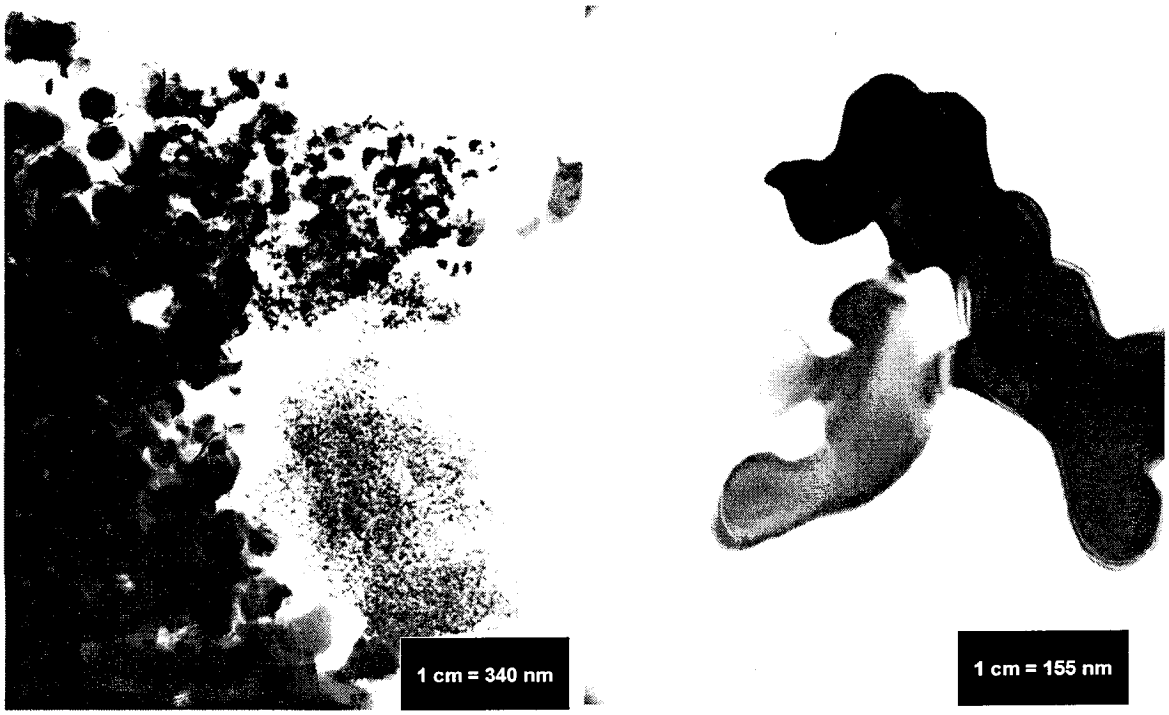

Figure 2.11: TEM micrographs of Linde A Al_2O_3 particles showing trimodal distribution (left) and "limbs" (right).

Silicon Dioxide Particles

Silica particles were purchased from Degussa as Aerosil 380. The reported average particle size was 7 nm with surface areas of 350 to 410 m^2/g. The particles were amorphous and 99.6% pure.

Silica particles were stored in a dessicator to prevent moisture absorption and used without further treatment.

The average primary particle size of silicon dioxide measured from the TEM micrographs was 17.5 nm, larger but approximating the reported size of 7 nm (Figure 2.12). The theoretical surface area was calculated assuming spherical particles as above, with d = 17.5 nm and ρ = 2.2 g/cm^3. Calculated surface area was 155 m^2/g, which differed from the BET surface area reported by the manufacturer, 350 to 410 m^2/g. The average BET surface area of 380 m^2/g was used instead of the theoretical specific surface area.

The same problem was encountered with the PCS measurements as for the Degussa aluminum particles and therefore the data were discounted.

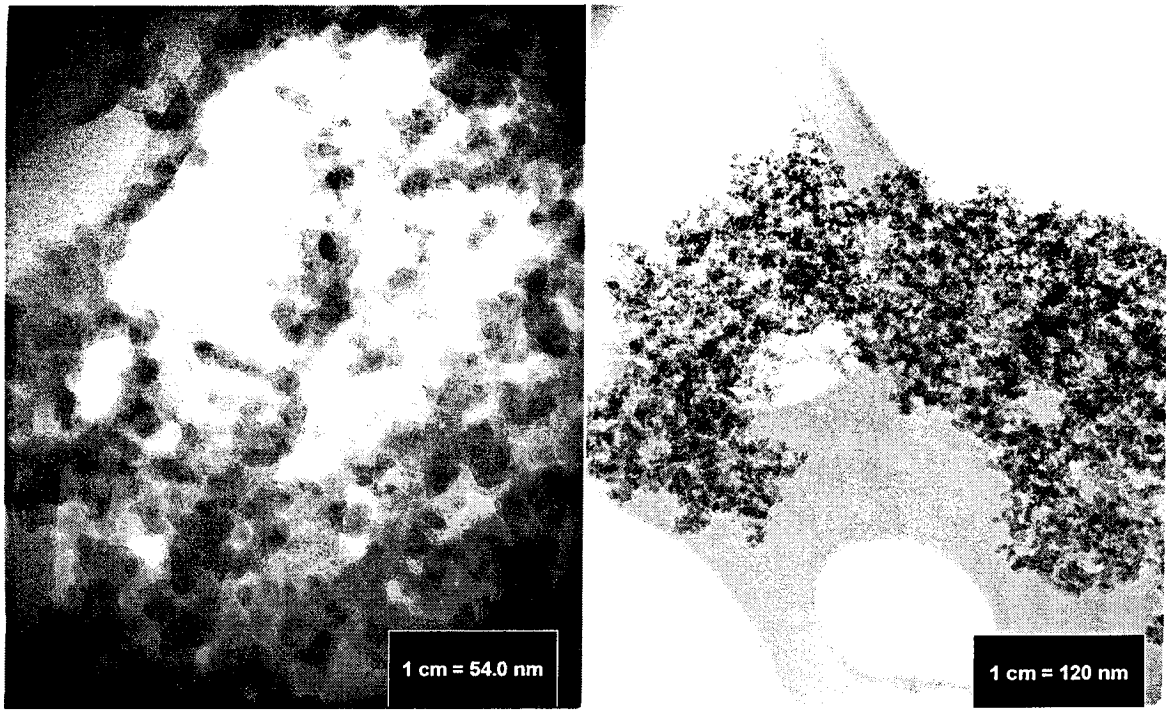

Figure 2.12: TEM micrographs of SiO_2 particles.

Calcium Carbonate Particles

Calcium carbonate particles used in experiments with methane gas were purchased from Mallinckrodt. The particles were in powder form and were used without further preparation or characterization.

For later experiments with carbon dioxide, higher purity (99.995+%) particles from Aldrich Chem Co. were used. Average particle sizes ranging from 1.91 to 4.65 microns (varying with sample) were measured with the Coulter Counter. Mass specific surface areas were calculated from the particle size distributions according to

$$S.A. = \frac{6}{\rho} \frac{\sum_{r=0}^{\max} m_r d_r^2}{\sum_{r=0}^{\max} m_r d_r^3}$$

where particles of size d_r constitute a fraction m_r, of the total number N in the sample and assuming spherical particles. The manufacturer's reported density of 2.930 g/cm^3 was used. Mass specific surface areas ranged from 1.59 to 3.06 m^2/g. By sonicating for one hour and then diluting sample, consistent surface areas of approximately 1.6 m^2/g were obtained and therefore this value of 1.6 m^2/g was used in all analyses.

Magnesium Hydroxide Particles

Magnesium hydroxide particles (Alpha Aesar) were sized by the Coulter Counter particle counting technique. An average size of 1 to 2 microns was measured and, assuming spherical particles and the density of Brucite reported in the literature, 2.39 g/cm^3, the mass specific surface area was 2 to 3 m^2/g. A value of 2.0 m^2/g was used in all analyses.

2.6 Methodology

2.6.1 Reactor Cleaning and Preparation

The polycarbonate reactor itself was rinsed thoroughly with Milli-q water and wiped dry with lint free paper. The top fitting pipe and probe assembly was rinsed out with deionized water and dried with compressed air. The threaded part of the assembly and the temperature probe were rinsed out with Milli-q water and dried with lint free paper.

The inserts were thoroughly rinsed with deionized water. If the glass insert were used with a particle suspension, the insert was wiped out with a clean cloth and re-rinsed. The inserts were then washed with acetone and again rinsed with deionized water to remove any organic materials. The inserts were then sonicated in deionized water for at least two hours to re-suspend any attached particles and again rinsed to remove these particles. If aluminum oxide particles had been used in the previous experiment, the inserts were again sonicated in a 20% sodium potassium tartrate solution to complex any residual aluminum and then these complexes were rinsed away. The final washing step consisted of overnight soaking, at least eight hours, in a 1 N hydrochloric acid bath. The inserts were then rinsed with deionized water and finally with Milli-q water.

2.6.2 Experimental Run

Reactors were prepared in a clean room to minimize contamination.

Particle suspensions were made by weighing the needed mass of particles, transferring the particles to a glass insert and adding 25 ml of water by pipette. In rare cases of more dilute (less than 0.1 g/l) particle suspensions, stock solutions were made and 25 ml of the stock solution were pipetted directly into a glass insert. After adding a Teflon coated stir bar, the insert was carefully lowered into the polycarbonate reactor. The top pipe and probe assembly was installed and the signal wiring for the temperature and pressure probes and pressure control system was connected. Dissolved gases were evacuated by vacuum pump connected to the gas outlet valve on the reactor.

For all methane experiments, the solution was stirred at 500 rpm, the maximum speed at which the stir bars remained centered. Stirring speed was reduced to 450 rpm for all carbon dioxide experiments because the liquid carbon dioxide droplets in the solution destabilized the stir bar at higher speeds.

Temperature of the cooling water was controlled by a computer programmed to cool at a rate of 5 °C per hour. Insulation by the polycarbonate walls and loss of heat to the surroundings caused the actual cooling rate of the reactor contents to lag, by about 6 °C, behind the temperature of the cooling water and to vary slightly from the programmed cooling rate. For this reason, experiments were begun with the reaction solution 6 °C warmer than the circulating water to ensure linear cooling. For methane experiments, the cold bath was initially adjusted to 5 °C and the reactor was pressurized when the solution had cooled to 11 °C. For carbon dioxide experiments, cold bath was adjusted to 10 °C and reactor pressurized when solution temperature decreased to 16 °C. The experimental procedure for a typical carbon dioxide hydrate formation experiment is shown in Figure 2.13 and for a typical methane experiment in Figure 2.14.

The reactor was pressurized with the hydrate forming gas, either carbon dioxide or methane, to 5.5 MPa (800 psi). Pressurization increased temperature. Once

temperature returned to the set value, the cold bath cooling system was activated. The above cooling method resulted in a linear cooling rate of reactor contents. For the methane systems, this cooling rate varied between 0.070 °C/min (4.19 °C/hour) and 0.081 °C/min (4.88 °C/hour), with an average of 0.074 ± 0.003 °C/min (4.46 ± 0.19 °C/hour). For the carbon dioxide systems, this cooling rate varied between 0.080 °C/min (4.78 °C/hour) and 0.108 °C/min (6.50 °C/hour), with an average of 0.089 ± 0.005 °C/min (5.36 ± 0.27 °C/hour)

Pressure and temperature were recorded every five seconds and their values plotted on a computer screen throughout the experiment for easy visual monitoring. Time, pressure and temperature data were also saved to a file for further analysis. The temperature and pressure traces for a typical hydrate formation experiment with carbon dioxide are shown in Figure 2.13 and with methane in Figure 2.14.

Hydrate formation was ascertained by visual inspection. The appearance of the hydrate forming solution changed markedly upon hydrate formation, becoming solid and more opaque. As the reaction is exothermic, hydrate formation was also usually accompanied by a noticeable temperature increase (Figure 2.13 and Figure 2.14). Data were recorded for several minutes after hydrate formation to include the temperature spike. Data logging then ceased and the reactor depressurized, disassembled and washed as already outlined.

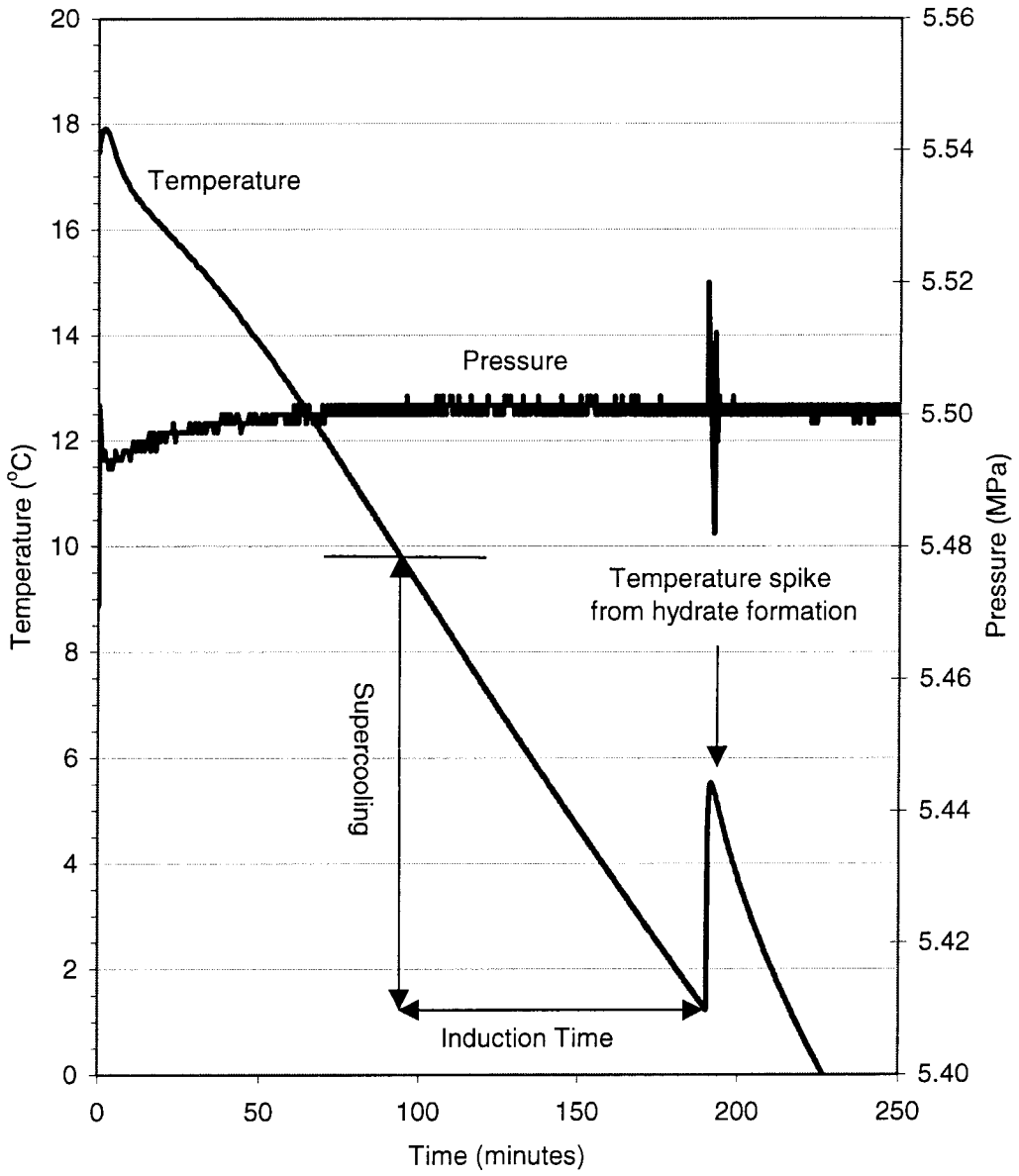

Figure 2.13: Pressure and temperature history for a typical carbon dioxide hydrate formation experiment showing temperature spike at hydrate formation.

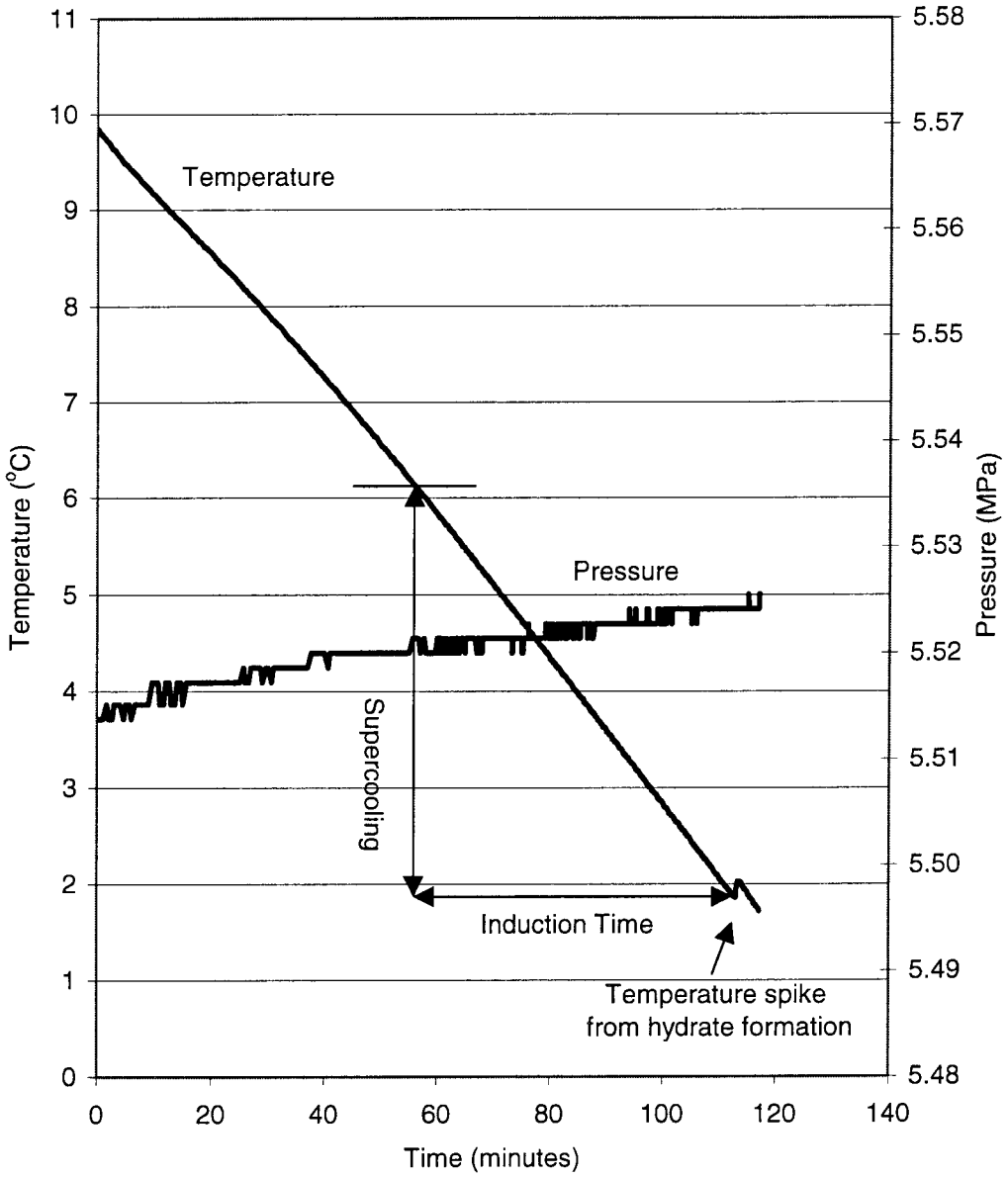

Figure 2.14: Pressure and temperature history for a typical methane formation experiment showing temperature spike at hydrate formation.

2.6.3 Experimental Protocol

Supercooling values and induction times were calculated from the temperature of hydrate formation.

Supercooling is a measure of the driving force needed to overcome the energy barrier to hydrate nucleation. Supercooling is the difference between the equilibrium temperature for hydrate formation at the experimental pressure of 5.5 MPa (800 psi) and the actual experimental temperature of hydrate formation (Figure 2.15):

$$\text{Supercooling} = T_{equilibrium} - T_{formation}$$

The equilibrium temperature was obtained from a regression on equilibrium data for the hydrate-liquid water-gaseous methane or liquid carbon dioxide phase line from the literature.

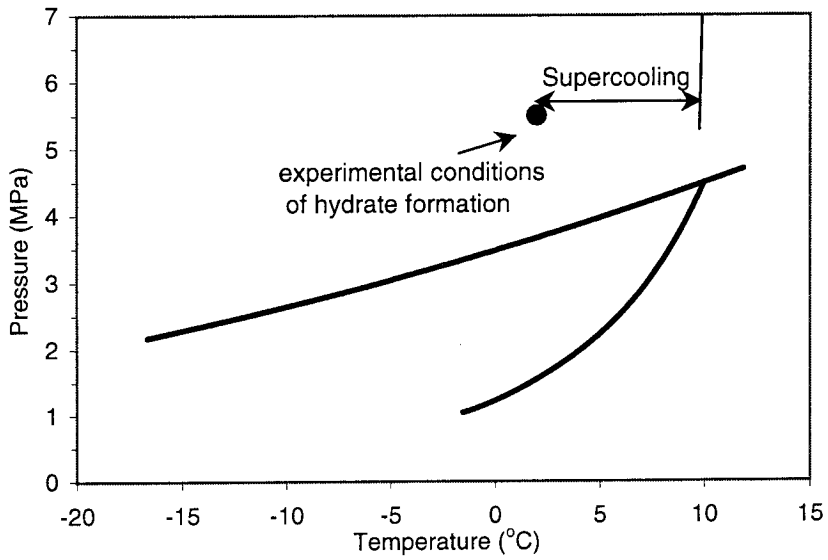

Figure 2.15: Definition of supercooling with respect to the phase diagram of CO_2.

The induction time for hydrate formation is the time that it takes hydrate to form once equilibrium conditions have been reached. Induction times were calculated by dividing the supercooling by the cooling rate:

$$\text{Induction time} = \frac{\text{Supercooling}}{\text{Cooling Rate}}$$

The induction time is a transformation of supercooling data from a temperature scale to a time scale using the cooling rate, and is therefore dependent on the cooling rate. This relationship is graphically shown in Figures 2.13 and 2.14. Cooling rates were individually calculated for each experiment by a linear regression fit to the cooling curve. This atypical definition of induction time is only used by hydrate researchers. It should not be confused with the standard measurement of induction time as the time to hydrate formation once specific temperature and pressure conditions are set and held constant.

Because the degree of supercooling is the more fundamental chemical variable, experimental results are presented in terms of supercooling. Induction times corresponding to the degree of supercooling with the experimental cooling rate are also sometimes reported.

Because of the large variability in experimental results, experiments were performed in replicate and average values of supercooling and induction times reported. Normally, at least five experiments were performed under each set of conditions. Data sets for control experiments without particles were larger, including 26 and 10 experiments for methane and carbon dioxide respectively.

The Kolmogorov-Smirnov test for normality of data was performed on control sets, ensuring normality of data so that parametric statistical analyses could be performed. Supercooling and induction time values were usually reported as averages and reproducibility by standard deviation. Analysis of variance was performed to test for dissimilarity among data points and the Tukey test was used to determine statistically significant differences among data points. Statistical tests were performed at 5% confidence levels.

2.7 References

1. J. P. Bidwell, S. Spotte, *Artificial Seawaters. Formulas and Methods* (Jones and Bartlett Publishers, Inc., Boston, 1985).

2. T. Sugimoto, K. Sakata, *Journal of Colloid and Interface Science* **152**, 587-590 (1992).

3. M. Schlautman, Ph.D. Thesis, California Institute of Technology (1992).

Chapter 3 Experimental Results

3.1 Methane Hydrate

3.1.1 Qualitative Observations

Methane hydrate always formed first at the boundary between methane gas and liquid water. Hydrate formed as a film on the interface. Mixing was sufficient to form a vortex, and the interface solidified in the shape of the vortex. The higher the formation temperature, the less hydrate appeared to form, producing a very thin and weak film that was initially broken up by the mixing. Hydrate continued to grow and after about 20 seconds, the film solidified and remained intact. At lower formation temperatures, the hydrate film grew rapidly and solidified in several seconds.

Immediately after initial hydrate formation, the bulk solution was clear and devoid of hydrate. Continued mixing appeared to cause hydrate erosion on the water side of the hydrate layer, bringing hydrate into the bulk solution. The bulk solution remained clear and liquid even after remaining for two days at elevated pressures and lowered temperatures in the hydrate stability region.

3.1.2 Control Experiments in Absence of Seed Particle

Hydrate formed from methane gas and liquid water at an average supercooling of 5.13 ^{o}C. This supercooling corresponds to an average induction time of 69.3 minutes. Variation in the data was large with a standard deviation of 1.19 ^{o}C for supercooling and 14.8 minutes for induction time. Twenty-eight experiments were run but two, NR157 and NR159, were discounted as hydrate failed to form before the water froze (leaving n, the number of experiments in a set = 26) (Figure 3.1).

The Kolmogorov-Smirnov goodness of fit test shows that supercooling temperatures were normally distributed with 5% confidence (Figure 3.2). This finding indicated that parametric statistics could be used to analyze results.

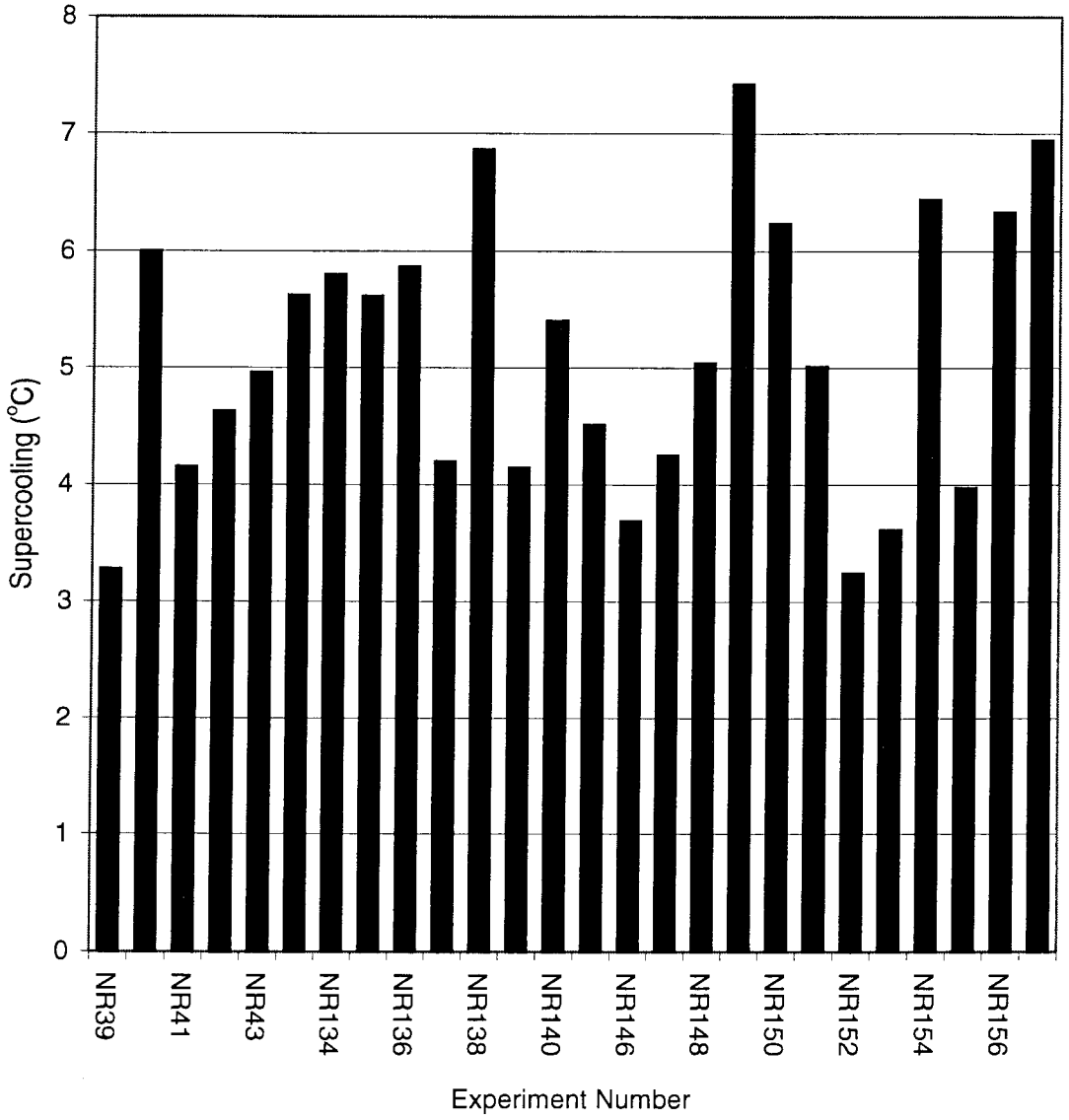

Figure 3.1: Supercooling values for methane hydrate formation in pure water (n=26).

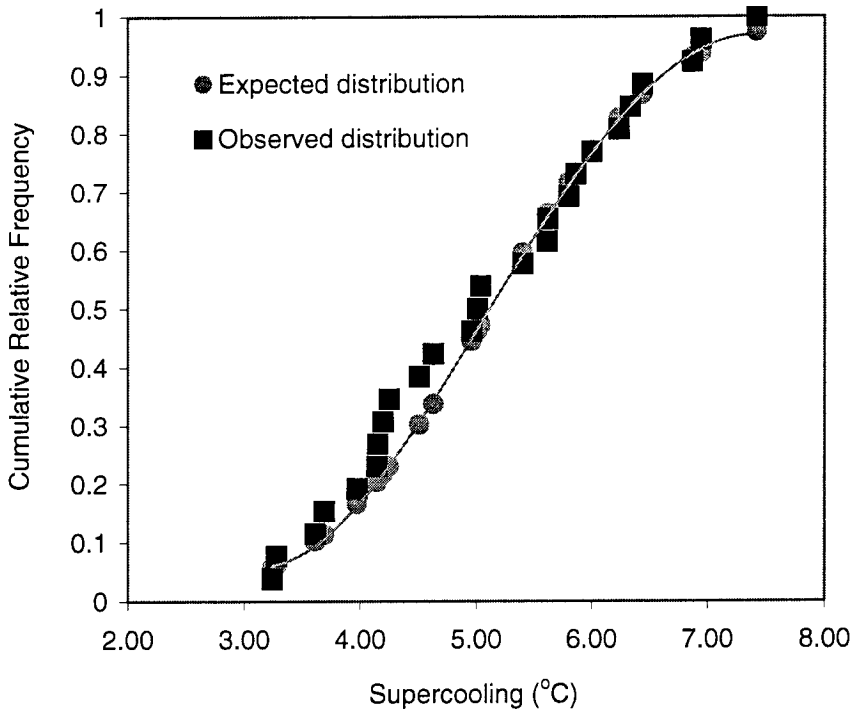

Figure 3.2: Cumulative frequency distribution of supercooling temperatures for hydrate formation from methane gas and pure water, used for the Kolmogorov-Smirnov goodness of fit test for normality of data. $d_{max\ observed} = 0.1165$ at a supercooling of 4.25 °C. $d_{max\ critical}$ (n=26, α=0.05) = 0.25908. Since $d_{max\ observed} < d_{max\ critical}$, accept at 5% confidence level hypothesis that the sample could come from a normal distribution with mean = 5.13 °C and standard deviation = 1.19 °C.

3.1.3 The Effect of Adding Particles

The addition of aluminum oxide and calcium carbonate particles to the hydrate forming solution decreased supercooling and induction time of methane hydrate formation. A 1 g/L suspension of unwashed Degussa aluminum oxide particles decreased the supercooling needed for hydrate formation by 44.8% to 2.83 °C and the induction time by 45.7%, to 38.0 minutes (Figure 3.3). The same concentration of calcium carbonate particles had a similar effect of decreasing the supercooling by 53.6% to 2.38 °C and decreasing the induction time by 53.4%, to 32.3 minutes (Figure 3.3).

The addition of these particles also increased reproducibility of the results. The standard deviation of supercooling values decreased from 1.19 °C in the unseeded system

to 0.49 °C and 0.35 °C in the systems seeded with aluminum oxide and calcium carbonate particles, respectively. Standard deviation of induction times decreased from 14.8 minutes in the unseeded system to 6.0 minutes and 5.4 minutes in the systems seeded with aluminum oxide and calcium carbonate, respectively.

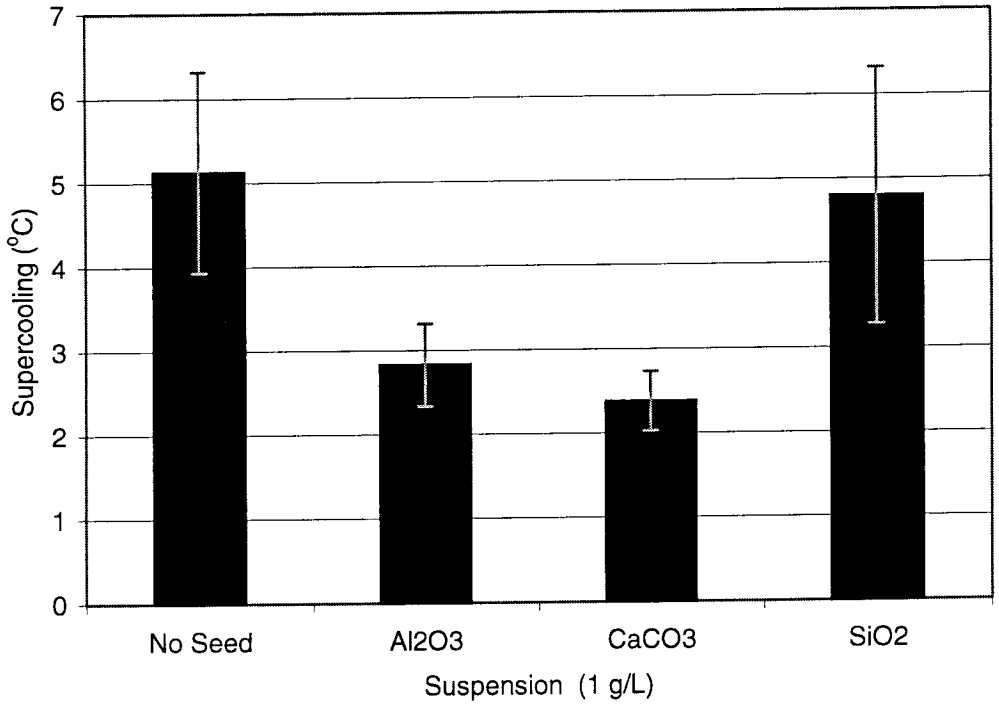

Figure 3.3: Comparison of supercooling values for methane hydrate formation in the unseeded system with those of seeded systems. Errors are presented as standard deviation (n=26 for no seed. n=5 for Al_2O_3 and $CaCO_3$ and n=10 for SiO_2).

The addition of silicon dioxide particles had no significant effect on the supercooling and induction times of methane hydrate formation and no effect on the reproducibility of results. The average supercooling needed for methane hydrate formation from a 1 g/L suspension of silica was 4.80 ± 1.52 °C. Average induction time was 66.0 minutes with a standard deviation of 19.8 minutes. Statistical analysis showed that these results were not statistically different from those of the unseeded system.

3.1.4 Particle Concentration Effect

The mass concentrations of aluminum oxide, silicon dioxide and calcium carbonate particle suspensions were varied from 0 to 1 g/L. The average supercooling and induction times for hydrate formation decreased with increasing aluminum oxide and calcium carbonate particle concentrations (Figure 3.4 and Figure 3.5). For aluminum oxide, the effect was not statistically significant at concentrations higher than about 0.2 g/L. For calcium carbonate particles, the slope changed sharply at 0.1 g/L and never quite became horizontal thereafter. To determine the minimum particle concentrations that would successfully seed hydrate formation, several low concentrations of calcium carbonate particle suspensions were used. Below about 0.05 g/L, necessary supercooling values were not significantly lowered. Variability was large and multiple t-test and analysis of variance showed that these low end values were not statistically different.

Again, silicon dioxide particles did not have any effect on supercooling at particle concentrations up to 1 g/L (Figure 3.6). An analysis of variance among all the results in Figure 3.6 showed these times were statistically equivalent.

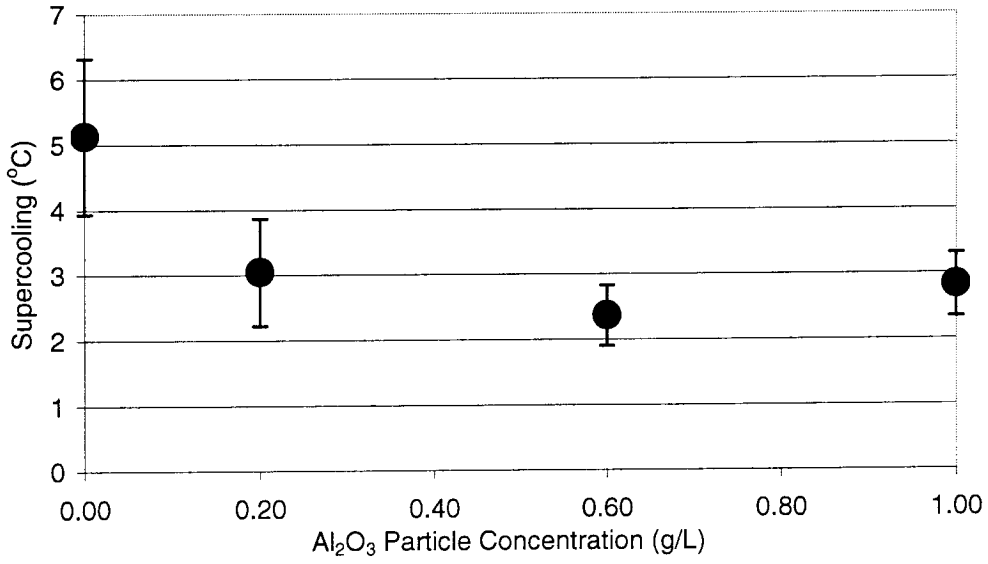

Figure 3.4: Variation of supercooling values for methane hydrate formation versus aluminum oxide mass concentration (n=5 for all sets, standard deviations shown).

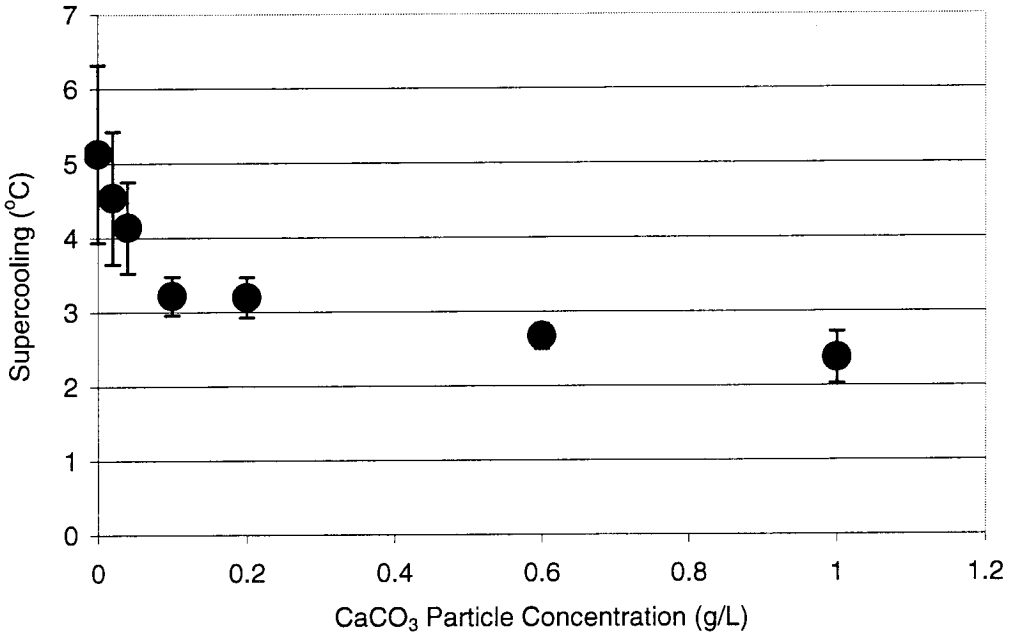

Figure 3.5: Variation of supercooling values for methane hydrate formation versus calcium carbonate mass concentration (n=5 for all data points, standard deviations shown).

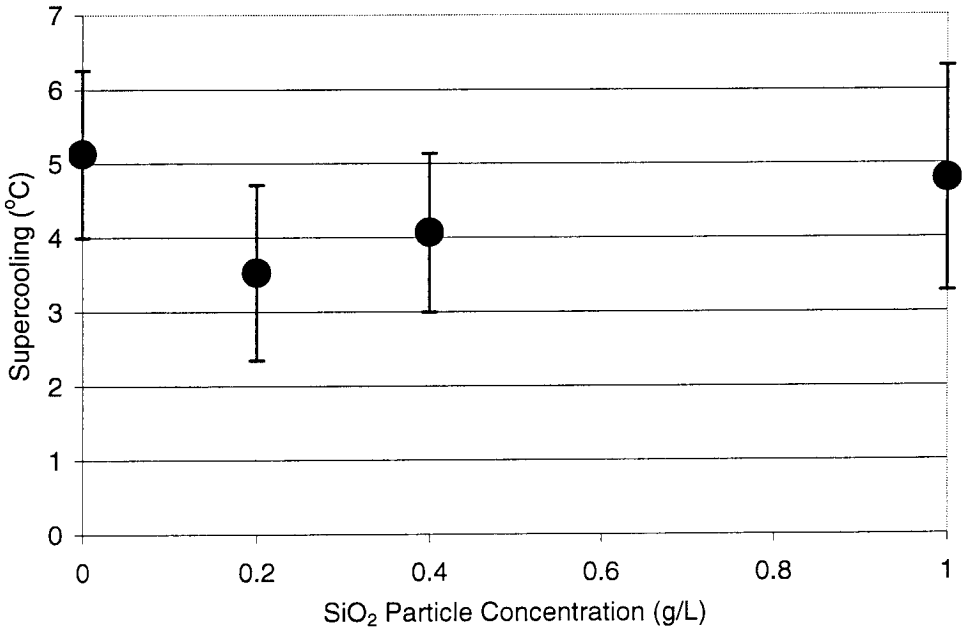

Figure 3.6: Variation of supercooling values for methane hydrate formation versus silicon dioxide mass concentration (n=5 for data points except n=10 for 1 g/L concentration).

3.1.5 Inhibitor Effect

A 1 g/L polyvinlypyrrolidone solution inhibited methane hydrate formation, increasing supercooling to 8.87 °C and induction time to 114.9 minutes, a gain of 72.9 and 65.8% respectively. Reproducibility was not improved though; standard deviation of sueprcooling was 1.77 °C. These values are higher but in the same range as that for the unseeded system.

3.1.6 Seawater Hydrate Formation Kinetics

Hydrate formed more slowly in artificial seawater than in pure water, even after taking into account the unfavorable shift in phase equilibria. Aluminum oxide particles still successfully enhanced hydrate formation from seawater (Figure 3.7).

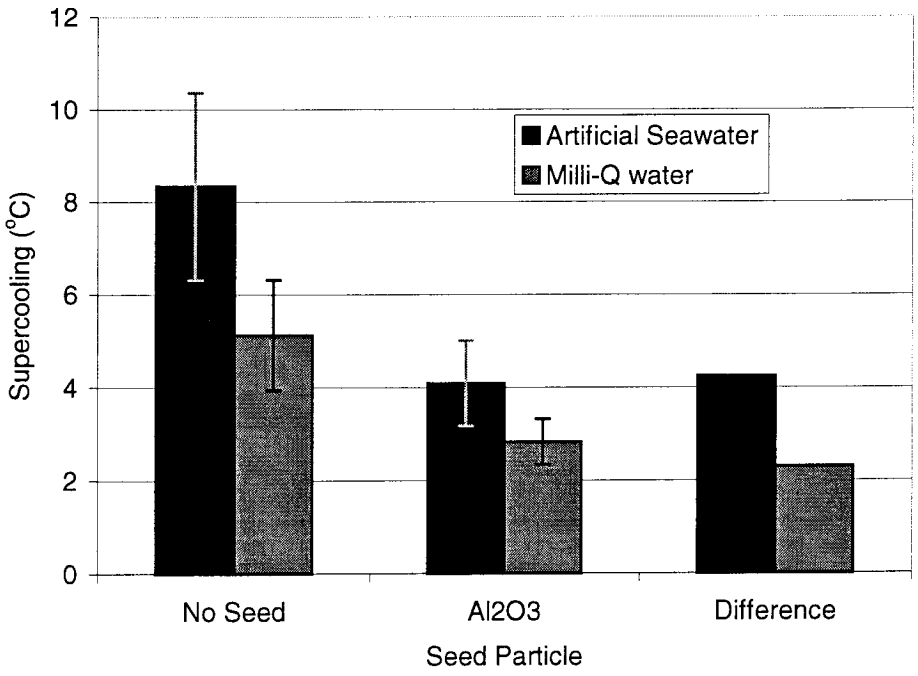

Figure 3.7: Comparison of methane hydrate formation in pure water and seawater systems with and without aluminum oxide seed (n=5 for all sets except no seed with n=26, standard deviations shown).

3.1.7 Temperature Increases

Hydrate formation was accompanied by temperature increases caused by the heat released during the exothermic hydrate formation reaction. Temperature increases were very small for methane hydrate formation because so little hydrate forms in each experiment. Heights of temperature spikes correlated with the supercooling needed for hydrate formation (Figure 3.22), increasing with increasing supercooling. This shows that more hydrate formed at higher supercooling (longer induction times). The temperature spike versus supercooling trend was the same for seeded and unseeded systems. The addition of PVP produced smaller temperature spikes at comparable supercooling values.

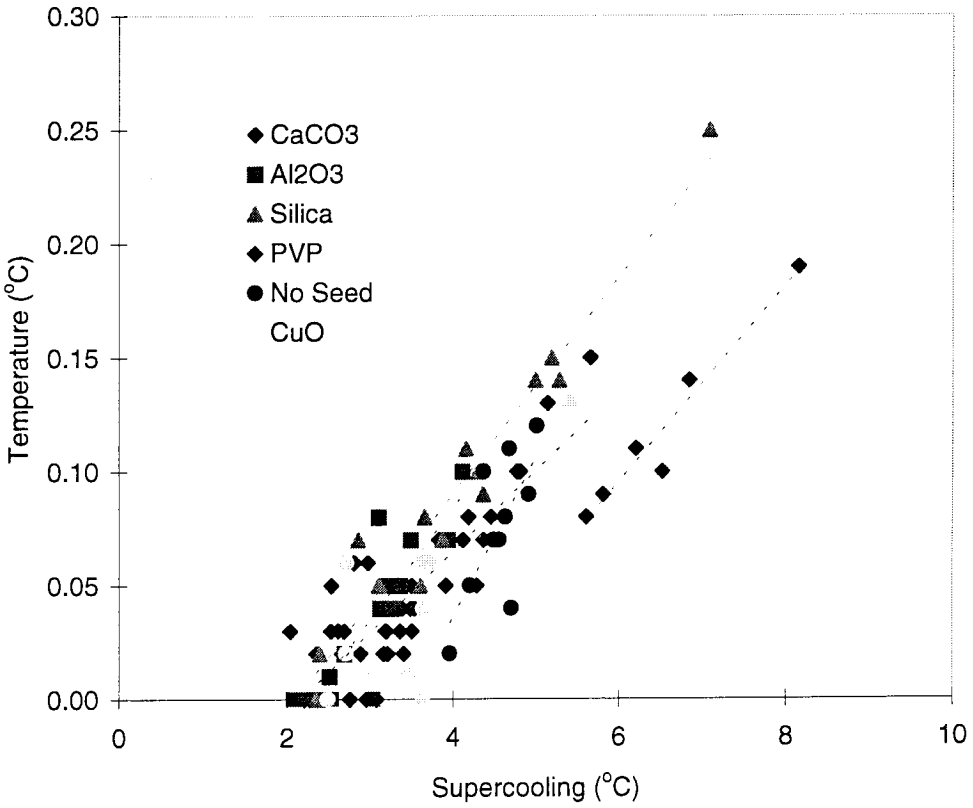

Figure 3.8: Temperature spikes during methane hydrate formation plotted versus supercooling.

3.2 Carbon Dioxide Hydrate

3.2.1 Qualitative Description

Carbon dioxide hydrate formed throughout the bulk solution spontaneously. The high mixing rate and liquid state of the carbon dioxide caused a turbulent condition with many carbon dioxide droplets. The bulk solution, including droplets, became whiteish and opaque. Occasionally, the stir bar continued rotating, signifying that the hydrate was not completely solid but more slurry-like. Frequently, especially at longer induction times, the stir bar stopped mixing when hydrate formed, indicating a more solid form of hydrate.

3.2.2 Control Experiments in Absence of Seed Particle

Hydrate was formed from liquid carbon dioxide and liquid Milli-q water in a series of ten experiments (Figure 3.9). The average supercooling was 9.38 °C with a standard deviation of 2.68 °C, corresponding to an induction time of 102.5 minutes and a standard deviation of 33.5 minutes. Again, the Kolmogorov-Smirnov test indicated a normal distribution (Figure 3.10) allowing use of parametric statistical analyses.

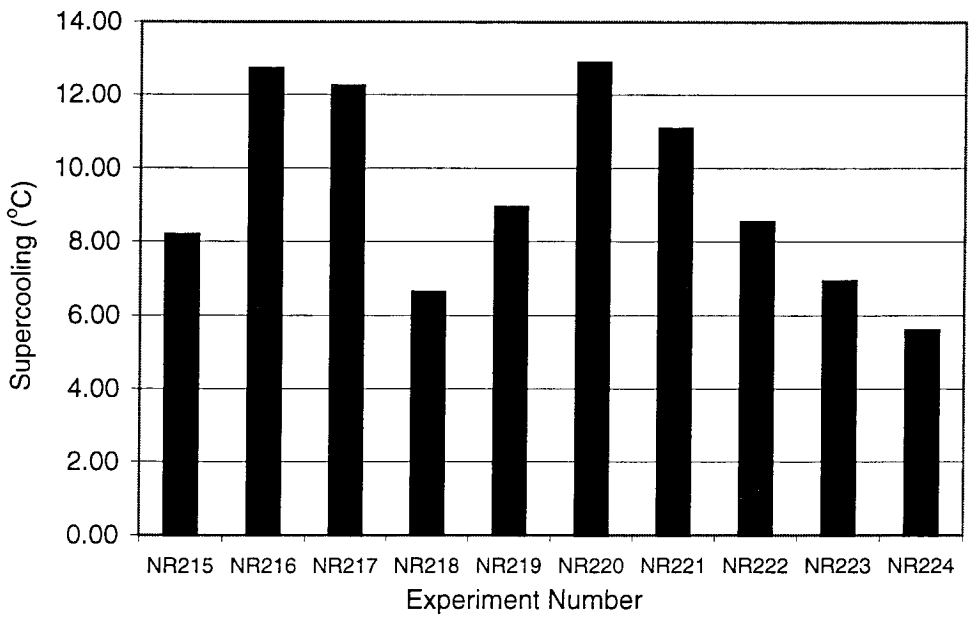

Figure 3.9: Supercooling values for carbon dioxide hydrate formation from carbon dioxide and pure water (n=10).

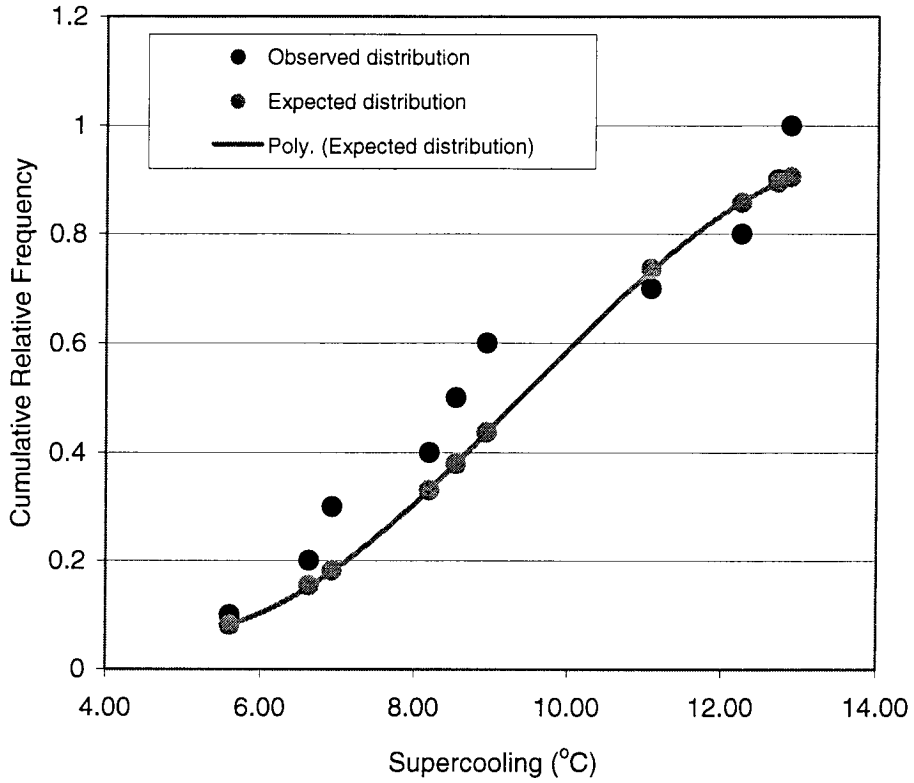

Figure 3.10: Cumulative frequency distribution of induction times for carbon dioxide hydrate from pure water and carbon dioxide, satisfies a normal distribution by the Kolmogorov-Smirnov test for normality.

3.2.3 Effect of Adding Aluminum Oxide Particles

In the first set of experiments, hydrate was formed from carbon dioxide and suspensions of Milli-q water and aluminum oxide of type Degussa C. The aluminum oxide used in these experiments was not pretreated by washing. Suspension concentration was varied from 0 to 1 g/L. The unwashed Degussa C aluminum oxide decreased supercooling values for hydrate formation by 51.1% to 4.59 ± 2.79 °C and by 57.4% to 4.00 ± 2.11 °C for 0.2 g/L and 1 g/L concentrations respectively (Figure 3.11). Induction times decreased to 50.6 ± 29.0 and 43.7 ± 23.3 minutes for 0.2 g/L and 1 g/L concentrations respectively (Figure 3.11).

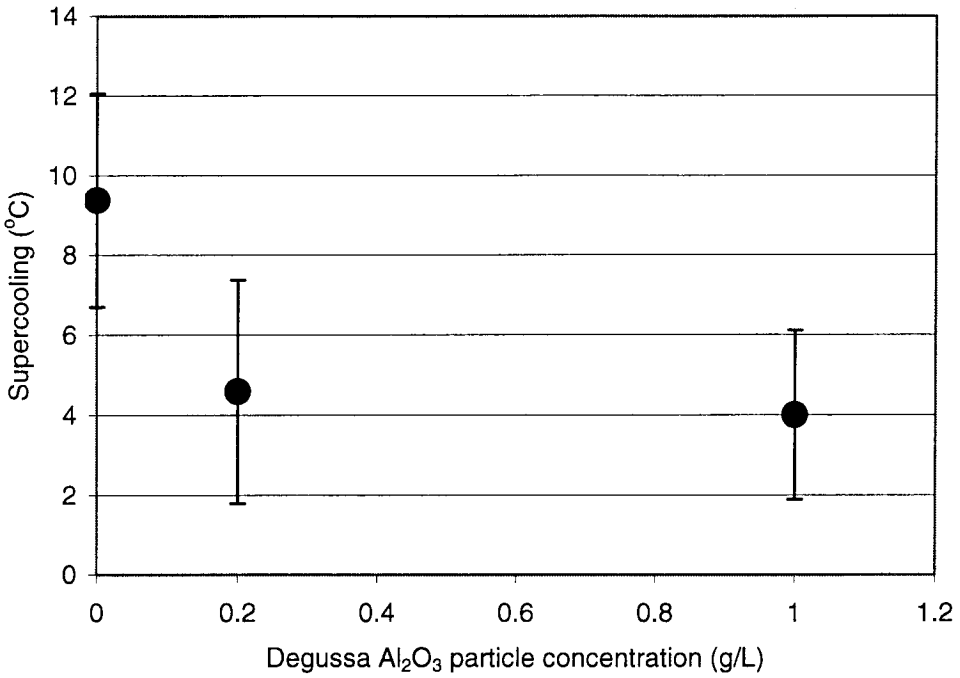

Figure 3.11: Variation of average supercooling for carbon dioxide hydrate formation versus unwashed Degussa C aluminum oxide mass concentration (n=10 for no seed, n=3 for 0.2 g/L and n=5 for 1 g/L concentration, standard deviations shown).

When the experiment was duplicated with 1 g/L concentration of washed Degussa C aluminum oxide, it was found that the washed aluminum oxide did not decrease supercooling nor did it have any other effect. This set of experiments with unwashed particles was repeated to ensure that the difference between washed and unwashed particle results was real. Results are shown in Figure 3.12. Washed and unwashed Linde D aluminum oxide particles were also compared at a suspension concentration of 1 g/L. Although the difference in supercooling is not significant, reproducibility was better with unwashed Linde D particles. It was decided to use unwashed particles in all subsequent experiments.

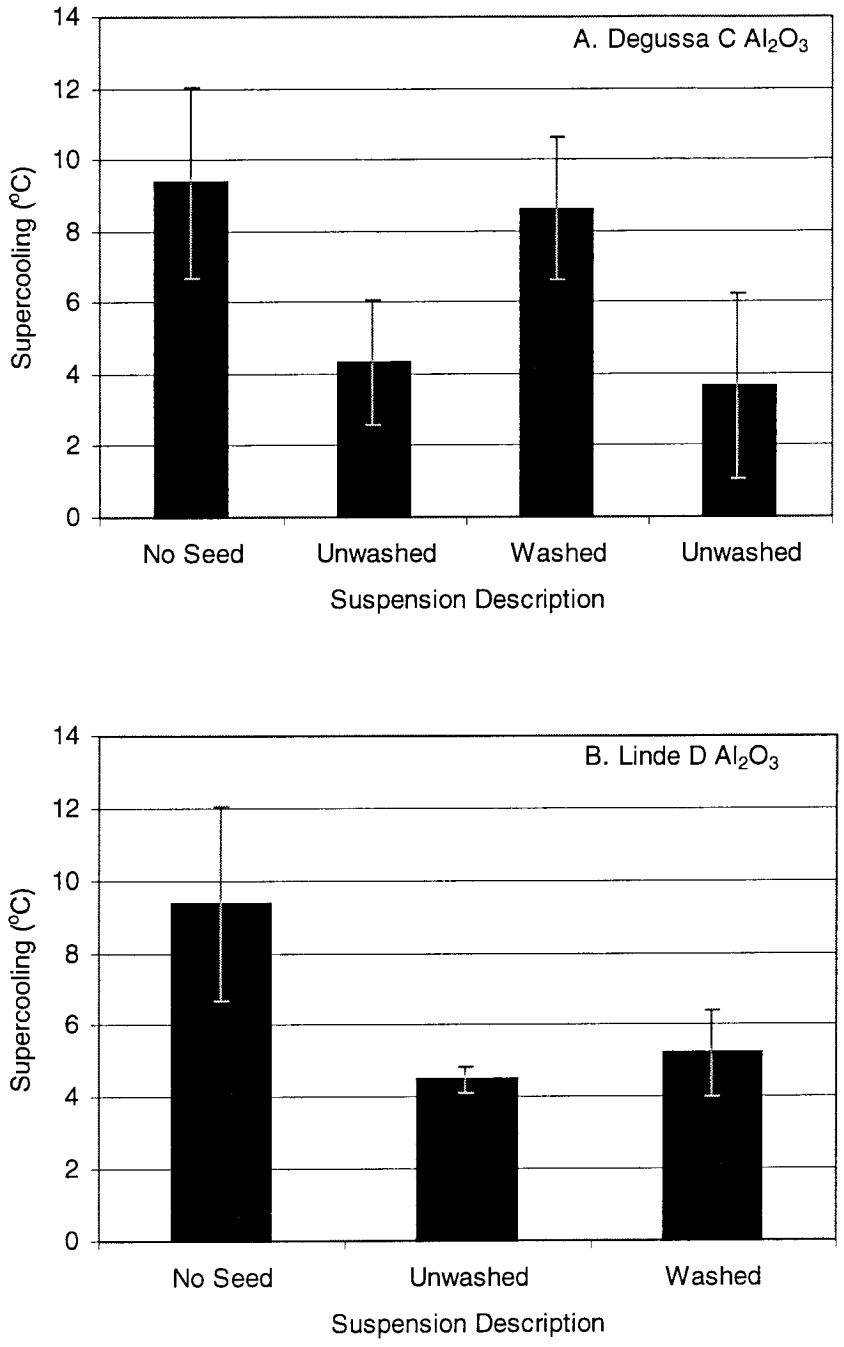

Figure 3.12: Effect of washing particles on supercooling values. All concentrations were 1 g/L. Top: Degussa C Al_2O_3 Bottom: Linde D Al_2O_3 (n=5 for all sets with particles, standard deviations shown).

3.2.4 Concentration Variation

The suspension concentration of Linde D aluminum oxide was varied from 0 to 10 g/L to determine the seed behavior at low and high concentrations. Linde D aluminum oxide decreased induction times at all concentrations down to 0.005 g/L (Figure 3.13).

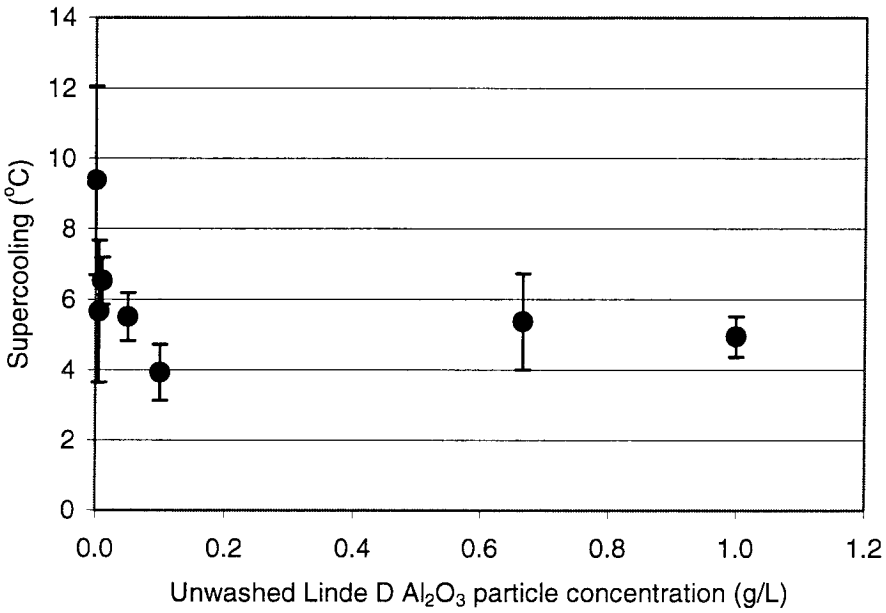

Figure 3.13: Variation of supercooling for carbon dioxide hydrate formation versus unwashed Linde D aluminum oxide mass concentration (n=10 for 0 g/L, n=4 for 0.005 g/L, n=5 for 0.01, 0.05 and 0.05 g/L, n=10 for 0.1, 0.667 and 1.0 g/L, standard deviations shown).

Increasing particle concentrations up to 10 g/L did not significantly decrease induction times over lower concentrations of 0.1 to 1.0 g/L (Figure 3.14).

Stock solutions of lower concentration suspensions of Linde D aluminum oxide were prepared and, after sonicating for one hour prior to experiment, 25 ml of suspension was transferred to the glass insert by pipette. Experimental runs using stock suspensions that had been aged for several days before experiment showed reduced effectiveness at decreasing induction times. Two series of experiments, shown in chronological order in Figure 3.15 exhibited this trend. For the 6th and 7th experiments at both concentrations

shown, new stock solutions were prepared and hydrate formed from these suspensions showed decreased induction times again.

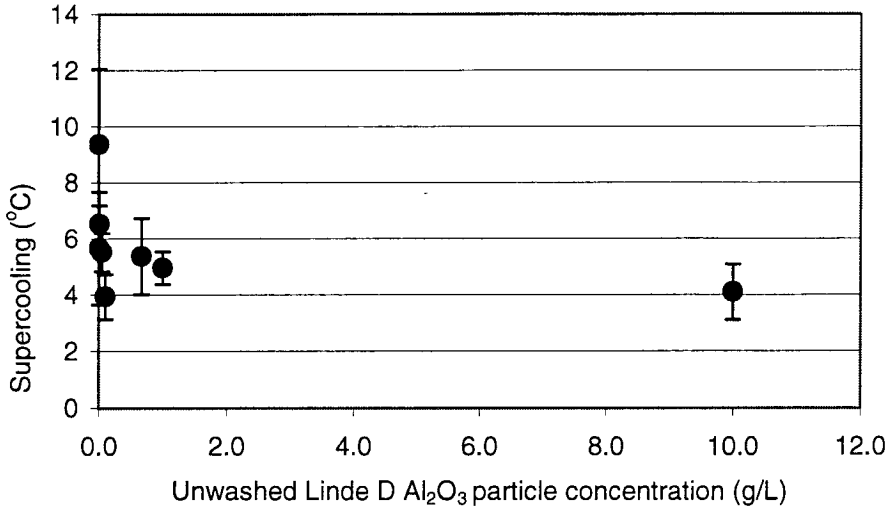

Figure 3.14: Variation in supercooling for carbon dioxide hydrate formation versus unwashed Linde D Aluminum Oxide mass concentrations up to 10 g/L (n=6 for 10 g/L, standard deviations shown).

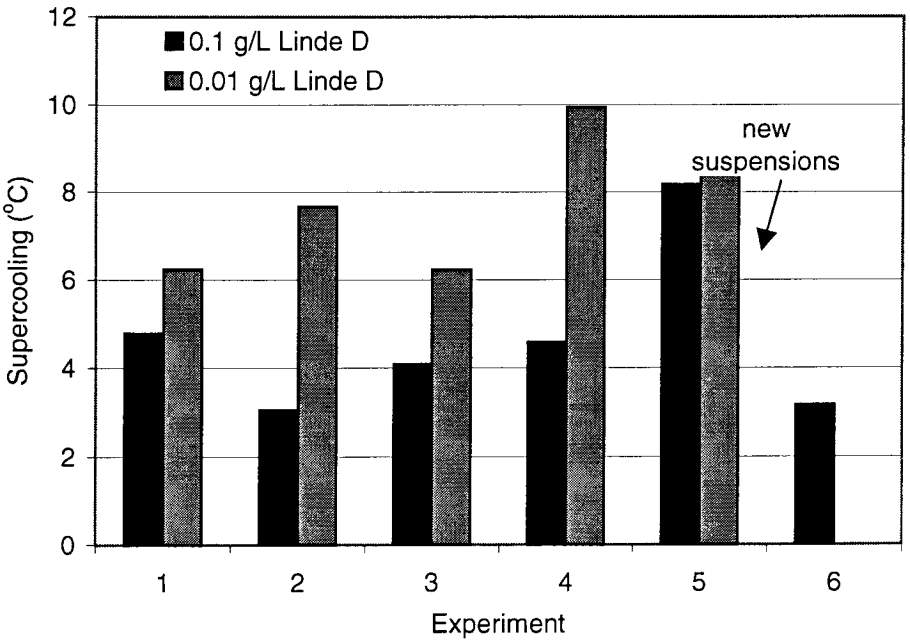

Figure 3.15: Two experimental runs of carbon dioxide hydrate formation supercooling values, presented chronologically, showing effect of aging on particle suspensions.

Supercooling values were next measured for carbon dioxide hydrate formation from suspensions of the remaining aluminum oxides, Linde A, C and Praxair B. Mass concentrations of particles equivalent to 10 m^2/L were used. Experiments were performed using reported surface areas, before BET measurements were made, so the surface area normalization is only approximate. None of Linde A, C and Praxair B had a significant effect on average supercooling (Figure 3.16). Variability remained large for Linde A and Praxair B.

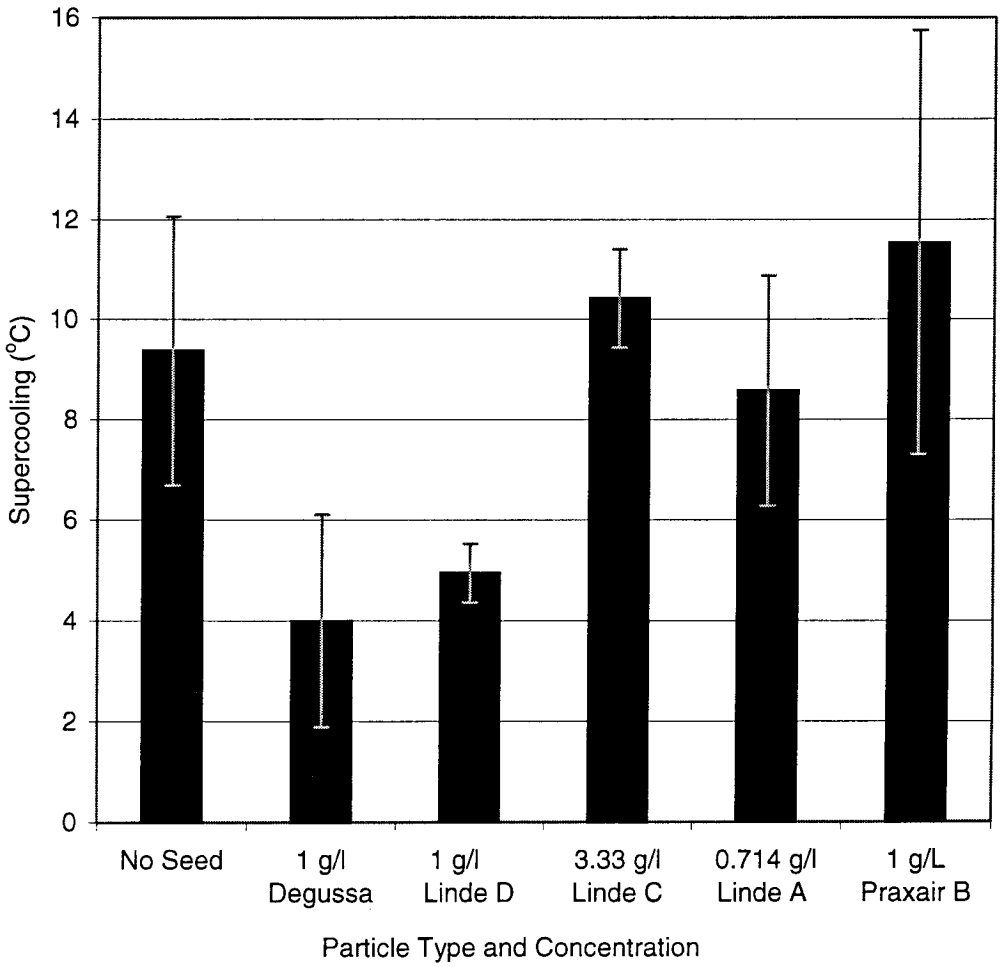

Figure 3.16: All experiments with aluminum oxide particles. Results with unwashed and aged particles are not presented. Particle mass concentrations correspond to surface area concentrations of approximately 10 m^2/L (n=10, 10, 5, 5, 5 and 5 in order presented, standard deviations shown).

Figure 3.17 and Figure 3.18 show supercooling values for all aluminum oxides versus mass concentration and surface area concentration.

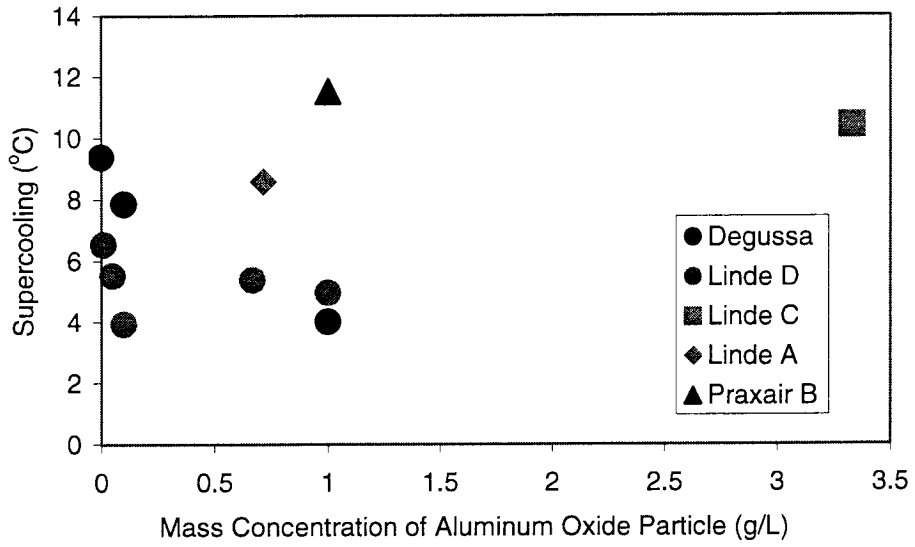

Figure 3.17: Supercooling needed for carbon dioxide hydrate formation plotted versus aluminum oxide particle mass concentration. Note that only Degussa and Linde D decreased supercooling.

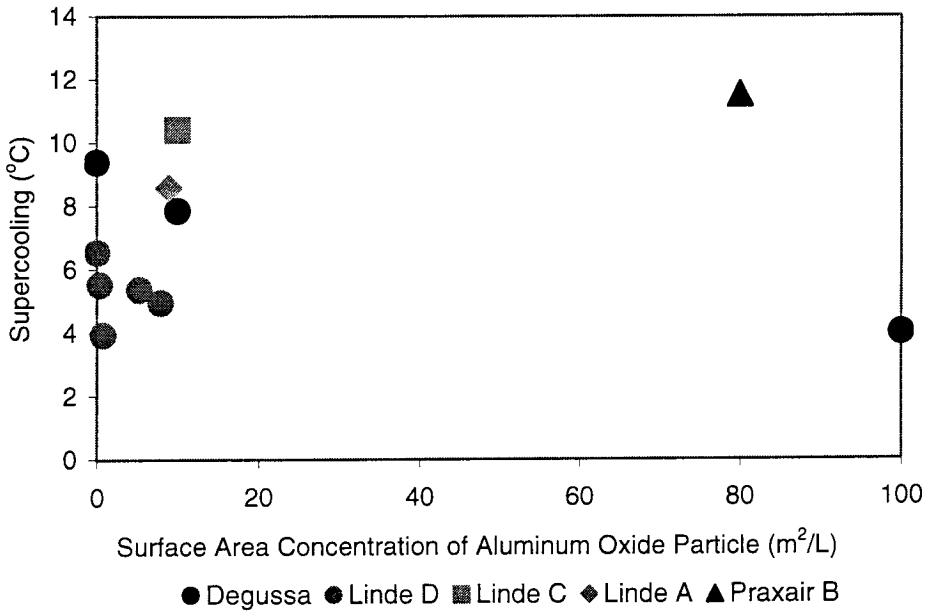

Figure 3.18: Supercooling needed for carbon dioxide hydrate formation plotted versus aluminum oxide particle surface area concentration.

3.2.5 Effect of Adding Other Oxide Particles

$Mg(OH)_2$, Fe_2O_3 and SiO_2 particles had no significant effect on hydrate formation with average supercooling values of 10.93 ± 2.26, 11.29 ± 3.42 and 10.01 ± 4.22 °C, respectively (Figure 3.19). CuO reduced the supercooling needed for formation of carbon dioxide hydrate to 1.33 ± 0.27 °C, a reduction of 86%.

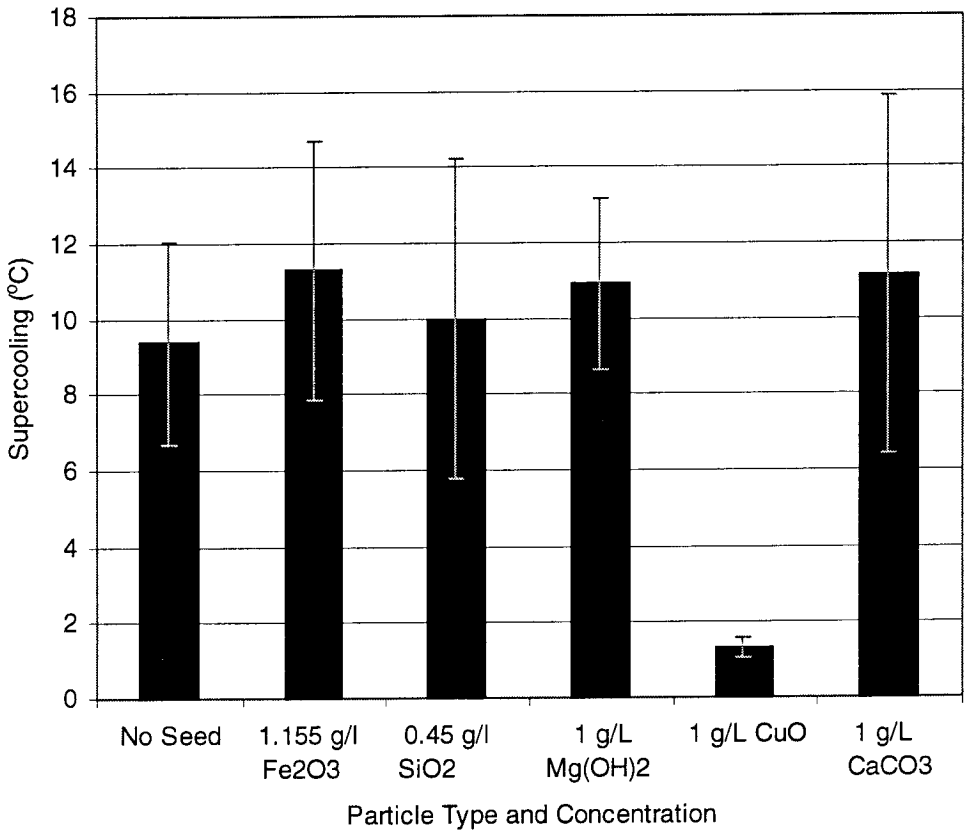

Figure 3.19: Average supercooling necessary for carbon dioxide hydrate formation from suspensions of oxides and $CaCO_3$ (n=10, 5, 5, 5, 5 and 3 in order presented, standard deviations shown).

3.2.6 Effect of Adding $CaCO_3$ Particles

The average supercooling necessary for carbon dioxide hydrate formation from a 1 g/L suspension of $CaCO_3$ particles was 11.17 ± 4.73 °C (Figure 3.19). The $CaCO_3$ particles

dissolved during the experiment, accounting for their lack of effect. Dissolution was visually determined by the clearness of suspension.

3.2.7 Phase Equilibria

To determine whether particles in the hydrate forming solution affected the phase equilibria, equilibrium pressures and temperatures were determined by measuring the hydrate decomposition pressures and temperatures. Decomposition temperatures were measured for pressures near the formation pressure of 5.5 MPa for hydrate formed from Milli-q water and from suspensions of oxide and carbonate particles, Table 3.1.

Table 3.1: Phase equilibrium data.

Suspensions	Decomposition Temperature (°C)	Pressure (MPa)
No Seed	10.17	5.496
No Seed	10.20	5.496
0.05 Linde D Al_2O_3	10.12	5.921
1 g/L Linde D Al_2O_3	10.16	6.061
10 g/L Linde D Al_2O_3	10.19	6.041
1 g/L Praxair B Al_2O_3	10.18	5.979
1 g/L Degussa C Al_2O_3	10.23	6.061
1 g/L $CaCO_3$	10.10	5.969
1 g/L $Mg(OH)_2$	10.06	5.925
1 g/L $Mg(OH)_2$	10.05	6.012

There was no large off-set from the phase line caused by the addition of particles (Figure 3.20). All the data points, including those with Milli-q water, only did indicate slightly higher decomposition temperatures, by about 0.2 °C, than the data culled from the literature. Precise calibration of temperature and pressure probes was verified. The cause of this small difference was not discovered.

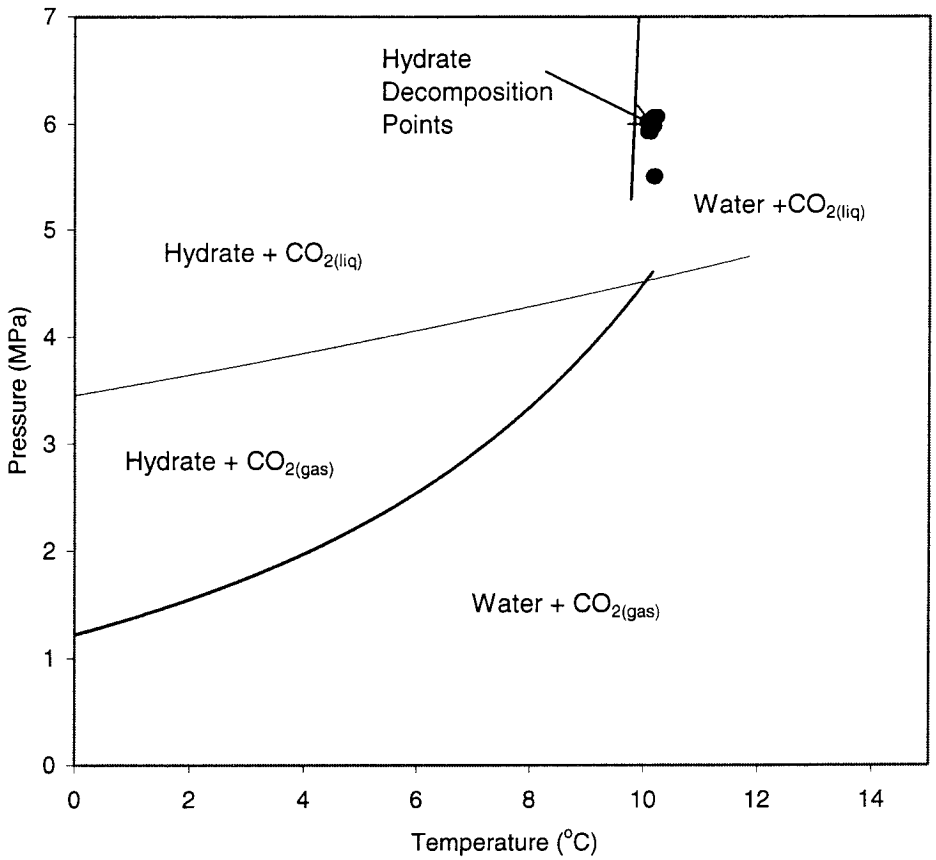

Figure 3.20: Phase equilibria for carbon dioxide hydrate formation. Regression lines are drawn through data gathered from literature [1]. Solid circles in upper left of diagram represent experimental decomposition data.

3.2.8 Particulate or Dissolved

The aluminum oxide phase, dissolved or particulate, that successfully catalyzed hydrate formation was investigated. The supercooling values necessary for hydrate formation from a suspension of Linde D aluminum oxide were measured in a series in of four replications. The particle suspensions from these experiments were saved, heated to room temperature and left for several days to ensure decomposition of all hydrate nuclei. They were then filtered through a 0.05 micron polycarbonate filter to remove most of the particles. Solutions were completely clear after filtration. Hydrate was formed from this filtrate in a series of only three replications because some of the solution was lost during

the recovery process. Average supercooling induction time for hydrate formation from this set of experiments with Linde D aluminum oxide was 5.43 ± 0.97 °C. Hydrate formed from the filtrate with a supercooling of 10.18 ± 2.66 °C, not different from the unseeded control system supercooling of 9.38 ± 2.68 °C.

3.2.9 Seawater Hydrate Kinetics

Hydrate was formed from carbon dioxide and synthetic seawater. Two experiments of 5 replications were conducted for systems with no added particles and with 1 g/L Linde D aluminum oxide particles. Supercooling was higher for hydrate formation from seawater than from pure water and the aluminum oxide particles decreased supercooling in seawater systems, as in pure water systems. Average supercooling values were 13.65 ± 1.75 °C in the unseeded system and 7.51 ± 0.71 °C in the seeded system.

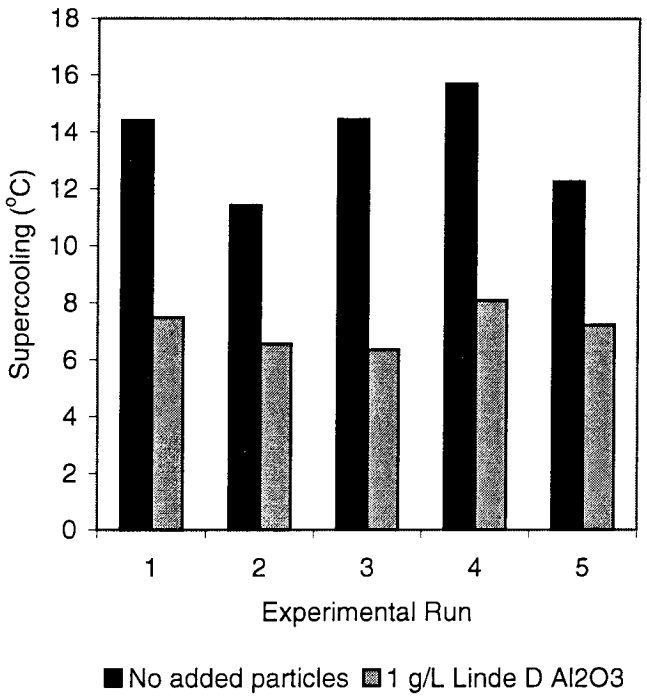

Figure 3.21: Supercooling values for carbon dioxide hydrate formation from seawater. Individual experiment results are shown from two series of 5 replications.

3.2.10 Temperature Increases

Hydrate formation was accompanied by temperature increases caused by the heat released during the exothermic hydrate formation reaction. Because much more hydrate is formed in the experiments with carbon dioxide than with methane, temperature spikes are larger for carbon dioxide hydrate formation. Heights of temperature spikes correlated with supercooling necessary for hydrate formation (Figure 3.22). More hydrate formed at higher supercooling values. The temperature spike versus supercooling trend was the same for seeded and unseeded systems with carbon dioxide. Three experiments at a lower stir rate, 300 rpm compared to the usual 450 rpm, showed slightly lower temperature spikes.

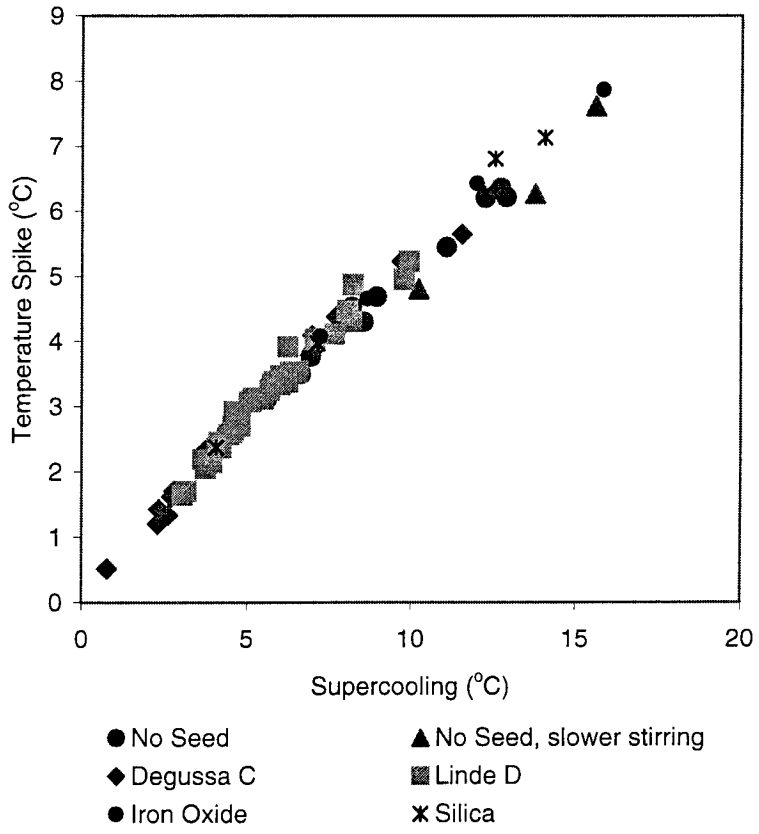

Figure 3.22: Correlation between temperature spike during hydrate reaction and supercooling for carbon dioxide hydrate formation.

3.3 Electrophoretic Mobilities and pH_{pzc}

Electrophoretic mobilities of Linde A, C and D aluminum oxide at 25 °C are compared in Figure 3.23. When particles have a net zero surface charge, mobility of the particle tends to zero. The pH at which particles are neutral is called the Point of Zero Charge. The pH_{pzc} is measured by varying the pH and observing when the mobility vs charge curves cross the zero mobility axis. The pH_{pzc} of Linde A, C and D at 25 °C were found to be approximately 7.5, 5.2 and 6.9 respectively.

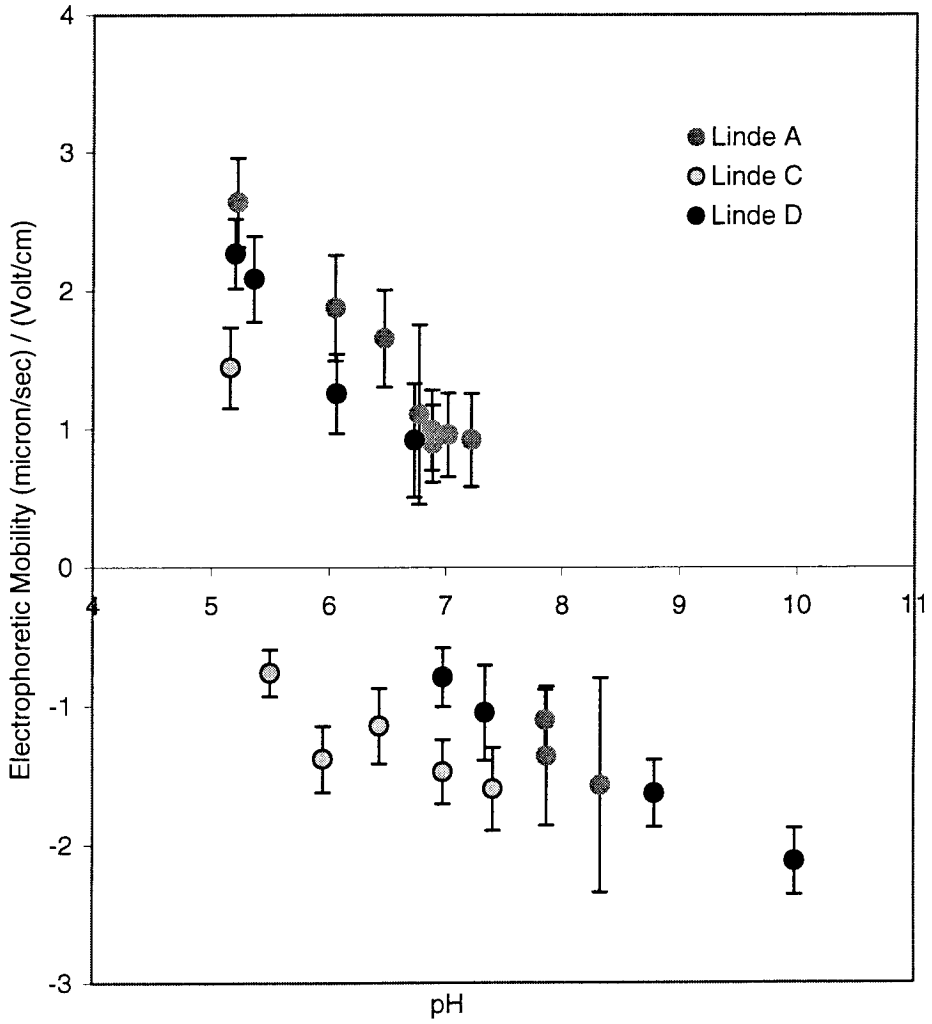

Figure 3.23: Linde A, C and D particle electrophoretic mobilities versus pH at 25 °C (error bars are standard deviations).

The pH_{pzc} of oxides varies with temperature [2, 3]. The pH_{pzc}'s of a magnetite and an unspecified aluminum oxide were found to decrease with increasing temperature from 6.9 at 10 °C to 5.4 at 100 °C and from 9.5 at 10 °C to about 8 at 100 °C, respectively [3]. In contrast, the pHpzc of γ-Al_2O_3 was found to increase with increasing temperature, from 4.5 at 10 °C to 9 at 50 °C [2]. No studies were found of the temperature dependence of pH_{pzc} at temperatures lower than 10 °C, where hydrate formation is possible. Particle mobilities were remeasured at 5.5 °C (Figure 3.24), the temperature at which hydrates form from Linde Al_2O_3 seeded water. A constant temperature of 5.5 °C in both solution and electrophoresis cell was maintained with water baths. Measured pH_{pzc} was greater than 8, between 6 and 7.5, 8.5 and 11.2 for Linde A, C and D aluminum oxides and $Mg(OH)_2$, respectively. Stabilization of suspension pH was difficult, accounting for lack of adequate data for accurate determination of pH_{pzc} in some cases. CuO particles settled and stuck to the walls of the electrophoresis cell making measurements very difficult.

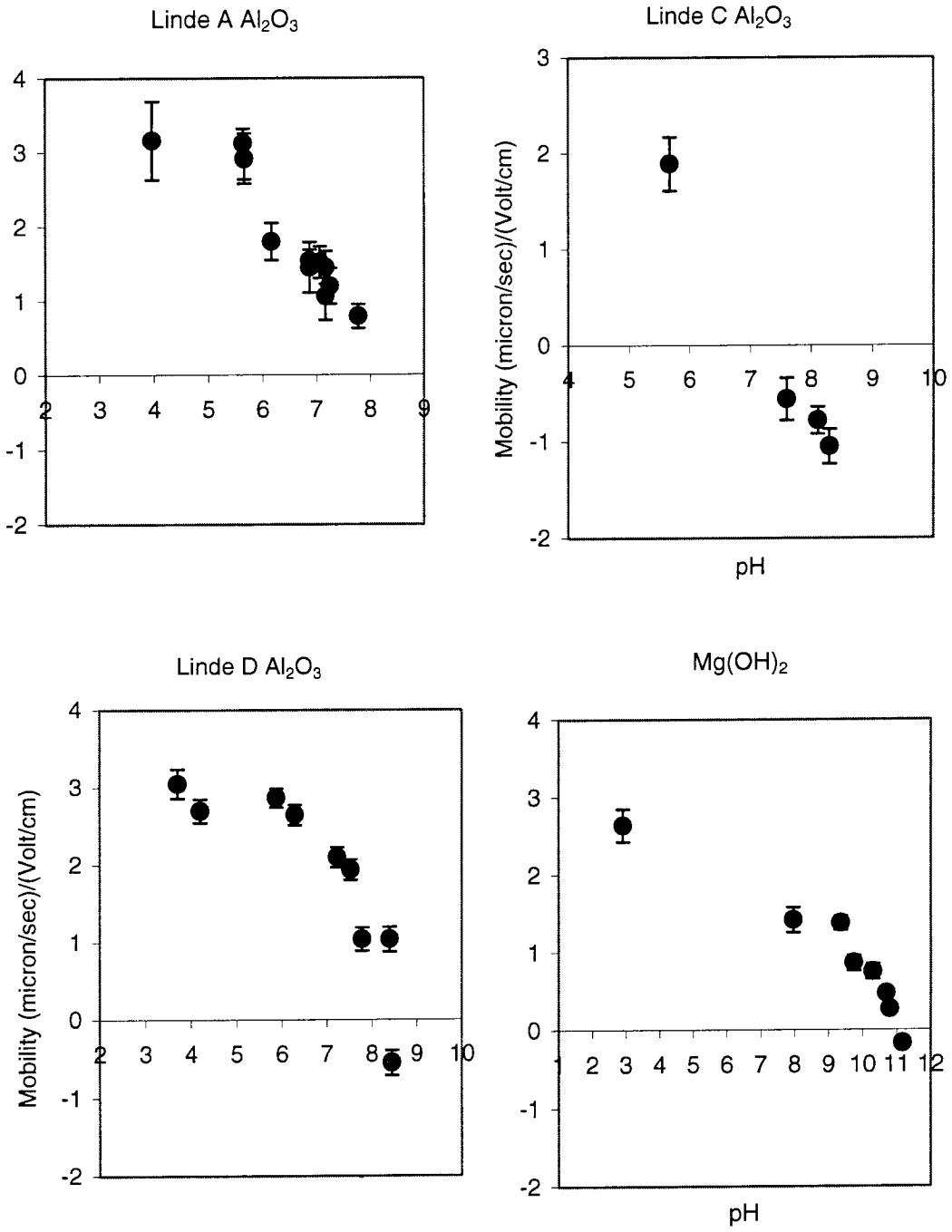

Figure 3.24: Electrophoretic Mobilities of Linde A, C, D and $Mg(OH)_2$ at 5.5 °C.

3.4 References

1. E. D. J. Sloan, *Clathrate Hydrates of Natural Gases*. H. Heineman, Ed., Chemical Industries (Marcel Dekker, Inc., New York, 1990), vol. 39.

2. K. C. Akratopulu, L. Vordoni, A. Lycourghiotis, *J. Chem. Soc., Faraday Trans. 1* **82**, 3697-3708 (1986).

3. P. H. Tewari, A. W. McLean, *Journal of Colloid and Interface Science* **49**, 267-272 (1972).

Chapter 4 Discussion of Results

4.1 Homogeneous Systems

4.1.1 Methane

In the particle-free homogeneous aqueous solutions, methane hydrate only formed at the interface between the free methane gas phase and the dissolved methane and water bulk aqueous phase. A transparent, solid membrane formed, separating methane gas and water. Even after several days of stirring and allowing for continued methane dissolution, hydrate never formed in the bulk solution.

Methane hydrate only forms at the interface because only at the interface are there enough methane molecules to support nucleation. Methane hydrate forms when methane molecules dissolve in water and stabilize the partial cages or ring structures of water molecules that exist in water. Dissolved methane molecules are needed to stabilize the water cages. In the absence of sufficient gas molecules, the cages destabilize and decompose before the cage structures reach critical nuclei size. Because the solubility of methane in water is low, the concentration of dissolved methane in the bulk aqueous phase is too low to support hydrate nucleation. At the interface, though, water molecules arrange themselves around the abundant methane molecules in the methane gas phase. After hydrate formation occurs at the interface, the solid hydrate membrane inhibits continued hydrate growth into the bulk solution. Diffusion of methane gas across the film is slow and the concentration of dissolved methane gas never increases enough for hydrate formation.

North et al. [1] have also demonstrated the existence of a hydrate film at the interface between water and carbon dioxide. Others [2, 3] agree that the membrane greatly inhibits, though does not completely stop, further transfer of gas into the liquid phase. Vysniauskas and Bishnoi [4] observed in their methane hydrate formation experiments that a few crystals of hydrate appeared on the water surface, after which they

recommenced stirring to measure bulk hydrate growth rates. They agreed that methane hydrate formation is an interfacial phenomenon, occurring at the interface because of the low solubility of methane in the liquid water. "Hence the most likely place where the concentration of water and methane molecules could be high enough to initiate and sustain hydrate formation is at the gas-water interface" [4]. In the same laboratory, Englezos et al. [5] reported that, when a uniform supersaturation was reached before the appearance of nuclei, the nucleation process occurred everywhere in the liquid water. Finding that hydrates of ethane and methane formed in the bulk solution, they suggested that the hydrate nuclei grow to critical size due to encapsulation of gas molecules at the crystal-water interface within the volume of solution. But the mixing rates used in these experiments were sufficiently high to break up any surface film and mix it into the bulk, producing what may have appeared to be nucleation in the bulk solution [6].

Average induction time for hydrate formation from pure water was 73.1 minutes and from seawater was 105.8 minutes. A longer induction time was needed to form methane hydrate from seawater than from pure water. The variability in measured induction times was large. The presence of small, unknown impurities cannot be ruled out as the cause of this variation.

4.1.2 Carbon Dioxide

In contrast to methane hydrate formation, carbon dioxide hydrate formed throughout the bulk solution. The entire aqueous phase solidified, though often the composition was more slurry-like at first and only became truly solid after several minutes to hours. Carbon dioxide hydrate forms in the bulk solution while methane hydrate does not because the solubility of carbon dioxide is higher than that of methane. The higher solubility ensures that there are enough carbon dioxide molecules in the bulk solution to stabilize the water cages.

The vigorous mixing of the solution produced droplets of liquid carbon dioxide throughout the bulk phase. Whether hydrate formed truly in the bulk solution first, or

formed at the surface of these droplets, was unclear. Earlier experiments, at lower mixing rates where droplets did not form, showed that carbon dioxide hydrate did form in the bulk solution but usually at the vessel surfaces. Although the initial nucleation site is unknown, hydrate spontaneously formed throughout the solution immediately after initiation because the concentration of carbon dioxide molecules was high enough.

Average induction time for carbon dioxide hydrate formation from pure water was 102.5 minutes and from seawater was 154.3 minutes. As in the methane system, a longer induction time was needed to form carbon dioxide hydrate from seawater than from pure water.

The variability in measured induction times was large and similar to that of the methane system. Again, formation of hydrate is probably not truly homogeneous because of unavoidable impurities in the solution.

4.2 Heterogeneous Systems

4.2.1 Methane

Adding certain types of particles to the hydrate forming solution shortened induction times for methane hydrate formation. Calcium carbonate and aluminum oxide particles shortened induction times and decreased variability equally well, while silicon dioxide particles had no effect on methane hydrate formation.

Hydrate nucleation occurs earlier in the presence of particles because of increased hydrogen bonding between surface hydroxyl groups on the particles and water molecules. The increased hydrogen bonding produces a structured layer of water molecules at the surface of the particle. This structure is stabilized by dissolved methane molecules, around which the structure grows into complete clathrate cages.

This explanation is substantiated by the findings of others that ordered, structured vicinal water exists at surfaces [7, 8].

Parallels between ice nucleation and hydrate nucleation are clear. Some solid particles and inorganic materials are good nucleators of ice. A matching, or fit, between

ice and nucleator crystal structure results in a correspondence between hydrogen bonding groups at the particle surface, the hydroxyl groups, and hydrogen bonding groups at the ice surface. If the unit cell structure and dimensions match well, hydrogen bonding is encouraged and an ice-like structure at the particle surface forms. When water molecules are adsorbed on the nuclei, the free energy of the system is lowered, and the forming ice embryo requires a lower free energy because the atoms of the nucleating surface have the same arrangement as ice crystals. As discussed in the next section, there is a remarkable coincidence of particles that nucleate ice and those that nucleate hydrate. Hydrate nucleation on particles may be caused by either a thin layer of ice forming on the particles first, and acting as a template for subsequent hydrate nucleation, or by the direct formation of hydrate crystals on the particles. There is a fair match of the oxygens of the 110 face of structure I hydrate, the exposed face [9], with those of ice, showing that hydrate formation on an ice surface may be favorable. The matching of crystal faces of nucleating particles and hydrate has been attempted and the possibility of forming clathrate-like structures directly on the particles and avoiding the middle ice-like layer should not be disregarded (see section 4.3.1).

Methane hydrate still formed only at the interface between methane gas and water, even in the presence of particles. The low concentration of methane molecules in the bulk solution and the presence of abundant methane molecules at the surface can again explain this phenomenon. In the experiments, the calcium carbonate, aluminum oxide and silicon dioxide particles appeared uniformly distributed throughout the water column. Therefore, particles would have been present at the interface. Particles that tended to settle out or avoid the surface would presumably not affect methane hydrate formation.

The hydrate reaction is exothermic, with the heat produced and associated temperature rise varying with the amount of hydrate formed. Though hydrate growth rates subsequent to initial formation were not measured, the temperature spikes provided an indirect measure of how much hydrate was formed initially. The quantity of hydrate

formed varied with induction time. Particles did not increase the quantity of hydrate formed while PVP, the known inhibitor, did lower the temperature spikes. PVP inhibits hydrate formation by interfering with hydrogen bonds and adsorbing to the clathrate surface, slowing further growth [10]. Particles, on the other hand, did not affect how much hydrate was formed, but only hastened the formation of the critically sized hydrate nuclei. This finding is substantiated by that of Bylov and Rasmussen [11], who added particulate impurities to their system studying ethane hydrate formation. The particles significantly decreased induction times over particle-free systems but the measured hydrate growth rates were comparable in both systems. Vysniauskas and Bishnoi [4] measured hydrate growth rates after seeding with dissociated methane hydrate and also found no difference between growth rates using double distilled water and dissociated hydrate samples.

4.2.2 Carbon Dioxide

Particles catalyzed the formation of carbon dioxide hydrate as well. Of the particles tested, copper (II) oxide was by far the most effective, reducing the average induction time by 85% from 102.5 minutes to 15.4 minutes. Copper particles also nearly eliminated the variability of hydrate formation time, reducing the standard deviation from 33.5 minutes to 2.8 minutes. A variety of aluminum oxide particles were tested; some reduced induction times and others did not. Silicon dioxide, iron oxide and calcium carbonate particles had no effect on hydrate formation, within the variability of the results. Calcium carbonate particles dissolved in the acidic solution, thus accounting for their effectiveness in the methane system but not in the carbon dioxide system. The reasons why some particles are effective and others are not are discussed in the next section.

The same processes as occur in the methane system can explain the nucleation of hydrate in the heterogeneous carbon dioxide system. The main difference is that now all the particles are effective, and not just those at the interface.

4.3 Nucleation Catalysts

By comparing particle properties, this section explains why certain particles, among them calcium carbonate, copper oxide and some aluminum oxides, catalyze hydrate formation, while others, such as iron oxide, magnesium hydroxide and some other aluminum oxides, do not.

4.3.1 Comparison of Particle Properties

Crystal Structure

The most important property of a good nucleator of hydrate appears to be the crystal structure type and lattice dimensions.

Of the particles tested, those that have been shown to be good catalysts of ice nucleation and/or those that have matching crystal structures to ice, were also effective at seeding hydrate formation (Table 4.1). Copper (II) oxide, the most active particle tested for catalysis of hydrate formation, is also one of the best ice nucleators [12]. γ-Al_2O_3, the form of Degussa C aluminum oxide, was an efficient hydrate nucleator and has been proven as an effective ice nucleator [12]. Active particles, α-Al_2O_3 and calcium carbonate, though untested as ice nucleators, have crystal lattice parameter deviations from ice of only 5% and about 10%, respectively. The crystal form of calcium carbonate used, aragonite or calcite, was unknown but both have similar lattice parameters to ice. Although Garten and Head [13] set an upper limit of lattice mismatch of 7%, these lattice matches are deemed acceptable. Magnesium hydroxide, on the other hand, has a large crystal mismatch of 30.6% and Fe_2O_3 has a crystal mismatch of 11%. These two particles were not succesful catalyzers of hydrate formation. (They have not been tested as ice nucleators.) Silica particles were amorphous and therefore did not have crystal structures to match with that of ice. Examples of crystal match or mismatch between particle and ice presented in Figure 4.1. As shown, the crystal faces of α-Al2O3 and ice match well but those of $Mg(OH)_2$ and Fe_2O_3 do not match well with the crystal face of ice.

Table 4.1: Crystal structure and lattice parameters of ice and particles used in experiments.

Particle	Crystal Phase	Crystal System	Lattice Parameters a	b	c
Ice[12]		Hexagonal	4.51		
Synthesized Fe_2O_3[14]	100% α	Hexagonal	5.04		13.76
Degussa C Al_2O_3	**100% γ**	**Cubic**	**7.73-8.06**		
Linde A Al_2O_3[14]	90% α, 10% γ	Hexagonal	4.76		12.98
Linde C Al_2O_3[14]	100% α	Hexagonal	4.76		12.98
Linde D Al_2O_3[14]	**90% α, 10% γ**	**Hexagonal**	**4.76**		**12.98**
Praxair B-AF Al_2O_3[12]	10% α, 90% γ	Cubic	7.73-8.06		
Degussa SiO_2	amorphous	None			
$CaCO_3$: calcite[14]	**--**	**Hexagonal**	**4.99**		**17.06**
		Rhombohedral	6.37		
Aragonite[14]		**Orthogonal**	**4.95**	**7.96**	**5.73**
$Mg(OH)_2$[14]	--	Hexagonal	3.13		4.74
CuO [15]	**--**	**Monoclinic**	**4.65**	**3.41**	**5.11**

Shaded entries are particles that have been tested for and proven to be good ice nucleators [12]. Bolded entries are particles that been proven in this laboratory to be good catalysts of hydrate formation.

The crystal lattice similarity between ice and particles poses the question of whether the hydrogen-bonded water structuring occurring at the surface of the particle is "ice-like" or "hydrate-like." A thin layer of ice may form on the particle surface and then, in turn, initiate hydrate nucleation or the water structure could be in the form of clathrate cages directly. The crystal matching between the 110 face of hydrate and ice, α-Al_2O_3, and $Mg(OH)_2$ shows that both ice and α-Al_2O_3 do show some coincidence with hydrate but $Mg(OH)_2$ does not. The match is not great though, so it is unclear whether the match is good enough for "hydrate-like" structures to form directly on particles.

Clearly, crystal structure is not the only property of a particle that makes it a good catalyst of hydrate formation, since only some of the aluminum oxides were active while others had no effect at all.

a: ice

b: α-Al_2O_3 and ice

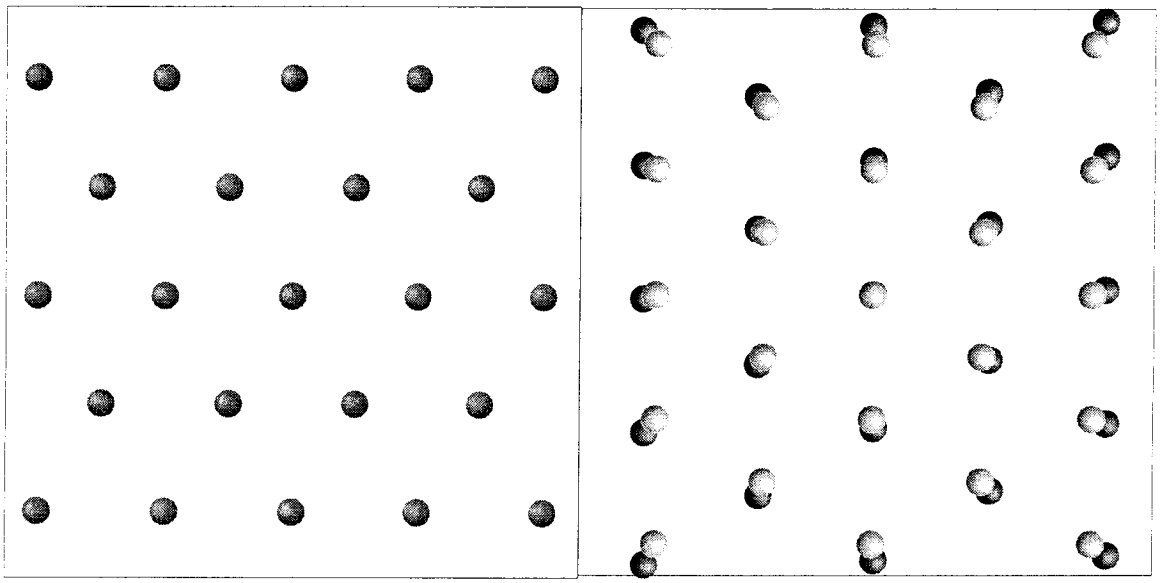

c: $Mg(OH)_2$ and Ice

d: Fe_2O_3 and ice

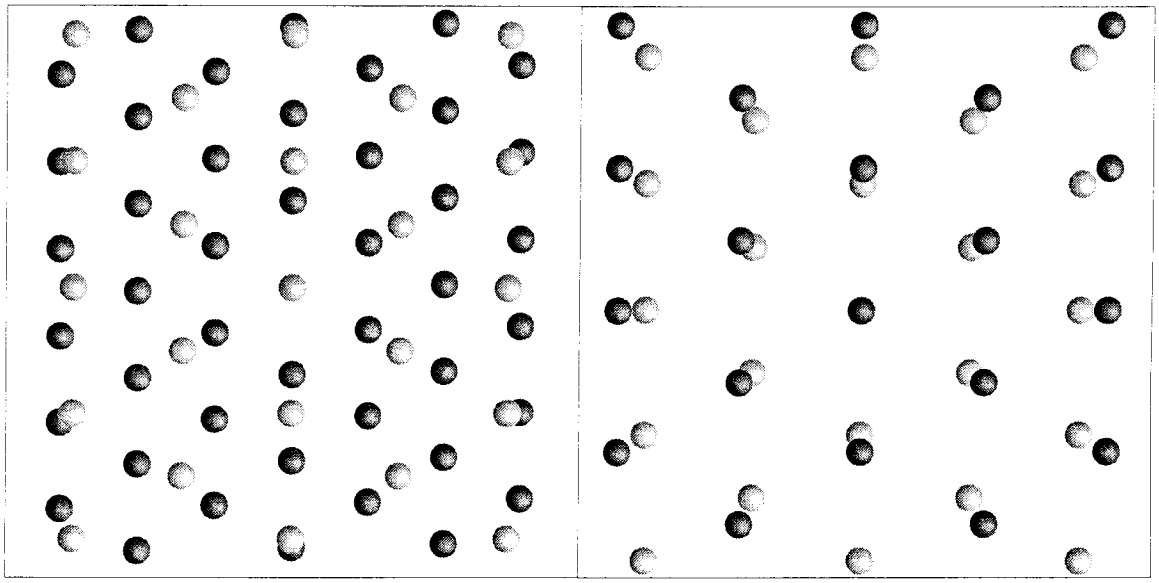

Figure 4.1: Crystal faces of ice and particles. Oxygen atoms are shown. Lighter spheres: ice oxygen atoms, darker spheres: particle oxygen atoms.

a: hydrate

b: hydrate and ice

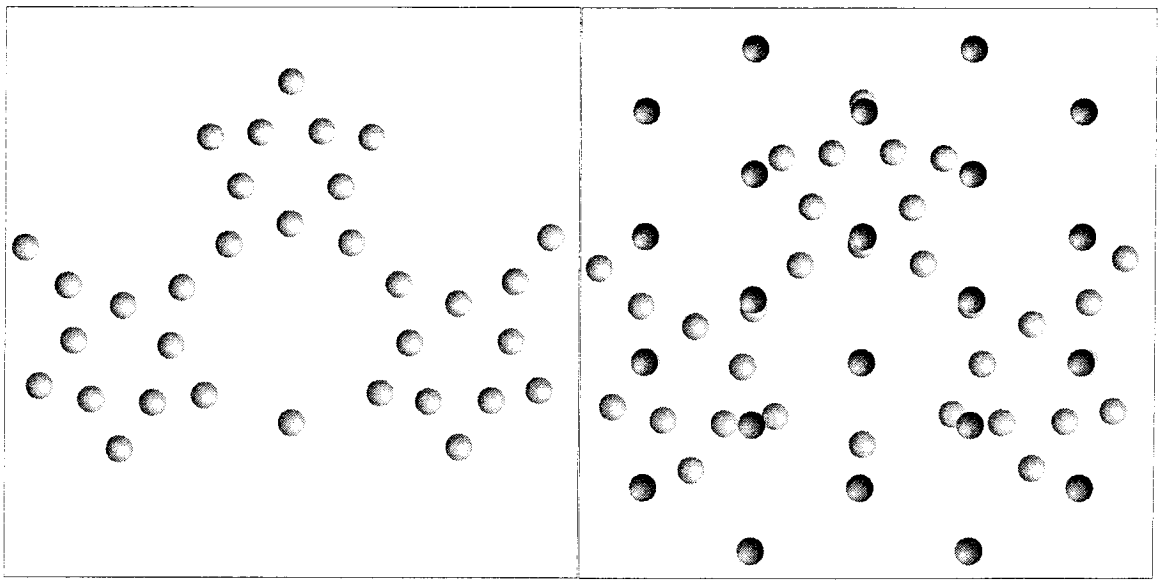

c: hydrate and α-Al_2O_3

d: hydrate and $Mg(OH)_2$

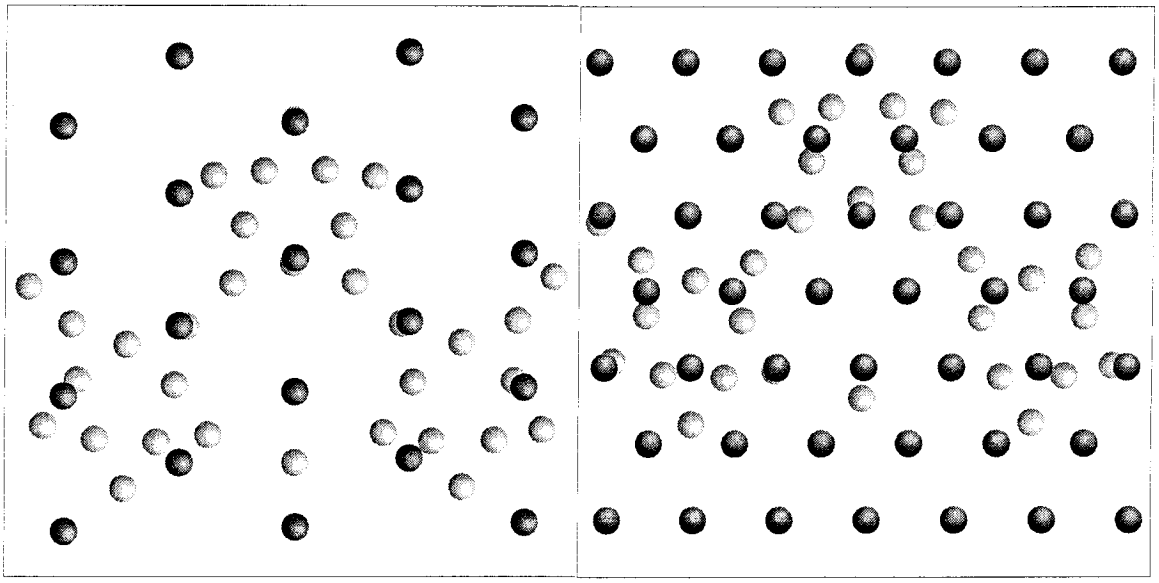

Figure 4.2: Crystal faces of hydrate and ice and particles. Oxygen atoms are shown. Lighter spheres: hydrate oxygen atoms, darker spheres: particle (and ice) oxygen atoms.

Size

Comparing sizes of the particles that decreased induction times, Degussa A and Linde D aluminum oxides, copper oxide and calcium carbonate, with those that did not decrease induction times, Linde A, C and Praxair B aluminum oxides, iron oxide and magnesium hydroxide, reveals no obvious dependency on particle size (Table 4.2). Measured size of active Linde D aluminum oxide particles was the same as that of inactive Linde A and C aluminum oxide, approximately 300 nm. Degussa C aluminum oxide particles were much smaller, 11.5 nm, but still quite active in reducing induction times.

Table 4.2: Particle sizes and surface areas.

Particle	Particle Diameter (nm)		Surface Area (m^2/g)		
	Reported	Measured	Reported	Measured	Calculated
Synthesized Fe_2O_3	--	131.7[d]	--	--	8.66
Degussa C Al_2O_3	13[a]	11.5[d]	85-115[a] 80[b]	--	163
Linde A Al_2O_3	300[c]	317.0[e] 268.8[d]	14[c]	12.42[g]	--
Linde C Al_2O_3	1000[c]	317.0[d] 360.9[e]	3[c]	--	--
Linde D Al_2O_3	1000[c]	352.5[e] 263.4[d]	15[c]	7.90[g]	--
Praxair B-AF Al_2O_3	50[c]	--	80[c]	--	--
Degussa SiO_2	7[a]	17.5[d]	350 to 410[a]	--	155
$CaCO_3$	-	1.91 to 4.65[f]	--	--	1.6
$Mg(OH)_2$	--	1000 to 2000[f]	--	--	2
CuO	--	--	--	--	--

a Degussa Manufacturer [16]
b Schlautman [17]
c Praxair
d Transmission Electron Microscope
e Photon Correlation Spectroscopy
f Coulter Counter
g BET

Although particle effectiveness at initiating nucleation does not correlate with bulk property size, the active particles could be a small fraction of the total particles with significantly smaller or larger particle size. Degussa C Al_2O_3 particles were uniformly small particles of 11.5 nm diameter, ruling out larger particle sizes being more active. All Linde Al_2O_3 particles showed some fines that were characterized by electron

diffraction as crystalline. The CuO particles were never examined by TEM since they were too large; therefore, it is not known if these particles had fines as well. Particles that had no effect on hydrate formation included SiO_2, with a small measured diameter of 17.5 nm. Unless SiO_2 particles were ineffective for other chemical reasons to be discussed later, these comparisons lead to the conclusion that size is not a determining property of particle activity.

Shape

Particle shapes were shown in Figures 2.7 to 2.12. Iron oxide, silicon dioxide and Degussa C aluminum oxide particles all had uniform shapes, pseudo-cubic and spherical for the latter two. The Linde particles, on the other hand, had highly irregular shapes, with "limbs." The shape of Linde D did not differ from that of Linde A and C. From these results, it seems evident that shape did not have a controlling effect on whether particles made good catalysts for hydrate nucleation.

Surface Area

Again, there was no obvious correlation between surface area and particle effectiveness at decreasing induction time. If surface area were controlling, induction times would presumably have decreased with increasing particle concentrations. There could be an upper or lower limit on concentration above or below which this trend is not seen. It is possible that the concentrations used were either too large or too small, to notice a trend of decreasing induction time with increasing concentration. More conclusive is Figure 4.3, which shows all measured induction times for aluminum oxide particles plotted versus concentration normalized to surface area.

SiO_2 particles with the largest surface area of approximately 400 m^2/g do not seed either carbon dioxide or methane hydrate. In the methane system, concentrations up to 1 g/L were tested. This concentration has about 400 times the surface area of a 0.1 g/L

Linde D suspension that is highly active in reducing induction time for carbon dioxide hydrate.

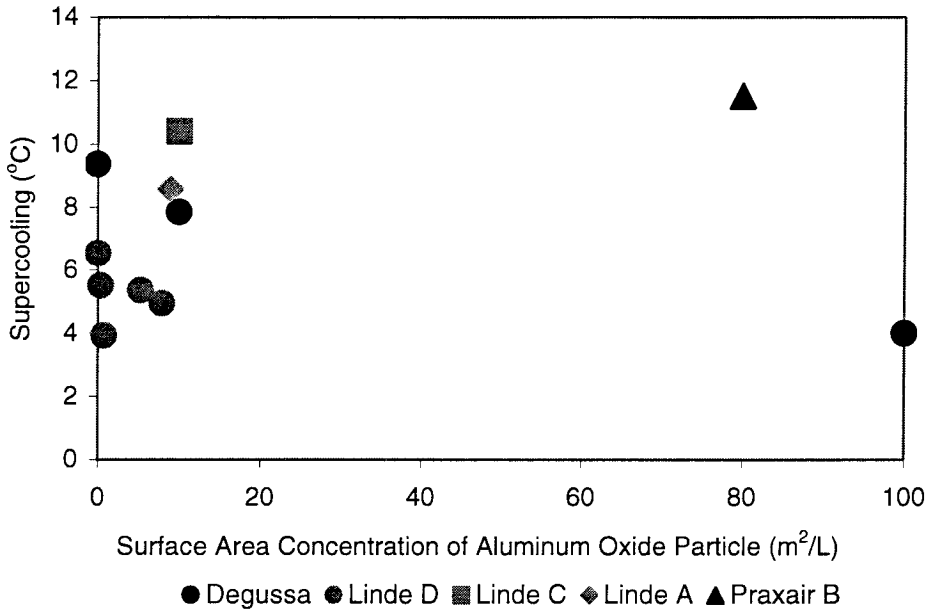

Figure 4.3: Induction times of carbon dioxide hydrate formation versus surface area concentration of all aluminum oxide particles used.

Surface area was not a determining factor. Because the physical variables of the particles: size, shape and surface area, have been ruled out, the chemistry of the particles must account for the discrepancy in aluminum oxide particle activities.

Charge and Functional Groups

The matching of crystal lattice parameters was shown to be fundamental in ensuring good catalytic properties of particles. The location of hydrogen bonding groups on the particle surface needs to match up with those of the hydrate crystal (or ice). The type of hydrogen bonding groups on the particle surface, which are the surface hydroxyl groups, depend on the pH_{pzc} of the particle (listed in Table 4. 3) and the pH of the solution. The pH of our experimental conditions, water saturated with guest gas at a pressure of 5.5 MPa and temperature between 0 and 10 °C is about 3.3 for the CO_2 system and about 7 for the methane system.

In the acidic carbon dioxide solutions, the pH << pH_{pzc} for all particles, except silica, and therefore their surfaces are positively charged with more $\equiv SOH^+$ than $\equiv SOH$ surface groups. The silica particles were negatively charged since the pH > pH_{pzc}. In the methane system, silica particles were negatively charged whereas the other particles were neutrally charged or positively charged for copper oxide particles with a high pH_{pzc} of 11.2.

The percentage of total hydroxyl groups that are positively charged is a function of pH-pH_{pzc}. Because the difference between solution pH and pH_{pzc} of all the aluminum oxides is similar, the percentage of positively charged hydroxyl groups will also be similar. The reported site density of γ-aluminum oxide (Praxair and Degussa) is about 2.5 times that of α-aluminum oxide so the total number of positively charged sites will be greater by 2.5 times as well. This does not, though, explain the difference in activity of the different aluminum oxide particles.

Table 4. 3: Point of zero charge and site densities of particles.

Particle	pH_{pzc}			Site Density (nm^{-2})
	Measured		Reported	
	25 °C	5.2 °C	25 °C	
Synthesized Fe_2O_3	-	-	8.5[a]	4.5[d]
Degussa C Al_2O_3	-	-	8.4[b]	16.9[b]
Linde A Al_2O_3	7.5	>8	9.1[c]	6[f]
Linde C Al_2O_3	5.2	6-7.5	9.1[c]	6[f]
Linde D Al_2O_3	6.9	8.5	9.1[c]	6[f]
Praxair B-AF Al_2O_3	-	-	8.4[a]	16.9[b]
Degussa SiO_2	-	-	2.0[a]	7.9[h]
$CaCO_3$	-	-	-	-
$Mg(OH)_2$	-	11.2	-	-
CuO	-	-	9.5[a]	-

a from Stumm [18]
b from Schlautman [17]
c measured by electrophoresis, Goldberg et al. [19]
d from chemical reactions, James and Parks [20]
e isotopic exchange technique, Goldberg et al. [19]
f estimated from crystal lattice considerations, Goldberg et al. [19]
g for SiO_2 gel James and Parks [20]
h measured, Young [21]

Other differences in surface hydroxyl groups arise from preparation and history of particles. Surface hydroxyl group density of an oxide can be estimated from its crystal structure. Knowledge of the crystal habit, or the exposed edges and faces of the oxide, is important. Crystal preparation techniques determine which crystal faces are exposed and therefore the density of hydroxyl groups. Mechanical disturbance such as grinding to make small particles, leads to an amorphous or disturbed layer with increased surface hydration [19, 22]. Hydration of particles raises the pH_{pzc}, meaning that surfaces become more positively charged. All the oxides of aluminum apparently slowly hydrate (in a matter of days) to the extent that at least a film of material with the properties of $Al(OH)_3$ results [19, 22]. The pH_{pzc} of α-aluminum oxide at equilibrium with water is probably about 9.2. All other values presently available for this material, including those measured in this work, seem to represent metastable or impure states [22]. Surfaces of particles may also vary in degree of crystallinity.

Linde A, C and D aluminum oxide particles used in this work all supposedly have similar crystal structures, with Linde A and D being 90% α and 10% γ and Linde C, 100% α phase. Yet, only Linde D is active with respect to hydrate catalysis, implying differences in their hydroxyl groups, either in density or type. The "aged" Linde D particles lost their ability to catalyze hydrate formation, possibly because of their increased hydration and higher percentage of positively charged sites.

The exact nature of hydroxyl groups that ensure good catalysis of hydrate formation is important, but not well understood.

4.3.2 Summary

Structural match between the exposed crystal face of a nucleating particle and that of ice (or hydrate) is the most important criterion for a good hydrate nucleator. The nature of the surface hydroxyl groups is also important.

The findings of Bylov and Rasmussen [11] support the observations from this laboratory. They found that adding $CaCO_3$, $BaSO_4$, rust and asphaltenes, all at once, eliminated induction times for ethane hydrate formation. $CaCO_3$ was presumably the active particle as rust, or hematite, has been shown to be inactive and $BaSO_4$ is an orthorhombic crystal with large crystal lattice mismatch (a=8.87, b=5.45, c=7.14) and therefore is probably not a good nucleator.

4.4 References

1. W. J. North, J. J. Morgan, "Investigations of CO_2 hydrate formation and dissolution" (California Institute of Technology, 1993).

2. H. Teng, C. M. Kinoshita, S. M. Masutani, *Chemical Engineering Science* **50**, 559-564 (1995).

3. I. Aya, K. Yamane, N. Yamada, Effect of CO_2 concentration in water on the dissolution rate of its clathrate, The International Symposium on CO_2 Fixation and Efficient Utilization of Energy, Tokyo, Japan (RCCU of Tokyo Institute of Technology, 1993).

4. A. Vysniauskas, P. R. Bishnoi, *Chemical Engineering Science* **38**, 1061-1072 (1983).

5. P. Englezos, N. Kalogerakis, P. D. Dholabhi, P. R. Bishnoi, *Chemical Engineering Science* **42**, 2647-2658 (1987).

6. E. D. J. Sloan, *Clathrate Hydrates of Natural Gases*. H. Heineman, Ed., Chemical Industries (Marcel Dekker, Inc., New York, 1990), vol. 39.

7. W. Drost-Hansen, in *Biophysics of Water* F. Franks, Ed. (John Wiley & Sons Limited, New York, 1982).

8. P. A. Vesilind, *Water Environment Research* **66**, 4-11 (1994).

9. R. Larsen, Y. M. Taras, C. A. Knight, E. D. J. Sloan, Growth and inhibition phenomena of single hydrate crystals, Meeting of the American Chemical Society, Division of Fuel Chemistry, San Francisco (1997).

10. T. J. Carver, M. G. B. Drew, P. M. Rodger, *J. Chem. Soc. Faraday Trans.* **91**, 3449-3460 (1995).

11. M. Bylov, P. Rasmussen, The effect of impurities on ethane hydrate induction times, Meeting of the American Chemical Society, Division of Fuel Chemistry, San Francisco (1997).

12. N. Fukuta, *Journal of Meteorology* **15**, 17-26 (1958).

13. V. A. Garten, R. B. Head, *Nature* **205**, 160-162 (1965).

14. C. Klein, C. Hurlbut, *Manual of Mineralogy* (John Wiley and Sons, Inc., New York, 1977).

15. L. Bragg, G. F. Claringbull, W. H. Taylor, *Crystal Structures of Minerals* (Cornell University Press, 1965).

16. Degussa, "Basic characteristics of Aerosil" (Degussa, AG, 1993).

17. M. Schlautman, Ph.D., California Institute of Technology (1992).

18. W. Stumm, *Chemistry of the solid-water interface* (Wiley-Interscience, New York, 1992).

19. S. Goldberg, J. A. Davis, J. D. Hem, in *The Environmental Chemistry of Aluminum* G. Sposito, Ed. (Lewis Publishers, New York, 1996).

20. R. O. James, G. A. Parks, *Surface and Colloid Science* **12**, 119-215 (1982).

21. J. R. Young, Ph.D., California Institute of Technology (1982).

22. G. A. Parks, *Chem. Rev.* **65**, 177-198 (1965).

Chapter 5 Conclusions, Implications and Future Work

5.1 Conclusions

Formation of hydrate occurs first where there is the highest concentration of guest molecules. Guest molecules are needed to stabilize the hydrogen bonded water molecules. Methane hydrate, therefore, only forms at the interface between methane gas and water. Carbon dioxide hydrate forms in the bulk solution because of the higher solubility of carbon dioxide.

Hydrate formation in both pure water and seawater can be catalyzed by particle surfaces. Only the nucleation process itself is catalyzed, resulting in decreased induction periods. The subsequent growth on the hydrate nuclei is not affected. Surface hydroxyl groups on the particles encourage hydrogen bonding between hydroxyl groups and free water molecules near the surface. For particles to be effective catalysts there needs to be good crystal face matching between particles and ice and maybe the clathrate structure itself. Also important is the nature of surface hydroxyl groups.

Calcium carbonate, copper oxide, and Degussa C γ-aluminum oxide and Linde D α-aluminum oxide are efficient hydrate nucleators. 1 g/L calcium carbonate and Degussa C γ-aluminum oxide particle concentrations reduced the degree of supercooling necessary for methane hydrate formation by 53.6 % and 44.8 %, respectively, at a pressure of 5.5 MPa. 1 g/L Degussa C γ-aluminum oxide, Linde D aluminum oxide, and CuO particle concentrations reduced the degree of supercooling necessary for carbon dioxide hydrate formation by 57.4 %, 47.2% and 86 %, respectively, also at a pressure of 5.5 MPa. Linde A, Linde C and Praxair α-aluminum oxide and silicon dioxide, magnesium oxide and iron oxide particles are not good catalysts of hydrate formation.

5.2 Implications

5.2.1 Implications for the laboratory

The ability of certain particles to catalyze hydrate formation highlights the importance of keeping laboratory equipment and solutions entirely free from impurities for the study of homogeneous systems. The near impossibility of eliminating all particulate impurities from the hydrate forming solutions ensures that most systems are not truly homogeneous as thought.

Reactors should be made of inactive materials. Stainless steel, a common reactor material, may not be a suitable choice. Long [1] showed that stainless steel balls and shavings catalyzed hydrate growth. Sapphire, a crystalline aluminum oxide material could be highly active with respect to hydrate catalysis.

5.2.2 Implications for Efficient Hydrate Formation

Spencer and North [2] have proposed sequestering carbon dioxide in the deep oceans by forming carbon dioxide hydrates in a plant at the ocean's surface and then, by pipeline, conveying the hydrate/seawater slurry down to depth. The formation of hydrates at lowered supersaturation, i.e., lower pressures or higher temperatures, would greatly reduce the cost of formation processes. This could be accomplished by seeding of the hydrate reaction. But using particles for this purpose is impractical because of the pollution problem they would cause if injected into the ocean with the hydrate. The seed particles would need to be separated out before transferring the slurry into the ocean. Installing surfaces of high surface area of an active particle may prove more useful. Problems may arise, though, with hydrate forming on and then adhering to the catalytic surfaces.

5.2.3 Implications for Natural Systems

Microscopic particles are naturally present in ocean waters. These particles consist of calcite, aragonite, silica and others. These particles could affect the kinetics of

hydrate formation by acting as hydrate nucleators. The fate of carbon dioxide released in the deep ocean will depend not only on thermodynamic considerations but also kinetic ones. If hydrate were to form on the surface of released carbon dioxide droplets or bubbles, the hydrate coating would affect the density of the droplet or bubble, and hence its tendency to sink or rise. The initiation of hydrate formation on particles could possibly cause hydrate to form earlier than in the absence of particles. Most of the particles in the ocean are either calcium carbonate, which would dissolve in the acidic environment of released carbon dioxide, or silica which has been shown inactive with respect to hydrate formation. Therefore, the effect of these particles on hydrate formation may be small.

Of perhaps more significance is the role of the particulate matter in ocean floor sediments on hydrate formation. Many proposed methods of carbon dioxide sequestration involve transferring the carbon dioxide to the ocean floor, either by releasing the carbon dioxide at very deep depths or by releasing solid carbon dioxide blocks that would sink to the ocean floor [3, 4]. The potential interaction of sediments with released carbon dioxide, seawater and hydrates of carbon dioxide and methane has been modeled by Harrison et al. [5]. Disposing of large quantities of carbon dioxide on the seafloor, at depths greater than 3000 m, would result in a separate carbon dioxide liquid phase overlying the sediments. Dissolution of the carbon dioxide would result in acidified seawater above the sediment and acidified pore water in the sediments beneath. Normally, the seafloor sediment has the capacity to neutralize the acidified seawater by dissolving calcite and clay minerals and incorporating carbon dioxide into carbonates. But Harrison et al. [5] found that large volumes of acidified seawater could deplete the sediment's neutralizing capacity, by causing carbon dioxide hydrate to form in the upper layer of the sediment. The growth of the hydrate causes all reactions between sediment and pore waters to stop because the solid hydrate blocks the pore spaces. Further neutralization by the sediments would thereby cease, reducing the amount of carbon dioxide that the oceans could potentially absorb. Noting that natural occurrences of

carbon dioxide hydrates are rare, Harrison et al. [5] argue that unknown kinetic limitations to hydrate formation might change their predictions. It has been demonstrated in this laboratory and by Brewer at al. [6] that carbon dioxide hydrate does form quite readily in seawater under favorable temperature and pressure conditions. Because sediments consist of calcite, aragonite, and other clay minerals, all of which may catalyze hydrate formation, hydrate formation at the pressures and temperatures of the sediments is suggested to be very favorable and kinetic limitations are not expected.

5.3 Future Work

Further proof of carbon dioxide hydrate formation in homogeneous, bulk solutions is necessary to show that hydrate formation is not only a surface phenomenon. Careful experiments must be designed to eliminate the possibility of liquid droplet surfaces or surface breakup and entrapment in the bulk to avoid mistaking surface hydrate formation with bulk formation. Experimental systems must be kept free of impurities to avoid inadvertent heterogeneous nucleation.

Further study of particle surface catalysis of hydrate formation is warranted to confirm the results presented here. More particles with known crystal structures and preparation techniques should be studied to understand the importance of the nature of surface hydroxyl groups on catalysis activity better.

5.4 References

1. J. Long, Ph.D., Colorado School of Mines (1990).
2. D. F. Spencer, W. J. North, *Energy Conversion and Management* **38**, S265-S271 (1997).
3. C. N. Murray, L. Visintini, G. Bidoglio, B. Henry, *Energy Conversion and Management* **37**, 1067-1072 (1996).
4. E. E. Adams, D. S. Golomb, H. J. Herzog, *Energy Conversion and Management* **36**, 447-452 (1995).
5. W. H. Harrison, R. F. Wendlandt, E. D. Sloan, *Applied Geochemistry* **10**, 461-475 (1995).
6. P. G. Brewer, F. M. Orr, G. Friederich, K. A. Kvenvolden, D. L. Orange, *Energy and Fuels* **12**, 183-188 (1998).

Appendix A: Nuclear Magnetic Resonance Spectroscopy Experiments

A.1 Background

Nuclear magnetic Resonance, or NMR, uses electromagnetic radiation to excite nuclei into higher spin states and then monitors the energy released as the nuclei relax back to their ground state. Nuclei in different chemical environments absorb radiation of different energy, corresponding to different frequencies, expressed as chemical shifts. Nuclei are distinguished, then, by their chemical shifts.

NMR has been used to study hydrates for at least two decades now, mostly by Ripmeester and his group at the National Research Council of Canada [1, 2, 3, 4, 5, 6, 7, 8]. Though originally the focus of these NMR studies was the dynamic and structural aspects of hydrates, the emphasis shifted towards studying the mechanisms and kinetics of hydrate formation.

Ratcliffe and Ripmeester [5] studied CO_2 hydrate using both ^{1}H and ^{13}C NMR. NMR was used to investigate the effect of cage geometry on the motion and orientation of the hydrate guest molecule, CO_2. The CO_2 hydrate was prepared by sealing $^{13}CO_2$ and finely powdered ice in a freezer at –40 °C for over one year. $^{13}CO_2$ line shapes of solid CO_2, CO_2 hydrate at various temperatures and liquid CO_2 were discovered.

The shape, particularly the symmetry, of a hydrate cage affects the line shapes of the guests in the cages to such an extent that guests in different cage types can be distinguished by the shapes of their NMR peaks. The small cage of structure I and large cage of structure II are cubic symmetric or pseudospherical, giving rise to isotropic line shapes for the guests in these cages. The large cage of structure I and small cage of structure II are asymmetrical, having oblate ellipsoidal geometry and thus produce anisotropic line shapes for guests in these cages [4].

Fleyfel et al. [9] studied hydrate precursors of a gas mixture of CH_4 and C_3H_8 in the metastable region. The hydrate was formed in a rocking reactor. Samples were taken when there was visible hydrate in the reactor and after the reactor was heated and the hydrate visually dissociated. Analysis of all samples by ^{13}C NMR showed traces of

methane and propane carbons in different cages of hydrate, showing that microscopic hydrate structure does exist even after hydrate is no longer visible [9].

A.2 Purpose

The objective of our NMR experiments was to determine when and how carbon dioxide hydrate precursors formed. Since there is evidence that water consists of hydrogen bonded clusters that can be stabilized by dissolved molecules, we hypothesized that hydrate precursors might form even below the equilibrium hydrate formation pressure. The first objective was to determine whether water and carbon dioxide molecules rearrange gradually to form intermediates with increasing pressure below the equilibrium hydrate formation pressure or whether hydrate precursors exist only at pressures above the hydrate formation pressure. To do this, the NMR peaks from the carbon nuclei in each of the cages of structure I hydrate were monitored with increasing pressure. We also hoped to measure the rate at which each cage type formed by comparing peak heights, to see whether pentagonal dodecahedral cages, thought to be the building blocks of all hydrates, do indeed form first, leading to he formation of tetrakaidecahedral cages. The nature of water containing dissociated hydrate was also examined, to see if remnants of hydrate structure do remain after dissolution and whether these structures are composed of full lattices with both size cages or if one cage type dominates.

A.3 High Pressure NMR Tube Apparatus and Methodology

A custom-designed high-pressure NMR tube was built to fit directly inside the NMR spectrometer. Carbon dioxide hydrate was formed inside the NMR tube while it was in the NMR instrument. Carbon dioxide was bubbled through several milliliters of water in the tube, to any desired pressure and NMR spectra were taken.

A Bruker 200 MLS NMR spectrometer was used to obtain ^{13}C NMR spectra. The magnet of the spectrometer had an 83 cm long, 5 cm diameter bore hole, into which the sample tube, or reactor, was inserted. The probe was located at the bottom

of this hole, with the observation region about 5 cm in height. The NMR sample tube was a long, thick-walled, 10 mm x 2.2 mm Pyrex tube, custom designed by us to satisfy the geometric constraints of a 10 mm NMR probe and the optical constraints of concentricity and precision needed for NMR. The complete sample tube design is shown in Figure A.1. The glass tube connected to a brass housing that rested on top of the NMR instrument (Figure A.2). A long needle extended from the carbon dioxide input valve to the bottom of the tube to bubble carbon dioxide through the tube.

Hydrate was made from Milli-q water and 99 % ^{13}C enriched carbon dioxide. Carbon dioxide was bubbled from a source outside the NMR instrument, through the needle, to the bottom of the sample tube. The sample tube contained 4 ml of water through which the carbon dioxide gas bubbled up. Experiments were performed in steps of increasing pressure caused by additional carbon dioxide bubbling. At each step, a set amount of time was allowed for the system to stabilize and then 256 NMR scans were taken and averaged to produce a sufficient signal to noise ratio. The maximum pressure increase was limited by safety considerations to about 500 psi. The apparatus was tested both for its capacity to form hydrate and to hold pressure up to 600 psi.

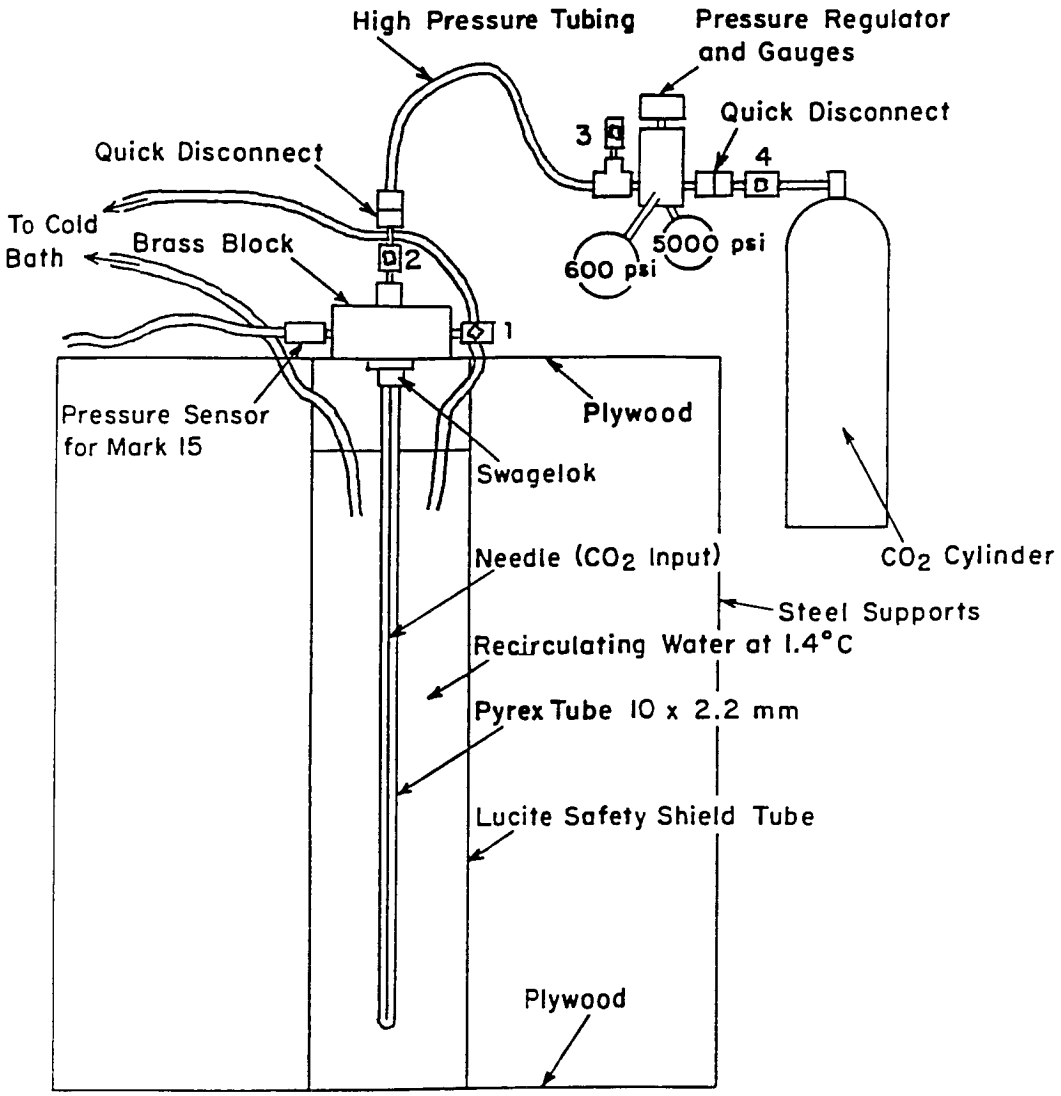

Figure A.1: The complete NMR sample tube/reactor design, shown set up for studies in a cooling bath. The NMR tube, brass housing and pressurizing equipment can be removed from the plywood and Lucite stand and inserted into the NMR spectrometer. Numbers denote valves with the following functions: 1. chamber bleed-off valve; 2. CO_2 input; 3. Bleed-off for high pressure hose; 4. CO_2 cylinder cut-off.

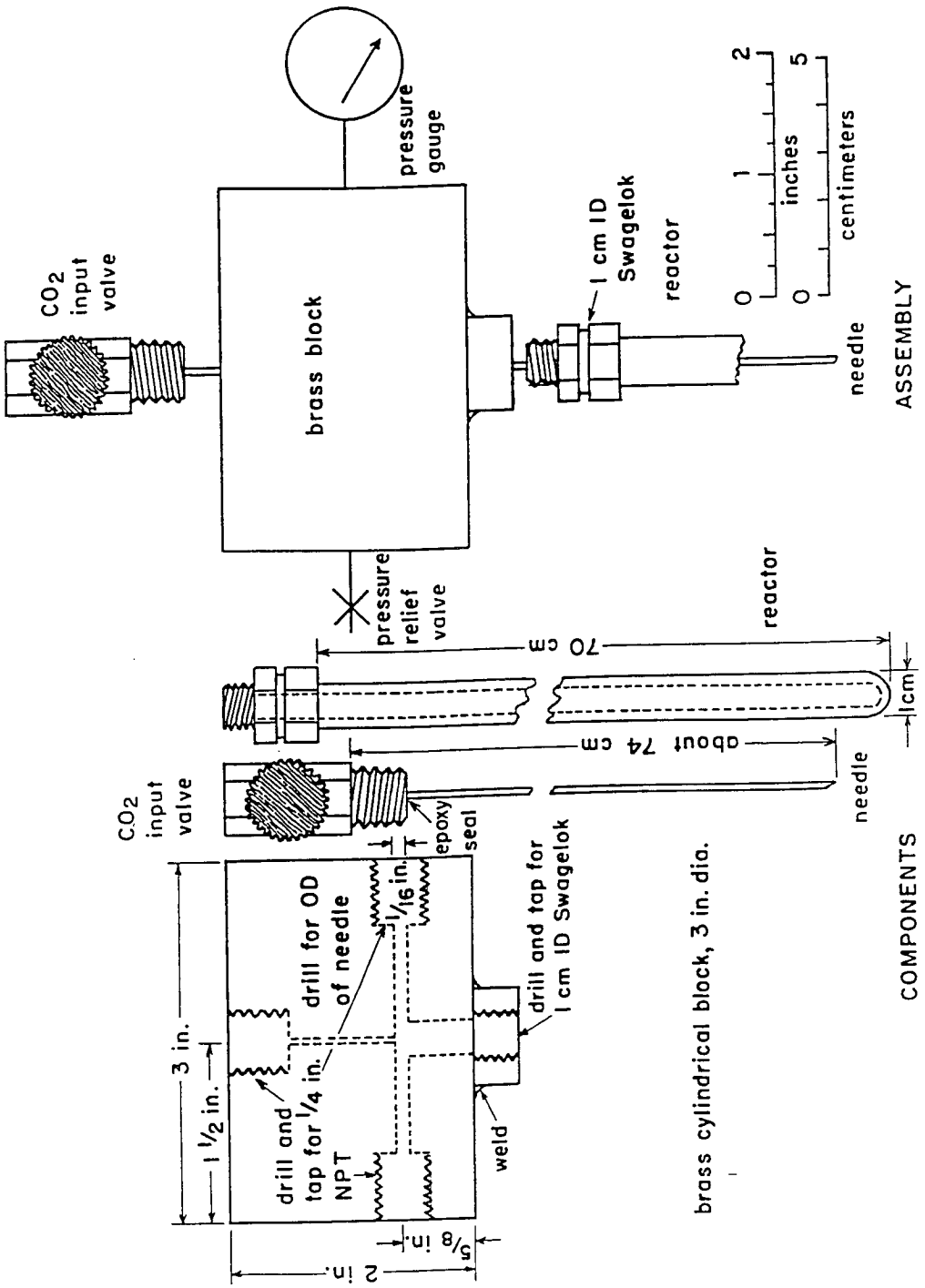

Figure A.2: Detailed diagram of the reactor and associated equipment used to prepare CO_2 hydrate and precursors for analysis by NMR spectroscopy.

A.4 Results and Discussion

A.4.1 Dissolved Carbon Dioxide

The chemical shift of dissolved carbon dioxide in a $^{13}CO_2$ saturated water solution was determined by ^{13}C NMR. The chemical shift of CO_2 hydrate or intermediates was hypothesized to be similar. This experiment was performed in both a standard NMR tube and the high-pressure NMR tube (Figure A.3). The chemical shift of the carbon nucleus of CO_2 was ~128 ppm. The increased thickness of the walls of the high-pressure NMR tube decreased the sensitivity and resolution of the spectrum as evidenced by the diminished S/N and broader peak, respectively. Still, the signal was clear and strong, promising valuable results.

A.4.2 Pressurized Solutions of Carbon Dioxide and Water

Next, $^{13}CO_2$ was bubbled through the tube to raise the pressure, incrementally, to 375 psi (Figure A.4). At atmospheric pressure, the spectrum consisted of only one distinct peak. At increased pressures of 100, 300 and 375 psi, the spectra showed one peak split into two, with chemical shifts of ~126 ppm and ~127 ppm. Hydrate did not form upon pressurizing to 375 psi, even though it was thermodynamically favorable to do so at the experimental temperature of 275 K. This experiment was repeated with similar results (Figure A.5).

A.4.3 Dissociated Hydrate

The nature of water containing dissociated hydrate was also examined to determine if remnants of hydrate structure do remain after dissolution and to determine whether these structures are composed of full lattices of both size cages or if one cage type predominates. Hydrate was formed in the high-pressure sample tube set up in a cold bath; the tube was depressurized and transported to the NMR spectrometer for analysis.

The ^{13}C enrichment was low in this experiment, leading to low S/N. After 256 scans, two peaks were present at ~210.7 ppm and ~69m ppm, possibly due to some remaining, undissociated hydrate, or intermediate (Figure A.6). This experiment was repeated with a higher ^{13}C enrichment resulting in only 1 peak at ~117 ppm, that of $CO_{2(aq)}$ (Figure A.6). The disparity of the two results was caused either by the low S/N in the first experiment giving erroneous peaks or by increased decomposition of the hydrate by the time of analysis in the second experiment.

A.4.4 Hydrate

Determination of the chemical shift of the carbon nucleus in carbon dioxide hydrate was attempted next. Knowing the expected chemical shift of carbon dioxide molecules in hydrate would be useful in analyzing the data already obtained, to determine if the two peaks appearing in some of our experiments were due to hydrate precursor formation. In an attempt to do so, hydrate was formed in a reactor that was then frozen at –80 °C and depressurized. At –80 °C, hydrate is stable at atmospheric pressure. The hydrate was transferred to a standard NMR tube and transported in dry ice to the NMR instrument to be analyzed. The NMR spectrometer was temporarily inoperable and when the sample was finally analyzed two weeks later, the spectrum showed no signs of enclathrated CO_2, only free CO_2 (Figure A.7). Presumably the hydrate dissociated due to low carbon dioxide concentrations, since much of the carbon dioxide was bled off in the depressurizing process.

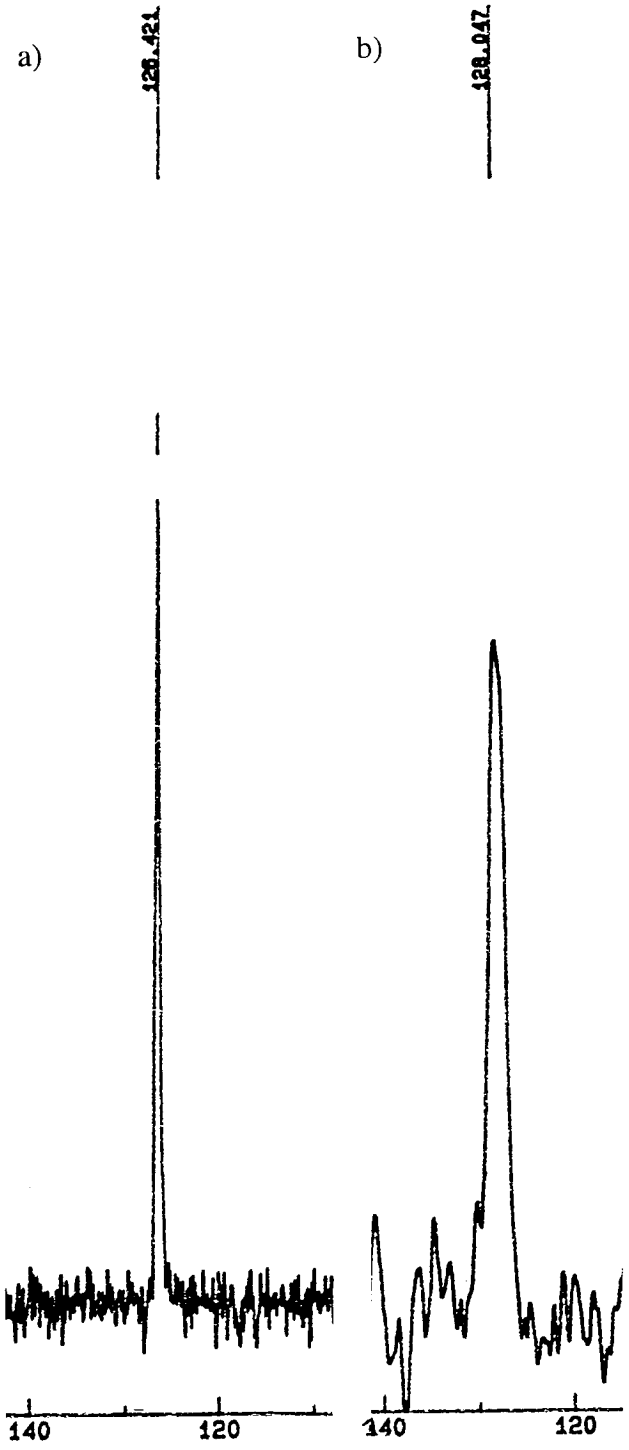

Figure A.3: ^{13}C NMR Spectra of dissolved CO_2 in water at 275 K. a) standard NMR tube; b) high-pressure NMR tube.

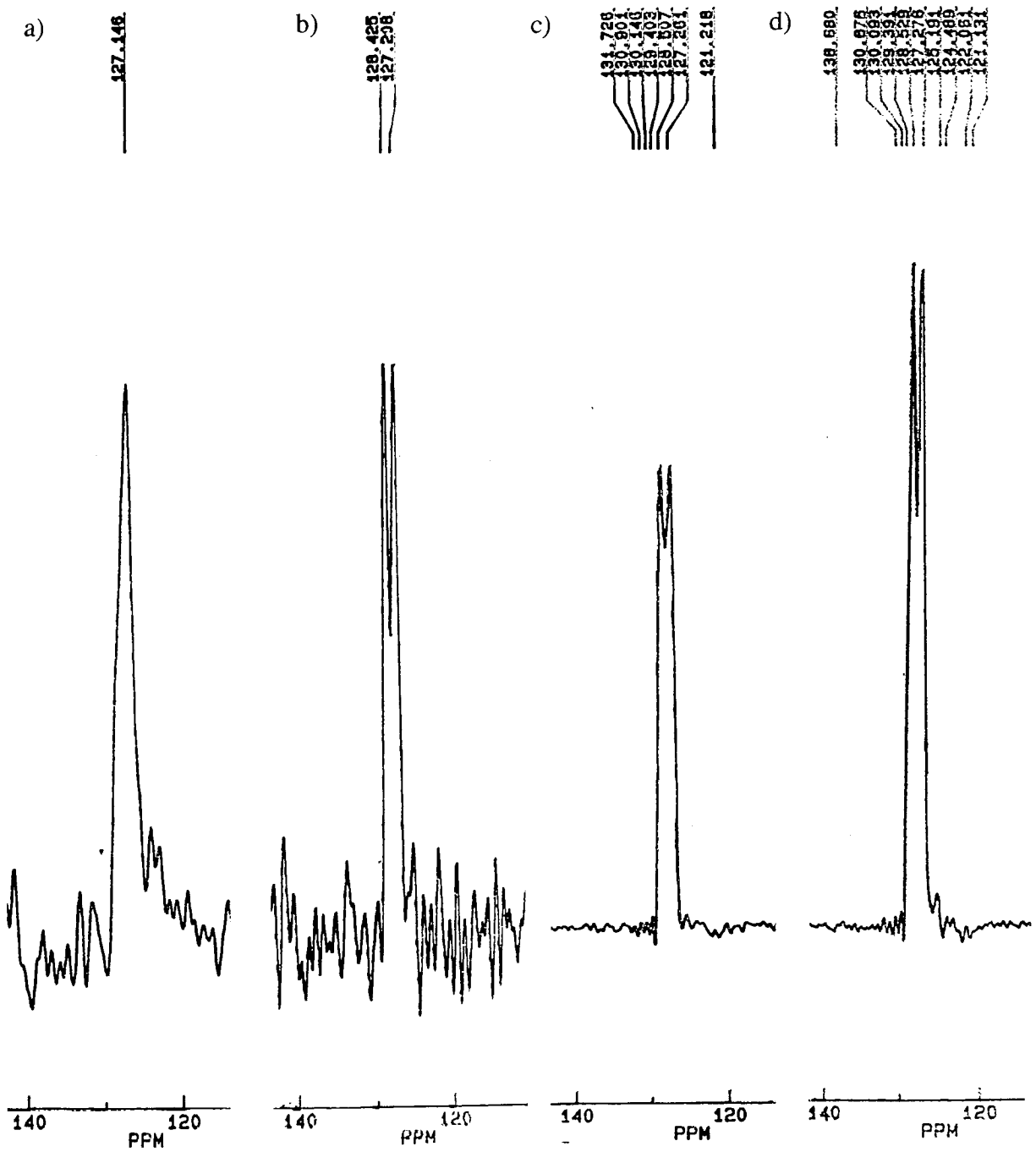

Figure A.4: ^{13}C NMR Spectra of dissolved CO_2 in water at 275 K. a) atmospheric pressure; b) 100 psi; c) 300 psi; d) 375 psi.

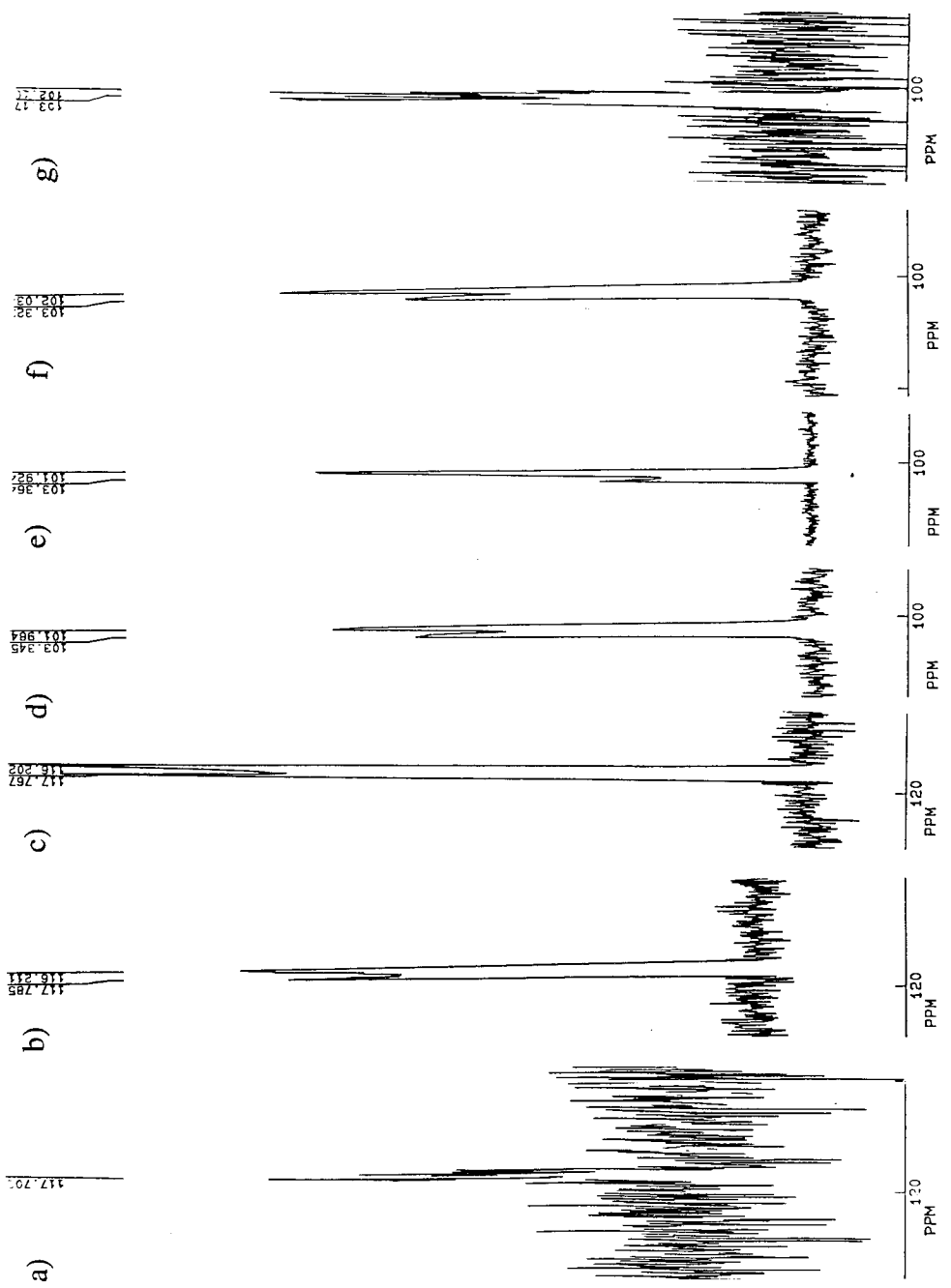

Figure A.5: Second series of ^{13}C NMR spectra of dissolved CO_2 in water at 275 K and increasing pressure. a) 1 atm; b) 239 psi; c) 400 psi; d) depressurized to 228 psi in an attempt to form hydrate; e) 282.5 psi; f) 400 psi; g) final depressurization to 1 atm.

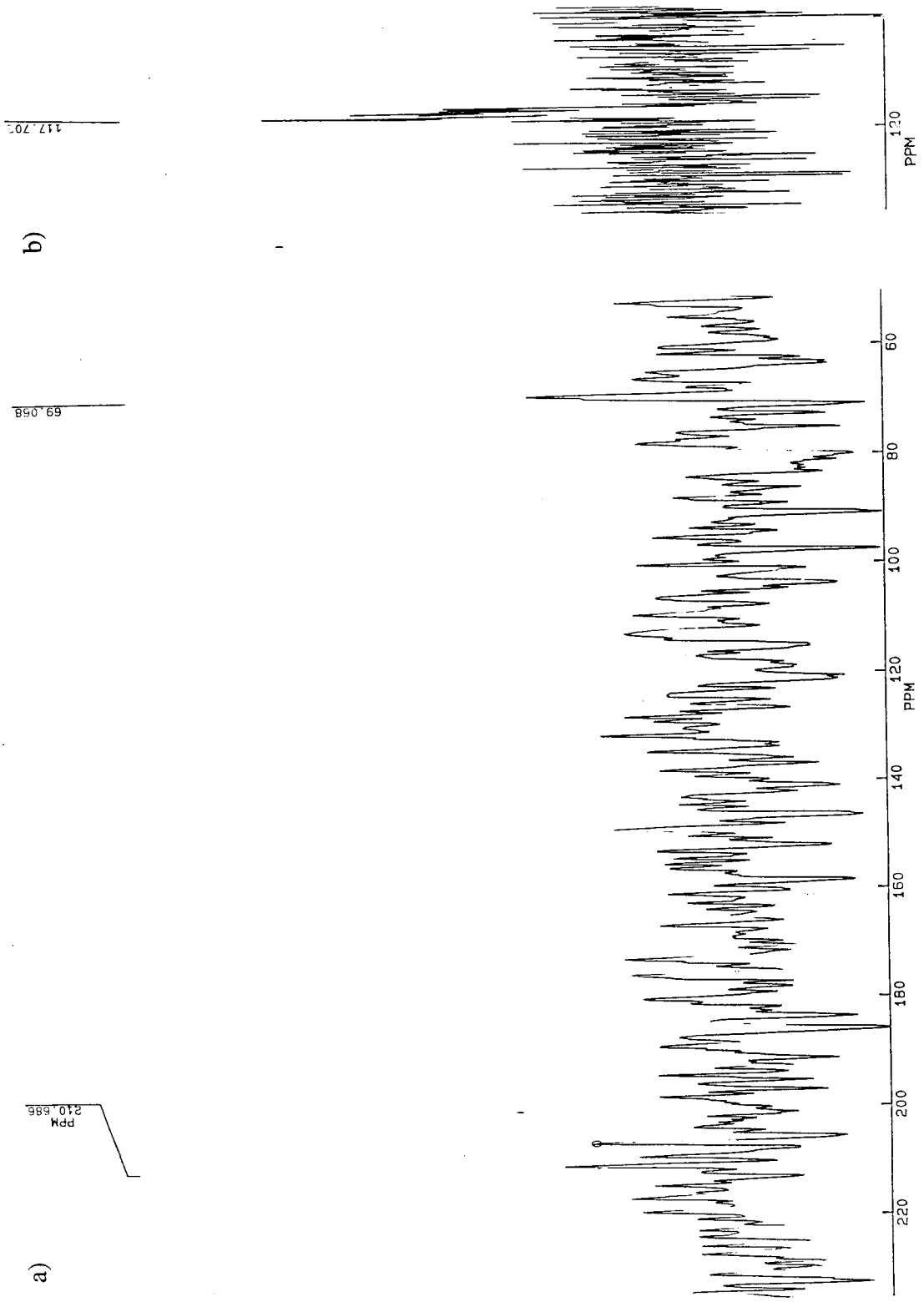

Figure A.6: Spectra of CO_2-water systems following hydrate dissociation. a) peaks at 210.686 and 69.058; b) one peak at 117.70 ppm with higher ^{13}C enrichment.

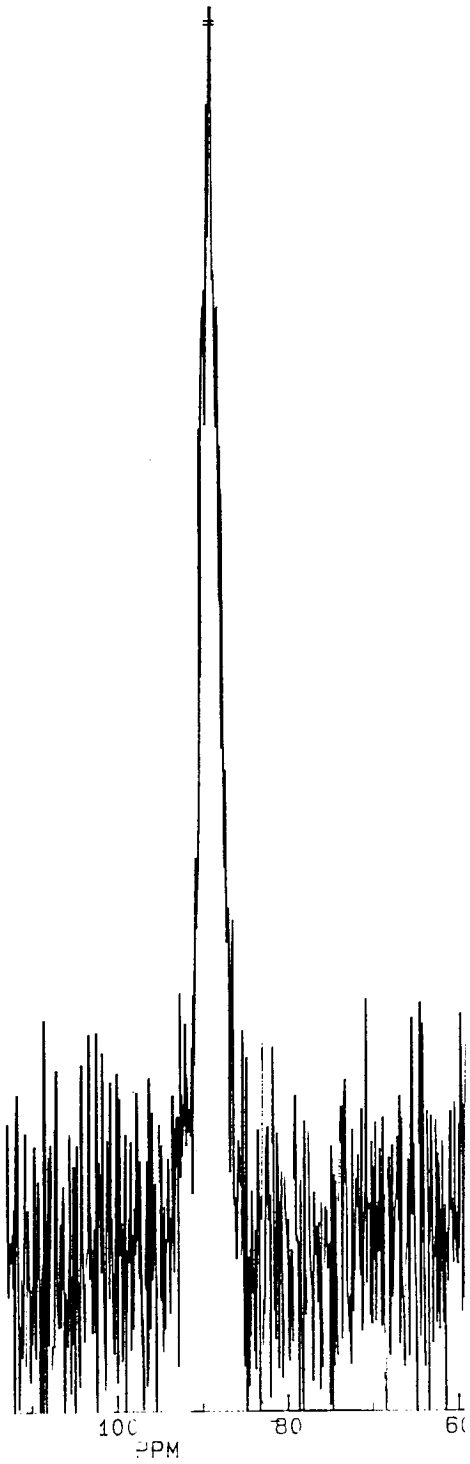

Figure A.7: ^{13}C NMR spectrum of failed CO_2 hydrate, T = -80 °C.

A.5 Problems and Reasons for Discontinuation of NMR Experiments.

Studying hydrate formation with NMR was complicated because of the low temperature and high-pressure constraints and the non-visibility of the NMR tube while in the NMR instrument. All of the experiments performed in the NMR instrument presumably failed to form hydrate. This assumption was based on the appearance of the spectra that failed to show any significant difference between those at pressures below the equilibrium hydrate forming pressure and those above. Because the tube could not be seen inside the spectrometer and removing the pressurized tube to examine its contents was dangerous, ascertaining whether or not hydrate formed was difficult. Hydrate does not form in our experiments, even above the equilibrium hydrate forming pressure because of the low mass transfer of carbon dioxide into the water caused by insufficient mixing and the metastable process of hydrate formation itself which leads to induction periods. In experiments performed outside the NMR instrument, in a cooling bath, the same technique of bubbling carbon dioxide into water usually produced hydrate at pressures above carbon dioxide liquefaction pressure, i.e. much higher than the equilibrium pressure at the experimental temperature. This is a kinetic effect, since if carbon dioxide bubbling is maintained by releasing pressure elsewhere in the apparatus, hydrate does form at lower pressures, but with new water this process took hours. This method cannot be duplicated for NMR studies because of the enormous expense of large quantities of ^{13}C enriched carbon dioxide that are needed. With our present apparatus, hydrate formation was highly inconsistent.

The cost of the NMR experiments was at least 500 dollars per experiment, for the cost of the ^{13}C enriched CO_2 alone. NMR experiments were discontinued because of this prohibitive cost.

A.6 References

1. J. A. Ripmeester, *Canadian Journal of Chemistry* **55**, 78-81 (1977).
2. D. W. Davidson, S. K. Garg, S. R. Gough, R. E. Hawkins, J. A. Ripmeester, *Canadian Journal of Chemistry* **55**, 3641-3650 (1977).
3. J. A. Ripmeester, C. I. Ratcliffe, *Journal of Physical Chemistry* **92**, 337-339 (1988).
4. M. J. Collins, C. I. Ratcliffe, J. A. Ripmeester, *Journal of Physical Chemistry* **94**, 157-162 (1990).
5. C. I. Ratcliffe, J. A. Ripmeester, *Journal of Physical Chemistry* **90**, 1259-1263 (1986).
6. Y. P. Handa, C. I. Ratcliffe, J. A. Ripmeester, J. S. Tse, *Journal of Physical Chemistry* **94**, 4363-4365 (1990).
7. J. A. Ripmeester, C. I. Ratcliffe, *Journal of Physical Chemistry* **94**, 8773-8776 (1990).
8. J. A. Ripmeester, C. I. Ratcliffe, D. D. Klug, J. S. Tse, in *Natural Gas Hydrates* E. D. Sloan, J. Hjappel, M. A. Hnatow, Eds. (New York Academy of Sciences, New York, 1994) pp. 161-175.
9. F. Fleyfel, K. Y. Song, R. Martin, R. Kobayashi, in *Natural Gas Hydrates* E. D. Sloan, J. Hjappel, M. A. Hnatow, Eds. (New York Academy of Sciences, New York, 1994) pp. 212-224.

Appendix B: Data

Methane Hydrate, Milli-q water, No Particles

Experiment	Data File (*.dat)	Hydrate Formation Time (min)	Pressure (psi)	Temperature (°C)	Pressure (MPa)	Teq (°C)	SuperCooling (°C)	Cooling Rate (°C/min)	Induction Time (min)	Initial T (°C)	Final T (°C)	T Spike (°C)
1	NR39	86.50	801.8	5.53	4.04	7.32	3.28	0.0735	44.62	stopped logging too soon		
2	NR40	115.33	802.8	5.54	1.33	7.33	6.00	0.0764	78.54	stopped logging too soon		
3	NR41	101.00	800.4	5.52	3.15	7.30	4.15	0.0722	57.54	3.15	3.2	0.05
4	NR42	104.50	800.2	5.52	2.67	7.30	4.63	0.0742	62.43	2.67	2.78	0.11
5	NR43	108.17	798.5	5.51	2.32	7.28	4.96	0.0748	66.36	2.31	2.43	0.12
6	NR133	120.67	801.2	5.53	1.69	7.31	5.62	0.0762	73.79	1.69	1.82	0.13
7	NR134	124.67	801	5.52	1.51	7.31	5.80	0.0718	80.79	1.51	1.67	0.16
8	NR135	121.00	800.6	5.52	1.69	7.31	5.62	0.0732	76.73	1.69	1.83	0.14
9	NR136	122.67	798.7	5.51	1.42	7.29	5.87	0.0746	78.63	1.42	1.58	0.16
10	NR137	101.08	800	5.52	3.1	7.30	4.20	0.0716	58.66	3.1	3.17	0.07
11	NR138	133.67	800.6	5.52	0.44	7.31	6.87	0.0776	88.49	0.44	0.63	0.19
12	NR139	100.00	800.6	5.52	3.16	7.31	4.15	0.071	58.40	3.16	3.25	0.09
13	NR140	116.08	801.4	5.53	1.91	7.32	5.41	0.0748	72.26	1.91	2.04	0.13
14	NR145	109.08	799.5	5.51	2.78	7.29	4.51	0.0742	60.84	2.78	2.85	0.07
15	NR146	99.67	801.2	5.53	3.62	7.31	3.69	0.0698	52.91	3.62	3.67	0.05
16	NR147	104.00	798.5	5.51	3.03	7.28	4.25	0.0784	54.25	3.03	3.09	0.06
17	NR148	109.33	802.8	5.54	2.29	7.33	5.04	0.0743	67.84	2.29	2.43	0.14
18	NR149	141.58	802	5.53	-0.1	7.32	7.42	0.0744	99.76	-0.18	0.07	0.25
19	NR150	125.67	802.4	5.53	1.09	7.33	6.24	0.0747	83.48	1.09	1.29	0.2
20	NR151	112.08	801.2	5.53	2.3	7.31	5.01	0.0727	68.96	2.3	2.43	0.13
21	NR152	91.33	801.2	5.53	4.07	7.31	3.24	0.0691	46.93	4.07	4.12	0.05
22	NR153	97.58	801.4	5.53	3.7	7.32	3.62	0.0706	51.21	3.7	3.71	0.01
23	NR154	133.50	800.8	5.52	0.87	7.31	6.44	0.0732	87.96	0.87	1.06	0.19
24	NR155	101.58	797.9	5.50	3.3	7.28	3.98	0.0707	56.25	3.3	3.35	0.05

Methane Hydrate, Milli-q water, No Particles (continued)

Experiment	Data File (*.dat)	Hydrate Formation Time (min)	Pressure (psi)	Temperature (°C)	Pressure (MPa)	Teq (°C)	SuperCooling (°C)	Cooling Rate (°C/min)	Induction Time (min)	Initial T (°C)	Final T (°C)	T Spike (°C)
25	NR156	138.00	801.2	5.53	0.98	7.31	6.33	0.0747	84.78	0.98	1.18	0.2
26	NR157	174.50	799.5	5.51	-2.24	7.29	9.53	0.0768	124.15	No Hydrate		
27	NR158	137.08	801	5.52	0.37	7.31	6.94	0.0779	89.10	0.37	0.57	0.2
28	NR159	169.00	801.8	5.53	-2.4	7.32	9.72	0.0786	123.66	No Hydrate		
						Average:	**5.13**		**69.29**			
						St. Dev:	**1.19**		**14.79**			

Methane Hydrate, Milli-Q water, Seed: SiO_2

Experiment	Seed (g/L)	Data File (*.dat)	Time (min)	Hydrate formation Pressure (psi)	Pressure (MP+F52a)	Temperature (C)	Equil. Temp. (C)	SuperCooling (C)	Cooling Rate (C/min)	Induction Time (min)
1	0.2	NR84	70.67	797.7	5.501	4.97	7.27	2.30	0.0735	31.35
2	0.2	NR85	96.67	798.5	5.507	3.03	7.28	4.25	0.0730	58.27
3	0.2	NR86	105.67	798.1	5.504	2.33	7.28	4.95	0.0729	67.89
4	0.2	NR87	91.67	798.1	5.504	3.46	7.28	3.82	0.0725	52.68
5	0.2	NR88	73.25	799.1	5.511	4.95	7.29	2.34	0.0716	32.68
							Average:	**3.53**		48.57
							St. Dev:	**1.18**		16.07
1	0.4	NR90	76	797.7	5.501	4.47	7.27	2.80	0.0765	36.66
2	0.4	NR91	89	799.7	5.515	3.74	7.30	3.56	0.0757	46.98
3	0.4	NR92	108.67	800.4	5.520	2.16	7.30	5.14	0.0739	69.61
4	0.4	NR93	89.5	799.5	5.514	3.69	7.29	3.60	0.0743	48.51
5	0.4	NR94	110	800.6	5.521	2.07	7.31	5.24	0.0745	70.29
							Average:	**4.07**		54.41
							St. Dev:	**1.07**		14.90

Methane Hydrate, Milli-Q water, Seed: SiO_2 (continued)

Experiment	Seed (g/L)	Data File (*.dat)	Time (min)	Hydrate formation Pressure (psi)	Pressure (Mpa)	Temperature (C)	Equil. Temp. (C)	SuperCooling (C)	Cooling Rate (C/min)	Induction Time (min)
1	1	NR96	97.67	800.4	5.520	2.99	7.30	4.31	0.0739	58.38
2	1	NR97	95.67	800	5.517	3.19	7.30	4.11	0.0711	57.80
3	1	NR100	81.42	802.2	5.532	4.28	7.32	3.04	0.0710	42.87
4	1	NR101	133.5	801.4	5.527	0.28	7.32	7.04	0.0747	94.18
5	1	NR102	112.67	801	5.524	1.87	7.36	5.49	0.0715	76.84
							Average:	**4.80**		66.02
							St. Dev:	**1.52**		19.82

Methane Hydrate, Milli-Q water, Seed: Al_2O_3

Experiment	Seed (gL)	Data File (*.dat)	Time (min)	Hydrate Formation Pressure (psi)	Pressure (Mpa)	Temperature (C)	Teq (C)	SuperCooling (C)	Cooling Rate (C/min)	Induction Time (min)
1	1	NR49	86	802.4	5.534	4.26	7.33	3.07	0.0868	35.33
2	1	NR50	86	802.8	5.537	4.09	7.33	3.24	0.0703	46.10
3	1	NR51	84.33	801.8	5.530	4.27	7.32	3.05	0.0706	43.20
4	1	NR52	76.67	801.2	5.526	4.88	7.31	2.43	0.0745	32.66
5	1	NR53	86.42	800.8	5.523	4	7.31	3.31	0.0725	45.64
							Average:	**3.02**		40.58
							St. Dev:	**0.35**		6.19

Methane Hydrate, Milli-Q water, Seed: Al_2O_3 (continued)

Experiment	Seed (gL)	Data File (*.dat)	Time (min)	Hydrate Formation Pressure (psi)	Hydrate Formation Pressure (Mpa)	Temperature (C)	Teq (C)	SuperCooling (C)	Cooling Rate (C/min)	Induction Time (min)
1	0.2	NR54	79	801.4	5.527	4.84	7.32	2.48	0.0685	36.14
2	0.2	NR55	96.42	801.6	5.528	3.53	7.32	3.79	0.0713	53.12
3	0.2	NR56	81.33	801.4	5.527	4.68	7.32	2.64	0.0717	36.75
4	0.2	NR57	100	799.5	5.514	3.23	7.29	4.06	0.0719	56.53
5	0.2	NR58	75.67	800.6	5.521	5.04	7.31	2.27	0.0693	32.71
							Average:	**3.05**		43.05
							St. Dev:	**0.82**		10.93
1	0.6	NR59	90.67	800.4	5.520	4.14	7.30	3.16	0.0708	44.69
2	0.6	NR60	77	801.6	5.528	5.1	7.32	2.22	0.0676	32.80
3	0.6	NR61	80	802.8	5.537	5.23	7.33	2.10	0.0733	28.66
4	0.6	NR62	66.42	800.2	5.519	5.26	7.30	2.04	0.0694	29.43
5	0.6	NR63	70	800	5.517	4.99	7.30	2.31	0.0734	31.47
							Average:	**2.37**		33.41
							St. Dev:	**0.46**		6.52
1	1	NR64	70	800.8	5.523	5.03	7.31	2.28	0.0723	31.52
2	1	NR65	84.67	800.8	5.523	3.87	7.31	3.44	0.0742	46.34
3	1	NR66	72.17	800.8	5.523	4.85	7.31	2.46	0.0749	32.83
4	1	NR67	79.67	801.4	5.527	4.34	7.32	2.98	0.0773	38.49
5	1	NR68	67	800.8	5.523	5.28	7.31	2.03	0.0736	27.56
							Average:	**2.64**		35.35
							St. Dev:	**0.57**		7.29

Methane Hydrate, Milli-Q water, Seed: $CaCO_3$

Experiment	Seed (g/L)	Data File (*.dat)	Time (min)	Hydrate Formation Pressure (psi)	Hydrate Formation Pressure (Mpa)	Temperature (°C)	Equil. Temp. (°C)	SuperCooling (°C)	Cooling Rate (°C/min)	Induction Time (min)
1	0.2	NR34	91.17	798.5	5.51	3.92	7.28	3.36	0.0814	41.32
2	0.2	NR35	88.17	796.9	5.50	4.03	7.27	3.24	0.0757	42.74
3	0.2	NR36	81.67	796.5	5.49	4.36	7.26	2.90	0.0717	40.46
4	0.2	NR37	83.67	800.4	5.52	4.34	7.30	2.96	0.0721	41.11
5	0.2	NR38	94.67	801.8	5.53	3.76	7.32	3.56	0.0698	51.00
							Average:	**3.20**		43.33
							St. Dev:	**0.27**		4.37
1	1	NR44	83	789.3	5.44	4.54	7.18	2.64	0.0735	35.94
2	1	NR45	75.67	798.7	5.51	5.13	7.29	2.16	0.0736	29.29
3	1	NR46	75.33	797.5	5.50	4.97	7.27	2.30	0.0756	30.45
4	1	NR47	83	796.7	5.49	4.43	7.26	2.83	0.0741	38.24
5	1	NR48	73.5	796.3	5.49	5.27	7.26	1.99	0.0725	27.44
							Average:	**2.38**		32.27
							St. Dev:	**0.35**		4.60

Methane Hydrate, Milli-Q water, Seed: $CaCO_3$ (continued)

Experiment	Seed (g/L)	Data File (*.dat)	Time (min)	Hydrate Formation Pressure (psi)	Hydrate Formation Pressure (MPa)	Temperature (°C)	Equil. Temp. (°C)	SuperCooling (°C)	Cooling Rate (°C/min)	Induction Time (min)
1	0.6	NR69	75.42	801.8	5.53	4.57	7.32	2.75	0.0747	36.81
2	0.6	NR70	72	801.8	5.53	4.76	7.32	2.56	0.0718	35.65
3	0.6	NR71	83.67	802.4	5.53	4.41	7.33	2.92	0.0755	38.63
4	0.6	NR72	75	802.4	5.53	4.85	7.33	2.48	0.0726	34.11
5	0.6	NR73	76	801.8	5.53	4.67	7.32	2.65	0.0784	33.80
							Average:	**2.67**		35.80
							St. Dev:	**0.17**		1.99
1	0.1	NR74	82.5	802	5.53	4.3	7.32	3.02	0.0747	40.45
2	0.1	NR75	74.24	802.6	5.54	4.86	7.33	2.47	0.0718	34.38
3	0.1	NR76	76.67	803.8	5.54	4.74	7.34	2.60	0.0727	35.79
4	0.1	NR77	95	800.5	5.52	3.17	7.31	4.14	0.0753	54.92
5	0.1	NR78	79.42	800.4	5.52	4.4	7.30	2.90	0.0737	39.41
							Average:	**3.03**		40.99
							St. Dev:	**0.66**		8.18

Methane Hydrate, Milli-Q water, Seed: $CaCO_3$ (continued)

Experiment	Seed (g/L)	Data File (*.dat)	Time (min)	Hydrate Formation Pressure (psi)	Hydrate Formation Pressure (MPa)	Temperature (°C)	Equil. Temp. (°C)	SuperCooling (°C)	Cooling Rate (°C/min)	Induction Time (min)
1	0.1	NR104	89.17	802	5.53	3.65	7.32	3.67	0.0722	50.86
2	0.1	NR105	84.67	803	5.54	4.01	7.33	3.32	0.0727	45.71
3	0.1	NR106	87	801.4	5.53	3.87	7.32	3.45	0.0718	47.99
4	0.1	NR107	-	800	5.52	5.5	7.30	1.80	0.0705	25.53
5	0.1	NR108	83.5	800.2	5.52	4.16	7.30	3.14	0.0759	41.40
6	0.1	NR109	84.67	801.2	5.53	4.01	7.31	3.30	0.0710	46.52
7	0.1	NR110	79.67	801.2	5.53	4.41	7.31	2.90	0.0715	40.60
Note: Did not include NR104 nad NR107 in statistical analysis because stir bar was off center and not rotating properly							Average:	**3.22**		44.44
							St. Dev:	**0.26**		3.26
1	0.04	NR111	95.25	801.6	5.53	3.23	7.32	4.09	0.0733	55.76
2	0.04	NR112	103.67	800.8	5.52	2.55	7.31	4.76	0.0733	64.92
3	0.04	NR113	99.67	801.4	5.53	2.91	7.32	4.41	0.0730	60.35
4	0.04	NR114	98.25	802.2	5.53	3.01	7.32	4.31	0.0734	58.78
5	0.04	NR115	82.08	801	5.52	4.18	7.31	3.13	0.0719	43.55
							Average:	**4.14**		56.67
							St. Dev:	**0.61**		8.05

Methane Hydrate, Milli-Q water, Seed: $CaCO_3$ (continued)

Experiment	Seed (g/L)	Data File (*.dat)	Time (min)	Hydrate Formation Pressure (psi)	Hydrate Formation Pressure (MPa)	Temperature (°C)	Equil. Temp. (°C)	SuperCooling (°C)	Cooling Rate (°C/min)	Induction Time (min)
1	0.02	NR116	113.67	801.4	5.53	1.71	7.32	5.61	0.0746	75.14
2	0.02	NR117	102.5	801.2	5.53	2.59	7.31	4.72	0.0733	64.44
3	0.02	NR118	91	800.8	5.52	3.45	7.31	3.86	0.0725	53.22
4	0.02	NR119	85.66	801	5.52	3.88	7.31	3.43	0.0703	48.80
5	0.02	NR120	108	800.4	5.52	2.21	7.30	5.09	0.0736	69.22
							Average:	**4.54**		62.16
							St. Dev:	**0.89**		10.97

Methane Hydrate, Milli-Q water, Inhibitor: 1 g/l Polyvinylpyrolidone

Experiment	Seed (g/L)	Data File (*.dat)	Time (min)	Hydrate Formation Pressure (psi)	Hydrate Formation Pressure (MPa)	Temperature (°C)	Teq (°C)	SuperCooling (°C)	Cooling Rate (°C/min)	Induction Time (min)	Initial T (°C)	Final T (°C)	T Spike (°C)
1	1	NR184	174.5	803.2	5.539	-3.28	7.34	10.62	0.0809	131.21	-3.28	-3.05	0.23
2	1	NR185	144.67	802	5.531	-0.51	7.32	7.83	0.0795	98.51	-0.51	-0.41	0.1
3	1	NR186	121.67	801.6	5.528	1.44	7.32	5.88	0.0788	74.59	1.44	1.45	0.01
4	1	NR187	181	800	5.517	-3.48	7.30	10.78	0.0781	138.03	Solution Froze, No Hyd.		
5	1	NR188	143.08	800.6	5.521	0.22	7.31	7.09	0.0775	91.44	0.22	0.27	0.05
6	1	NR189	157.08	801.6	5.528	-0.88	7.32	8.20	0.0774	105.91	-0.89	-0.77	0.12
7	1	NR190	155.67	799.7	5.515	-1.05	7.30	8.35	0.0789	105.79	-1.05	-0.94	0.11
8	1	NR191	157.42	800.2	5.519	-1.52	7.30	8.82	0.0767	115.02	-1.52	-1.36	0.16
9	1	NR192	197.33	799.7	5.515	-4.21	7.30	11.51	0.0767	150.02	Solution Froze, No Hyd.		
10	1	NR193	170	799.5	5.514	-2.32	7.29	9.61	0.0786	122.32	-2.32	-2.11	0.21
							Average:	**8.87**		**113.28**			
							St. Dev:	**1.77**		**22.78**			

Methane Hydrate: Artificial Seawater, Seed: 1 gl Al_2O_3

Experiment	Data File (*.dat)	Time (min)	Hydrate Formation Pressure (psi)	Hydrate Formation Temperature (°C)	Pressure (MPa)	Teq (°C)	SuperCooling (°C)	Cooling Rate (°C/min)	Induction Time (min)	Initial T (°C)	Final T (°C)	T Spike (°C)
1	NR205	97.58	798.7	3.38	5.508	6.17	2.79	0.0799	34.88	3.38	3.38	0
2	NR206	128.17	798.1	1.07	5.504	6.16	5.09	0.0791	64.35	1.07	1.16	0.09
3	NR207	115.5	798.3	1.92	5.506	6.16	4.24	0.0704	60.26	1.91	1.93	0.02
4	NR208	102.67	799.3	2.86	5.512	6.17	3.31	0.0788	42.06	2.86	2.88	0.02
5	NR209	116.67	798.3	1.91	5.506	6.16	4.25	0.0795	53.49	1.91	1.96	0.05
6	NR210	112.33	798.1	1.82	5.504	6.16	4.34	0.0802	54.11	1.81	1.87	0.06
7	NR211	113.08	796.5	1.72	5.493	6.14	4.42	0.0798	55.40	1.72	1.76	0.04
8	NR212	104.08	797.3	2.56	5.499	6.15	3.59	0.0804	44.65	2.56	2.59	0.03
9	NR213	102.33	799.7	3.11	5.515	6.18	3.07	0.0781	39.29	3.11	3.11	0
10	NR214	133.08	803	0.45	5.538	6.22	5.77	0.0794	72.65	0.45	0.54	0.09
						Average:	**4.09**		**52.11**			
						St. Dev:	**0.92**		**11.89**			

Methane Hydrate, Artificial Seawater, No Seed

Experiment	Data File (*.dat)	Time (min)	Hydrate Formation Pressure (psi)	Hydrate Formation Pressure (MPa)	Temperature (°C)	Teq (°C)	SuperCooling (°C)	Cooling Rate (°C/min)	Induction Time (min)	Initial T (°C)	Final T (°C)	T Spike (°C)
1	NR194	140.67	800	5.517	-0.1	6.18	6.28	0.0800	78.53	-0.1	0.01	0.11
2	NR195	174.67	800.6	5.521	-2.65	6.19	8.84	0.0787	112.32	-2.65	-2.43	0.22
3	NR196	137.67	799.1	5.511	0.18	6.17	5.99	0.0794	75.46	0.18	0.3	0.12
4	NR197	179	800	5.517	-3.19	6.18	9.37	0.0779	120.31	-3.19	-2.96	0.23
5	NR198	165.67	798.5	5.507	-2.4	6.16	8.56	0.0766	111.81	-2.4	-2.18	0.22
6	NR199	209	798.7	5.508	-5.28	6.17	11.45	0.0768	149.05	-5.28	-4.95	0.33
7	NR200	199.67	798.9	5.510	-4.51	6.17	10.68	0.0787	135.70	-4.51	-4.21	0.3
8	NR201	141.33	797.3	5.499	0	6.15	6.15	0.0777	79.15	0	0.09	0.09
9	NR202	142.67	799.1	5.511	-0.22	6.17	6.39	0.0789	81.01	-0.22	-0.11	0.11
10	NR203	184.33	799.5	5.514	-3.56	6.18	9.74	0.0788	123.56	-3.56	-3.31	0.25
						Average:	**8.35**		**105.84**			
						St. Dev:	**2.02**		**27.94**			

Carbon Dioxide Hydrate, Milli-Q Water, No Seed, Stirring Rate = 450 rpm

Experiment	Data File (*.dat)	Hydrate Formation Time (min)	Pressure (psi)	Temperature (°C)	Pressure (MPa)	Teq (°C)	SuperCooling (°C)	Cooling Rate (°C/min)	Induction Time (min)	Initial T (°C)	Final T (°C)	T Spike (°C)
1	NR215	191	801.8	1.59	5.530	9.787	8.20	0.0803	102.08	1.59	6.12	4.53
2	NR216	189	802	-2.93	5.531	9.787	12.72	0.1083	117.42	-2.93	3.43	6.36
3	NR217	243.17	804	-2.46	5.545	9.788	12.25	0.0868	141.11	-2.46	3.75	6.21
4	NR218	170.67	800.2	3.15	5.519	9.787	6.64	0.0948	70.01	3.15	6.65	3.5
5	NR219	199.08	800	0.84	5.517	9.787	8.95	0.0861	103.91	0.84	5.53	4.69
6	NR220	238.17	799.5	-3.1	5.514	9.786	12.89	0.0874	147.44	-3.1	3.12	6.22
7	NR221	225	802.4	-1.29	5.534	9.788	11.08	0.0927	119.50	-1.29	4.16	5.45
8	NR222	190.17	797.9	1.24	5.503	9.786	8.55	0.0895	95.49	1.24	5.54	4.3
9	NR223	171.67	798.3	2.85	5.506	9.786	6.94	0.0843	82.28	2.85	6.62	3.77
10	NR224	161.5	796.9	4.18	5.496	9.785	5.61	0.0878	63.84	4.18	7.29	3.11
						Average:	**9.38**		**102.51**			
						St. Dev:	**2.68**		**33.52**			

Carbon Dioxide Hydrate, Milli-Q Water, No Seed, Reduced Stirring Rate = 275 rpm

Experiment	Data File (*.dat)	Hydrate Formation Time (min)	Pressure (psi)	Temperature (°C)	Pressure (MPa)	Teq (°C)	SuperCooling (°C)	Cooling Rate (°C/min)	Induction Time (min)	Initial T (°C)	Final T (°C)	T Spike (°C)
1	NR225	211.25	802.2	-0.44	5.532	9.787	10.23	0.0879	116.35	-0.44	4.37	4.81
2	NR226	257.67	801.8	-3.98	5.530	9.787	13.77	0.0825	166.87	-3.98	2.3	6.28
3	NR227	296	797.8	-5.82	5.502	9.788	15.61	0.0796	196.08	-5.82	1.8	7.62
						Average:	**13.20**		**159.77**			
						St. Dev:	**2.73**		**40.34**			

Carbon Dioxide Hydrate, Milli-Q Water, 1 g/l Unwashed Degussa Al_2O_3 C, Stirring Rate = 450 rpm

Experiment	Data File (*.dat)	Hydrate Formation Time (min)	Pressure (psi)	Temperature (°C)	Pressure (MPa)	Teq (°C)	SuperCooling (°C)	Cooling Rate (°C/min)	Induction Time (min)	Initial T (°C)	Final T (°C)	T Spike (°C)
1	NR229	148	801.2	5.4	5.526	9.787	4.39	0.0914	48.00	5.4	8.05	2.65
2	NR230	135	801.4	7.01	5.527	9.787	2.78	0.0923	30.09	7.01	8.72	1.71
3	NR231	164	802.6	4.99	5.535	9.788	4.80	0.0928	51.70	4.99	7.67	2.68
4	NR232	184.67	801	2.81	5.524	9.787	6.98	0.0874	79.83	2.81	6.91	4.1
5	NR233	137.33	807.8	7.09	5.571	9.790	2.70	0.0904	29.87	7.09	8.71	1.62
						Average:	**4.33**		**47.90**			
						St. Dev:	**1.75**		**20.47**			

Carbon Dioxide Hydrate, Milli-Q Water, 0.2 g/l Degussa Al_2O_3 C, Stirring Rate = 450 rpm

Experiment	Data File (*.dat)	Hydrate Formation Time (min)	Pressure (psi)	Temperature (°C)	Pressure (MPa)	Teq (°C)	SuperCooling (°C)	Cooling Rate (°C/min)	Induction Time (min)	Initial T (°C)	Final T (°C)	T Spike (°C)
1	NR234	153.42	799.7	6.05	5.515	9.786	3.74	0.0898	41.60	6.05	8.38	2.33
2	NR235	191.08	797.1	2.08	5.497	9.785	7.71	0.0928	83.03	2.08	6.46	4.38
3	NR236	126.42	793.1	7.46	5.470	9.783	2.32	0.0858	27.07	7.46	8.89	1.43
						Average:	**4.59**		**50.57**			
						St. Dev:	**2.79**		**29.03**			

Carbon Dioxide Hydrate, Milli-Q Water, 1 g/l Degussa Cleaned Al_2O_3 C, Stirring Rate = 450 rpm

Experiment	Data File (*.dat)	Hydrate Formation Time (min)	Pressure (psi)	Temperature (°C)	Pressure (MPa)	Teq (°C)	SuperCooling (°C)	Cooling Rate (°C/min)	Induction Time (min)	Initial T (°C)	Final T (°C)	T Spike (°C)
1	NR237	177	796.5	2.88	5.493	9.785	6.91	0.0891	77.50	2.88	6.67	3.79
2	NR238	189.67	801.2	1.9	5.526	9.787	7.89	0.0854	92.35	1.9	6.15	4.25
3	NR239	188.42	800.8	2.77	5.523	9.787	7.02	0.0934	75.13	2.77	6.66	3.89
4	NR240	206.5	802	0.07	5.531	9.787	9.72	0.0908	107.02	0.07	5.3	5.23
5	NR241	231.58	801.4	-1.76	5.527	9.787	11.55	0.0881	131.07	-1.76	3.89	5.65
						Average:	**8.61**		**96.61**			
						St. Dev:	**1.99**		**23.13**			

Carbon Dioxide Hydrate, Milli-Q Water, 1 g/l Degussa Uncleaned Al_2O_3 C, Stirring Rate = 450 rpm

Experiment	Data File (*.dat)	Hydrate Formation Time (min)	Pressure (psi)	Temperature (°C)	Pressure (MPa)	Teq (°C)	SuperCooling (°C)	Cooling Rate (°C/min)	Induction Time (min)	Initial T (°C)	Final T (°C)	T Spike (°C)
1	NR242	115	798.5	9.03	5.507	9.786	0.76	0.0953	7.93	9.03	9.55	0.52
2	NR243	131.58	798.9	7.18	5.510	9.786	2.61	0.0860	30.30	7.18	8.52	1.34
3	NR244	125.67	798.5	7.5	5.507	9.786	2.29	0.0946	24.16	7.5	8.7	1.2
4	NR245	162	796.9	4.08	5.496	9.785	5.71	0.0977	58.39	4.08	7.31	3.23
5	NR246	178.67	796.9	2.81	5.496	9.785	6.98	0.0915	76.23	2.81	6.67	3.86
						Average:	**3.67**		**39.40**			
						St. Dev:	**2.58**		**27.49**			

Carbon Dioxide Hydrate, Milli-Q Water, 1 g/l Degussa Uncleaned Al_2O_3 C, Stirring Rate = 450 rpm
All 10 runs

Experiment	Data File (*.dat)	Hydrate Formation Time (min)	Pressure (psi)	Temperature (°C)	Pressure (MPa)	Teq (°C)	SuperCooling (°C)	Cooling Rate (°C/min)	Induction Time (min)	Initial T (°C)	Final T (°C)	T Spike (°C)
1	NR229	148	801.2	5.4	5.526	9.787	4.39	0.0914	48.00	5.4	8.05	2.65
2	NR230	135	801.4	7.01	5.527	9.787	2.78	0.0923	30.09	7.01	8.72	1.71
3	NR231	164	802.6	4.99	5.535	9.788	4.80	0.0928	51.70	4.99	7.67	2.68
4	NR232	184.67	801	2.81	5.524	9.787	6.98	0.0874	79.83	2.81	6.91	4.1
5	NR233	137.33	807.8	7.09	5.571	9.790	2.70	0.0904	29.87	7.09	8.71	1.62
1	NR242	115	798.5	9.03	5.507	9.786	0.76	0.0953	7.93	9.03	9.55	0.52
2	NR243	131.58	798.9	7.18	5.510	9.786	2.61	0.0860	30.30	7.18	8.52	1.34
3	NR244	125.67	798.5	7.5	5.507	9.786	2.29	0.0946	24.16	7.5	8.7	1.2
4	NR245	162	796.9	4.08	5.496	9.785	5.71	0.0977	58.39	4.08	7.31	3.23
5	NR246	178.67	796.9	2.81	5.496	9.785	6.98	0.0915	76.23	2.81	6.67	3.86
						Average:	**4.00**		**43.65**			
						St. Dev:	**2.11**		**23.28**			

Carbon Dioxide Hydrate, Milli-Q Water, 1 g/l Linde D Uncleaned Al_2O_3, Stirring Rate = 450 rpm

Experiment	Data File (*.dat)	Hydrate Formation Time (min)	Pressure (psi)	Temperature (°C)	Pressure (MPa)	Teq (°C)	SuperCooling (°C)	Cooling Rate (°C/min)	Induction Time (min)	Initial T (°C)	Final T (°C)	T Spike (°C)
1	NR247	154.67	802.2	5.01	5.532	9.788	4.78	0.0931	51.32	5.01	7.71	2.7
2	NR248	154.08	802.6	5	5.535	9.788	4.79	0.0950	50.40	5	7.76	2.76
3	NR249	153.25	803.6	5.25	5.542	9.788	4.54	0.0954	47.57	5.25	7.86	2.61
4	NR250	150.67	804	5.33	5.545	9.788	4.46	0.0996	44.76	5.33	7.91	2.58
5	NR251	146.58	804.4	5.86	5.548	9.789	3.93	0.0993	39.57	5.86	8.01	2.15
						Average:	**4.50**		**46.72**			
						St. Dev:	**0.35**		**4.76**			

Carbon Dioxide Hydrate, Milli-Q Water, 1 g/l Linde D Cleaned Al_2O_3, Stirring Rate = 450 rpm

Experiment	Data File (*.dat)	Hydrate Formation Time (min)	Pressure (psi)	Temperature (°C)	Pressure (MPa)	Teq (°C)	SuperCooling (°C)	Cooling Rate (°C/min)	Induction Time (min)	Initial T (°C)	Final T (°C)	T Spike (°C)
1	NR252	145.33	804.2	5.57	5.546	9.789	4.22	0.0998	42.27	5.57	7.95	2.38
2	NR255	171.17	806.2	3.45	5.560	9.790	6.34	0.0966	65.63	3.45	6.98	3.53
3	NR256	160.5	799	4.3	5.510	9.786	5.49	0.0964	56.91	4.3	7.42	3.12
4	NR257	170.42	799.4	3.48	5.513	9.786	6.31	0.0917	68.77	3.48	7.02	3.54
5	NR258	145.42	798	6.04	5.503	9.786	3.75	0.0963	38.90	6.04	8.1	2.06
						Average:	**5.22**		**54.50**			
						St. Dev:	**1.19**		**13.47**			

Carbon Dioxide Hydrate, Milli-Q Water, 0.1 g/l Linde D UnCleaned Al_2O_3, Stirring Rate = 450 rpm

Experiment	Data File (*.dat)	Hydrate Formation Time (min)	Pressure (psi)	Temperature (°C)	Pressure (MPa)	Teq (°C)	SuperCooling (°C)	Cooling Rate (°C/min)	Induction Time (min)	Initial T (°C)	Final T (°C)	T Spike (°C)
1	NR259	155.5	798.8	5	5.509	9.786	4.79	0.0962	49.75	5	7.75	2.75
2	NR260	133	799	6.74	5.510	9.786	3.05	0.1010	30.16	6.74	8.39	1.65
3	NR261	144.58	797.6	5.7	5.501	9.786	4.09	0.0910	44.90	5.7	8.07	2.37
4	NR262	147.67	797.8	5.2	5.502	9.786	4.59	0.0924	49.63	5.2	7.85	2.65
5	NR263	191.17	798	1.61	5.503	9.786	8.18	0.0946	86.43	1.61	5.92	4.31
6	NR271	132.67	799	6.62	5.510	9.786	3.17	0.0976	32.44	6.62	8.33	1.71
						Average:	**3.93**		**41.38**			
						St. Dev:	**0.80**		**9.44**			

Carbon Dioxide Hydrate, Milli-Q Water, 0.01 g/l Linde D UnCleaned Al_2O_3, Stirring Rate = 450 rpm

Experiment	Data File (*.dat)	Hydrate Formation Time (min)	Pressure (psi)	Temperature (°C)	Pressure (MPa)	Teq (°C)	SuperCooling (°C)	Cooling Rate (°C/min)	Induction Time (min)	Initial T (°C)	Final T (°C)	T Spike (°C)
1	NR264	167	797.6	3.55	5.501	9.786	6.24	0.0951	65.57	3.55	6.93	3.38
2	NR265	185.58	796.8	2.12	5.495	9.785	7.67	0.0950	80.68	2.12	6.24	4.12
3	NR266	168.67	797.2	3.56	5.498	9.785	6.23	0.0950	65.53	3.56	6.99	3.43
4	NR267	211.17	798	-0.15	5.503	9.786	9.94	0.0907	109.55	-0.15	5.08	5.23
5	NR268	209	799.2	0	5.512	9.786	9.79	0.0924	105.91	0	4.96	4.96
						Average:	**7.97**		**85.45**			
						St. Dev:	**1.82**		**21.30**			

Carbon Dioxide Hydrate, Milli-Q Water, 0.01 g/l Linde D UnCleaned Al_2O_3, Made up new solution, Stirring Rate = 450 rpm

Experiment	Data File (*.dat)	Hydrate Formation Time (min)	Pressure (psi)	Temperature (°C)	Pressure (MPa)	Teq (°C)	SuperCooling (°C)	Cooling Rate (°C/min)	Induction Time (min)	Initial T (°C)	Final T (°C)	T Spike (°C)
1	NR269	163.33	799.4	3.79	5.513	9.786	6.00	0.0986	60.81	3.79	7.13	3.34
2	NR270	171.42	798.6	3.26	5.508	9.786	6.53	0.0975	66.93	3.26	6.8	3.54
						Average:	**6.53**		**67.91**			
						St. Dev:	**0.66**		**7.51**			

Carbon Dioxide Hydrate, Milli-Q Water, 0.05 g/l Linde D UnCleaned Al_2O_3, Stirring Rate = 450 rpm

Experiment	Data File (*.dat)	Hydrate Formation Time (min)	Pressure (psi)	Temperature (°C)	Pressure (MPa)	Teq (°C)	SuperCooling (°C)	Cooling Rate (°C/min)	Induction Time (min)	Initial T (°C)	Final T (°C)	T Spike (°C)
1	NR272	160.33	799.2	4.1	5.512	9.786	5.69	0.0923	61.60	4.1	7.36	3.26
2	NR273	179.42	804	3.77	5.545	9.788	6.02	0.0856	70.30	3.77	7.25	3.48
3	NR274	171	801	4.74	5.524	9.787	5.05	0.0864	58.41	4.74	7.81	3.07
4	NR275	164.67	800.6	5.19	5.521	9.787	4.60	0.0891	51.59	5.19	8.12	2.93
5	NR276	187.67	801	3.56	5.524	9.787	6.23	0.0889	70.04	3.56	7.48	3.92
						Average:	**5.52**		**62.39**			
						St. Dev:	**0.68**		**7.97**			

Carbon Dioxide Hydrate, Milli-Q Water, 0.005 g/l Linde D UnCleaned Al_2O_3, Stirring Rate = 450 rpm

Experiment	Data File (*.dat)	Hydrate Formation Time (min)	Pressure (psi)	Temperature (°C)	Pressure (MPa)	Teq (°C)	SuperCooling (°C)	Cooling Rate (°C/min)	Induction Time (min)	Initial T (°C)	Final T (°C)	T Spike (°C)
1	NR277	187.67	801	3.56	5.524	9.787	6.23	0.0882	70.60	3.56	7.48	3.92
2	NR278	211	801.6	1.56	5.528	9.787	8.23	0.0843	97.59	1.56	6.44	4.88
3	NR279	139	803.6	6.14	5.542	9.788	3.65	0.0912	40.00	6.14	8.34	2.2
4	NR280	148.67	803.6	5.22	5.542	9.788	4.57	0.0921	49.60	5.22	7.93	2.71
						Average:	**5.67**		**64.45**			
						St. Dev:	**2.01**		**25.53**			

Carbon Dioxide Hydrate, Milli-Q Water, 10 m^2/l Iron Oxide, Stirring Rate = 450 rpm

Experiment	Data File (*.dat)	Hydrate Formation Time (min)	Pressure (psi)	Temperature (°C)	Pressure (MPa)	Teq (°C)	SuperCooling (°C)	Cooling Rate (°C/min)	Induction Time (min)	Initial T (°C)	Final T (°C)	T Spike (°C)
1	NR281[1]	198.33	801.2	1.13	5.526	9.787	8.66	0.0857	101.02	1.13	5.79	4.66
2	NR282	181.08	799.3	2.56	5.512	9.786	7.23	0.0854	84.61	2.56	6.64	4.08
3	NR283	239.17	800	-2.2	5.517	9.787	11.99	0.0833	143.90	-2.2	4.23	6.43
4	NR284	250.5	801	-2.97	5.524	9.787	12.76	0.0833	153.15	-2.97	No Hydrate	
5	NR285	290	800	-6.04	5.517	9.787	15.83	0.0823	192.31	-6.04	1.83	7.87
						Average:	**11.29**		**135.00**			
						St. Dev:	**3.42**		**42.97**			

Carbon Dioxide Hydrate, Milli-Q Water, 1 m^2/l Iron Oxide, Stirring Rate = 450 rpm

Experiment	Data File (*.dat)	Hydrate Formation Time (min)	Pressure (psi)	Temperature (°C)	Pressure (MPa)	Teq (°C)	SuperCooling (°C)	Cooling Rate (°C/min)	Induction Time (min)	Initial T (°C)	Final T (°C)	T Spike (°C)
1	Nr286	302.08	799.3	-6.93	5.512	9.786	16.72	0.0818	204.35	No hydrate ever formed		

Carbon Dioxide Hydrate, Milli-Q Water, 10 m^2/l Uncleaned Degussa Al_2O_3, Stirring Rate = 450 rpm

Experiment	Data File (*.dat)	Hydrate Formation Time (min)	Pressure (psi)	Temperature (°C)	Pressure (MPa)	Teq (°C)	SuperCooling (°C)	Cooling Rate (°C/min)	Induction Time (min)	Initial T (°C)	Final T (°C)	T Spike (°C)
1	NR287	179	802.6	2.6	5.535	9.788	7.19	0.0889	80.85	2.6	6.67	4.07
2	NR288	133	802.8	6.92	5.537	9.788	2.87	0.0923	31.07	6.92	8.47	1.55
3	NR289	284.25	804	-5.43	5.545	9.788	15.22	0.0842	180.74	-5.43	2.18	7.61
						Average:	**8.42**		**97.55**			
						St. Dev:	**6.27**		**76.22**			

Carbon Dioxide Hydrate, Milli-Q Water, 10 m^2/l Uncleaned Linde D Al_2O_3, Stirring Rate = 450 rpm

Experiment	Data File (*.dat)	Hydrate Formation Time (min)	Pressure (psi)	Temperature (°C)	Pressure (MPa)	Teq (°C)	SuperCooling (°C)	Cooling Rate (°C/min)	Induction Time (min)	Initial T (°C)	Final T (°C)	T Spike (°C)
1	NR290	151.08	802.8	5.06	5.537	9.788	4.73	0.0898	52.65	5.06	7.9	2.84
2	NR291	156.67	807.2	4.61	5.567	9.790	5.18	0.0863	60.02	4.61	7.74	3.13
3	NR292	155.67	803	4.67	5.538	9.788	5.12	0.0870	58.83	4.67	7.74	3.07
4	NR309	166.17	802.2	3.97	5.532	9.788	5.82	0.0873	66.64	3.97	7.36	3.39
5	NR310	197.42	808.6	1.74	5.577	9.791	8.05	0.0860	93.62	1.74	6.22	4.48
6	NR311	146.67	802.6	5.66	5.535	9.788	4.13	0.0860	48.00	5.66	8.03	2.37
7	NR312	166.67	799.7	4.04	5.515	9.787	5.75	0.0894	64.28	4.04	7.39	3.35
8	NR313	146.25	798.7	5.64	5.508	9.787	4.15	0.0878	47.23	5.64	8.1	2.46
9	NR314	142.08	798.5	6.04	5.507	9.787	3.75	0.0874	42.87	6.04	8.23	2.19
10	NR315	181.17	797.5	2.72	5.500	9.787	7.07	0.0853	82.85	2.72	6.76	4.04
						Average:	**5.37**		**61.70**			
						St. Dev:	**1.36**		**16.13**			

Carbon Dioxide Hydrate, Milli-Q Water, 10 m^2/l Uncleaned Degussa Al_2O_3, Stirring Rate = 450 rpm, Second Try after Cleaning Every

Experiment	Data File (*.dat)	Hydrate Formation Time (min)	Pressure (psi)	Temperature (°C)	Pressure (MPa)	Teq (°C)	SuperCooling (°C)	Cooling Rate (°C/min)	Induction Time (min)	Initial T (°C)	Final T (°C)	T Spike (°C)
1	NR293	188	802.4	1.92	5.534	9.788	7.87	0.0860	91.49	1.92	6.44	4.52
2	NR294	169.67	803.2	3.48	5.539	9.788	6.31	0.0856	73.69	3.48	7.2	3.72
3	NR295	165.25	807.6	3.86	5.570	9.790	5.93	0.0893	66.41	3.86	7.37	3.51
4	NR296	201.67	800.4	0.89	5.520	9.787	8.90	0.0853	104.30	0.89	5.85	4.96
5	NR297	221	800.8	-0.47	5.523	9.787	10.26	0.0856	119.82	-0.47	4.99	5.46
						Average:	**7.85**		**91.14**			
						St. Dev:	**1.80**		**21.87**			

Carbon Dioxide Hydrate, Milli-Q Water, 10 m^2/l Uncleaned Linde C Al_2O_3, Stirring Rate = 450 rpm

Experiment	Data File (*.dat)	Hydrate Formation Time (min)	Pressure (psi)	Temperature (°C)	Pressure (MPa)	Teq (°C)	SuperCooling (°C)	Cooling Rate (°C/min)	Induction Time (min)	Initial T (°C)	Final T (°C)	T Spike (°C)
1	NR298	229.67	799.1	-1.22	5.511	9.786	11.01	0.0848	129.79	-1.22	4.76	5.98
2	NR299	205.67	797.3	0.5	5.499	9.785	9.29	0.0849	109.36	0.5	5.56	5.06
3	NR300	221.17	798.1	-0.6	5.504	9.786	10.39	0.0836	124.23	-0.6	5.11	5.71
4	NR301	211.17	795.9	0.09	5.489	9.785	9.70	0.0844	114.87	0.09	5.35	5.26
5	NR302	236.17	798.5	-1.93	5.507	9.786	11.72	0.0852	137.51	-1.93	4.19	6.12
						Average:	**10.42**		**123.15**			
						St. Dev:	**0.98**		**11.29**			

Carbon Dioxide Hydrate, Milli-Q Water, 10 m^2/l Uncleaned Linde A Al_2O_3, Stirring Rate = 450 rpm

Experiment	Data File (*.dat)	Hydrate Formation Time (min)	Pressure (psi)	Temperature (°C)	Pressure (MPa)	Teq (°C)	SuperCooling (°C)	Cooling Rate (°C/min)	Induction Time (min)	Initial T (°C)	Final T (°C)	T Spike (°C)
1	NR303	204.42	797.3	-1.93	5.499	9.785	11.72	0.0835	140.30	-1.93	4.33	6.26
2	NR304	204.67	797.1	0.47	5.497	9.785	9.32	0.0838	111.16	0.47	5.66	5.19
3	NR305	199	797.5	0.99	5.500	9.785	8.80	0.0864	101.79	0.99	5.71	4.72
4	NR306	179.67	799.3	2.6	5.512	9.786	7.19	0.0868	82.79	2.6	6.56	3.96
5	NR307	209.25	800.6	0.32	5.521	9.787	9.47	0.0848	111.64	0.32	5.52	5.2
6	NR308	149.67	801.2	4.81	5.526	9.787	4.98	0.0886	56.17	4.81	7.7	2.89
						Average:	**8.58**		**100.64**			
						St. Dev:	**2.29**		**28.64**			

Carbon Dioxide Hydrate, Milli-Q Water, 100 m^2/l Silica, Stirring Rate = 450 rpm

Experiment	Data File (*.dat)	Hydrate Formation Time (min)	Pressure (psi)	Temperature (°C)	Pressure (MPa)	Teq (°C)	SuperCooling (°C)	Cooling Rate (°C/min)	Induction Time (min)	Initial T (°C)	Final T (°C)	T Spike (°C)
1	nr316	0.08	801.6	-4.27	5.528	9.785	14.06	0.0835	168.32	-4.27	2.87	7.14
2	nr317	177	796.9	2.64	5.496	9.785	7.15	0.0875	81.66	2.64	6.61	3.97
3	nr318	138.67	796.1	5.73	5.490	9.785	4.06	0.0953	42.55	5.73	8.11	2.38
4	nr319	238.17	796.1	-2.76	5.490	9.785	12.55	0.0856	146.55	-2.76	4.05	6.81
5	nr320	231.67	796.1	-2.44	5.490	9.785	12.23	0.0839	145.71	-2.44	3.84	6.28
						Average:	**10.01**		**116.96**			
						St. Dev:	**4.22**		**52.73**			

Carbon Dioxide Hydrate, Milli-Q Water, 1 g/l Uncleaned, Unsonicated Degussa Al_2O_3, Stirring Rate = 450 rpm

Experiment	Data File (*.dat)	Hydrate Formation Time (min)	Pressure (psi)	Temperature (°C)	Pressure (MPa)	Teq (°C)	SuperCooling (°C)	Cooling Rate (°C/min)	Induction Time (min)	Initial T (°C)	Final T (°C)	T Spike (°C)
1	nr321	147.42	797.9	4.71	5.503	9.786	5.08	0.0914	55.54	4.71	7.63	2.92
2	nr322	195	805	0.79	5.552	9.789	9.00	0.0864	104.16	0.79	5.72	4.93
						Average:	**7.04**		**79.85**			
						St. Dev:	**2.77**		**34.38**			

Carbon Dioxide Hydrate, Milli-Q Water, 1 g/L Uncleaned Linde C Al_2O_3, Stirring Rate = 450 rpm

Experiment	Data File (*.dat)	Hydrate Formation Time (min)	Pressure (psi)	Temperature (°C)	Pressure (MPa)	Teq (°C)	SuperCooling (°C)	Cooling Rate (°C/min)	Induction Time (min)	Initial T (°C)	Final T (°C)	T Spike (°C)
1	nr323	263.25	804.4	-4.75	5.548	9.788	14.54	0.0839	173.28	-4.75	2.65	7.4
						Average:	**14.54**		**173.28**			

Carbon Dioxide Hydrate, Milli-Q Water, 1 g/L $Mg(OH)_2$, Stirring Rate = 450 rpm

Experiment	Hydrate Formation Data File (*.dat)	Time (min)	Pressure (psi)	Temperature (°C)	Pressure (MPa)	Teq (°C)	SuperCooling (°C)	Cooling Rate (°C/min)	Induction Time (min)	Initial T (°C)	Final T (°C)	T Spike (°C)
1	nr324	178.58	796.9	2.11	5.496	9.786	7.68	0.0896	85.67	2.11	6.3	4.19
2	nr325	239.17	816.4	-2.99	5.630	9.786	12.78	0.0852	149.95	-2.99	3.35	6.34
3	nr326	206.67	806.8	-0.28	5.564	9.786	10.07	0.0860	117.05	-0.28	4.98	5.26
4	nr327	217.5	794.5	-1.02	5.479	9.786	10.81	0.0860	125.65	-1.02	4.51	5.53
5	nr328	244.58	795.7	-3.54	5.488	9.786	13.33	0.0855	155.86	-3.54	3.35	6.89
						Average:	**10.93**		**126.84**			
						St. Dev:	**2.26**		**28.15**			

Carbon Dioxide Hydrate, Milli-Q Water, 1 g/L $CaCO_3$, Stirring Rate = 450 rpm

Experiment	Hydrate Formation Data File (*.dat)	Time (min)	Pressure (psi)	Temperature (°C)	Pressure (MPa)	Teq (°C)	SuperCooling (°C)	Cooling Rate (°C/min)	Induction Time (min)	Initial T (°C)	Final T (°C)	T Spike (°C)
1	nr329	269	796.7	-5.11	5.494	9.786	14.90	0.0838	177.76	-5.11	2.43	7.54
2	nr330	238.58	800.2	-2.97	5.519	9.786	12.76	0.0844	151.14	-2.97	3.62	6.59
3	nr331	157	798.1	3.94	5.504	9.786	5.85	0.0915	63.89	3.94	7.34	3.4
						Average:	**11.17**		**130.93**			
						St. Dev:	**4.73**		**59.56**			

Carbon Dioxide Hydrate, Milli-Q Water, 1 g/L Linde D, Stirring Rate = 450 rpm, All Results together:

Experiment	Data File (*.dat)	Hydrate Formation Time (min)	Pressure (psi)	Temperature (°C)	Pressure (MPa)	Teq (°C)	SuperCooling (°C)	Cooling Rate (°C/min)	Induction Time (min)	Initial T (°C)	Final T (°C)	T Spike (°C)
1	nr332	157.58	796.5	3.82	5.493	9.786	5.97	0.0894	66.73	3.82	7.29	3.47
2	nr333	151.25	795.5	4.36	5.486	9.786	5.43	0.0888	61.10	4.36	7.59	3.23
3	nr334	148.58	801.2	4.6	5.526	9.786	5.19	0.0899	57.69	4.6	7.62	3.02
4	nr335	151	800.6	4.43	5.521	9.786	5.36	0.0894	59.91	4.43	7.63	3.2
5	nr336	147	801.2	4.67	5.526	9.786	5.12	0.0897	57.03	4.67	7.73	3.06
1	NR247	154.67	802.2	5.01	5.532	9.788	4.78	0.0931	51.32	5.01	7.71	2.7
2	NR248	154.08	802.6	5	5.535	9.788	4.79	0.0950	50.40	5	7.76	2.76
3	NR249	153.25	803.6	5.25	5.542	9.788	4.54	0.0954	47.57	5.25	7.86	2.61
4	NR250	150.67	804	5.33	5.545	9.788	4.46	0.0996	44.76	5.33	7.91	2.58
5	NR251	146.58	804.4	5.86	5.548	9.789	3.93	0.0993	39.57	5.86	8.01	2.15
						Average:	**4.95**		**53.61**			
						St. Dev:	**0.58**		**8.33**			

Carbon Dioxide Hydrate, Milli-Q Water, 1 g/L Linde D, Stirring Rate = 450 rpm

Experiment	Data File (*.dat)	Hydrate Formation Time (min)	Pressure (psi)	Temperature (°C)	Pressure (MPa)	Teq (°C)	SuperCooling (°C)	Cooling Rate (°C/min)	Induction Time (min)	Initial T (°C)	Final T (°C)	T Spike (°C)
1	nr332	157.58	796.5	3.82	5.493	9.786	5.97	0.0894	66.73	3.82	7.29	3.47
2	nr333	151.25	795.5	4.36	5.486	9.786	5.43	0.0888	61.10	4.36	7.59	3.23
3	nr334	148.58	801.2	4.6	5.526	9.786	5.19	0.0899	57.69	4.6	7.62	3.02
4	nr335	151	800.6	4.43	5.521	9.786	5.36	0.0894	59.91	4.43	7.63	3.2
5	nr336	147	801.2	4.67	5.526	9.786	5.12	0.0897	57.03	4.67	7.73	3.06
						Average:	**5.41**		**60.49**			
						St. Dev:	**0.34**		**3.86**			

Carbon Dioxide Hydrate, Synthetic Sea Water, No Seed, Stirring Rate = 450 rpm

Experiment	Data File (*.dat)	Hydrate Formation Time (min)	Pressure (psi)	Temperature (°C)	Pressure (MPa)	Teq (°C)	SuperCooling (°C)	Cooling Rate (°C/min)	Induction Time (min)	Initial T (°C)	Final T (°C)	T Spike (°C)
1	nr350	274.67	799.5	-5.73	5.514	8.680	14.41	0.0869	165.83	-5.73	0.63	6.36
2	nr351	236.67	799.3	-2.75	5.512	8.680	11.43	0.0921	124.11	-2.75	2.58	5.33
3	nr352	276.42	806.2	-5.76	5.560	8.686	14.45	0.0890	162.32	-5.76	0.79	6.55
4	nr353	293.08	808.4	-7.01	5.575	8.688	15.70	0.0875	179.41	-7.01	-0.53	6.48
5	nr354	253.5	798.5	-3.59	5.507	8.679	12.27	0.0876	140.06	-3.59	1.83	5.42
						Average:	**13.65**		**154.34**			
						St. Dev:	**1.75**		**22.03**			

Carbon Dioxide Hydrate, Synthetic Sea Water, 1 g/L Linde D AL_2O_3, unwashed, older batch from Linde, Stirring Rate = 450 rpm

Experiment	Data File (*.dat)	Hydrate Formation Time (min)	Pressure (psi)	Temperature (°C)	Pressure (MPa)	Teq (°C)	SuperCooling (°C)	Cooling Rate (°C/min)	Induction Time (min)	Initial T (°C)	Final T (°C)	T Spike (°C)
1	nr355	195.17	796.5	1.18	5.493	8.678	7.50	0.0895	83.77	1.18	4.83	3.65
2	nr356	189.5	797.7	2.11	5.501	8.679	6.57	0.0869	75.59	2.11	5.26	3.15
3	nr357	184	799.3	2.32	5.512	8.680	6.36	0.0845	75.27	2.32	5.48	3.16
4	nr358	205.08	798.1	0.58	5.504	8.679	8.10	0.0879	92.14	0.58	4.59	4.01
5	nr359	195.67	800.8	1.44	5.523	8.682	7.24	0.0891	81.27	1.44	5.01	3.57
						Average:	**7.15**		**81.61**			
						St. Dev:	**0.71**		**6.93**			

Carbon Dioxide Hydrate, Milliq water, 10 g/L Linde D AL_2O_3, unwashed, older batch from Linde, Stirring Rate = 450 rpm

Experiment	Data File (*.dat)	Hydrate Formation Time (min)	Pressure (psi)	Temperature (°C)	Pressure (MPa)	Teq (°C)	SuperCooling (°C)	Cooling Rate (°C/min)	Induction Time (min)	Initial T (°C)	Final T (°C)	T Spike (°C)
1	nr360	134.67	802.6	6.34	5.535	9.786	3.45	0.0924	37.29	6.34	8.34	2
2	nr361	129.08	803.8	7.02	5.543	9.786	2.77	0.0906	30.53	7.02	8.6	1.58
3	nr362	158.67	802	4.41	5.531	9.786	5.38	0.0896	60.00	4.41	7.53	3.12
4	nr363	145.67	801.6	5.43	5.528	9.786	4.36	0.0878	49.61	5.43	8.07	2.64
5	nr364	218.17	801.4	-0.67	5.527	9.786	10.46	0.0852	122.72	-0.67	3.31	3.98
6	nr365	140.08	801.2	6.1	5.526	9.786	3.69	0.0878	41.98	6.1	8.24	2.14
7	nr366	154.25	800.2	4.82	5.519	9.786	4.97	0.0899	55.24	4.82	7.82	3
						Average:	**4.10**		**45.78**			
						St. Dev:	**0.98**		**11.18**			

Carbon Dioxide Hydrate, Milliq water, 1 g/L B AL_2O_3, unwashed, new batch from Praxair, Stirring Rate = 450 rpm

Experiment	Data File (*.dat)	Hydrate Formation Time (min)	Pressure (psi)	Temperature (°C)	Pressure (MPa)	Teq (°C)	SuperCooling (°C)	Cooling Rate (°C/min)	Induction Time (min)	Initial T (°C)	Final T (°C)	T Spike (°C)
1	nr367	179.25	798.5	3.1	5.507	9.786	6.69	0.0874	76.50	3.1	6.82	3.72
2	nr368	223.17	798.5	-0.97	5.507	9.786	10.76	0.0877	122.65	-0.97	4.68	5.65
3	nr369	294.67	797.9	-6.52	5.503	9.786	16.31	0.0913	178.60	-6.52	1.62	8.14
4	nr370	188.5	798.7	1.98	5.508	9.786	7.81	0.0880	88.70	1.98	6.38	4.4
5	nr371	225.5	798.5	-1.04	5.507	9.786	10.83	0.0882	122.74	-1.04	4.78	5.82
6	nr372	304.17	802.4	-7.01	5.534	9.786	16.80	0.0860	195.30	-7.01	1.1	8.11
						Average:	**11.53**		**130.75**			
						St. Dev:	**4.22**		**47.53**			

Carbon Dioxide Hydrate, Milliq water, unwashed, Particles Filtered Out, Stirring Rate = 450 rpm

Experiment	Data File (*.dat)	Hydrate Formation Time (min)	Pressure (psi)	Temperature (C)	Pressure (MPa)	Teq (C)	SuperCooling (C)	Cooling Rate (°C/min)	Induction Time (min)	Initial T (C)	Final T (C)	T Spike (C)
1	nr377	234	799.3	-1.93	5.512	9.786	11.72	0.0901	130.03	-1.93	4.2	6.13
2	nr378	234.08	799.3	-1.93	5.512	9.786	11.72	0.0912	128.46	-1.93	4.2	6.13
3	nr379	181.67	796.5	2.68	5.493	9.785	7.11	0.0912	77.91	2.68	6.6	3.92
						Average:	**10.18**		**112.13**			
						St. Dev:	**2.66**		**29.65**			

Carbon Dioxide Hydrate, Milli-q Water, 10 g/L Linde A AL_2O_3, unwashed Stirring Rate = 450 rpm

Experiment	Data File (*.dat)	Hydrate Formation Time (min)	Pressure (psi)	Temperature (C)	Pressure (MPa)	Teq (C)	SuperCooling (C)	Cooling Rate (°C/min)	Induction Time (min)	Initial T (C)	Final T (C)	T Spike (C)
1	nr380	222.67	802.8	-1.1	5.537	9.788	10.89	0.0895	121.65	-1.1	4.57	5.67
2	nr381	185.08	802	1.76	5.531	9.787	8.03	0.0869	92.37	1.76	6.34	4.58
3	nr382	143.25	800.6	5.34	5.521	9.787	4.45	0.0845	52.63	5.34	8.08	2.74
4	nr383	191.08	801	1.29	5.524	9.787	8.50	0.0879	96.67	1.29	6.1	4.81
5	nr384	198.42	801.6	0.68	5.528	9.787	9.11	0.0891	102.21	0.68	5.78	5.1
						Average:	**8.19**		**93.11**			
						St. Dev:	**2.36**		**25.25**			

Carbon Dioxide Hydrate, Milli-q Water, 1 g/L Linde CuO, unwashed Stirring Rate = 450 rpm

Experiment	Data File (*.dat)	Hydrate Formation Time (min)	Pressure (psi)	Temperature (°C)	Pressure (MPa)	Teq (°C)	SuperCooling (°C)	Cooling Rate (°C/min)	Induction Time (min)	Initial T (°C)	Final T (°C)	T Spike (°C)
1	nr385	115.67	802.2	8.12	5.532	9.788	1.67	0.0895	18.64	8.12	9.1	0.98
2	nr386	115.58	801.2	8.31	5.526	9.787	1.48	0.0869	17.00	8.31	9.16	0.85
3	nr387	113	801	8.81	5.524	9.787	0.98	0.0845	11.56	8.81	9.36	0.55
4	nr388	113.58	801.2	8.64	5.526	9.787	1.15	0.0845	13.57	8.64	9.29	0.65
5	nr389	113.58	799.3	8.42	5.512	9.786	1.37	0.0845	16.17	8.42	9.22	0.8
						Average:	**1.33**		**15.39**			
						St. Dev:	**0.27**		**2.81**			